2020

Chemical Biology of Dynein

Cristina C. Santarossa

CHEMICAL BIOLOGY OF DYNEIN

A Thesis Presented to the Faculty of

The Rockefeller University

in Partial Fulfillment of the Requirements for

the degree of Doctor of Philosophy

by

Cristina C. Santarossa

June 2020

CHEMICAL BIOLOGY OF DYNEIN

Cristina C. Santarossa, Ph.D.
The Rockefeller University 2020

Cytoplasmic dynein is a AAA (ATPase Associated with various Activities) motor protein that transports cellular cargoes towards the microtubule minus-end. Despite its essential role in intracellular transport, dynein remains the least understood cytoskeletal motor. With speeds >25 μm/min in cells, dynein's cellular functions are challenging to study using genetic approaches, such as CRISPR and RNA interference, as the perturbation timescales far exceed those of dynein action. Fast-acting small molecule probes can be powerful tools to study dynein's many cellular mechanisms, but the design of potent and selective inhibitors of dynein remains challenging.

Inhibitors of dynein's motor domain have been reported, such as ciliobrevins, dynapyrazoles and dynarrestin, but the inhibitor-binding site(s) have yet to be elucidated. Though inhibitor-bound dynein structures have been long-sought after, efforts have been curtailed by difficulties in obtaining high-resolution dynein structures and the lack of an inhibitor with the requisite chemical properties, such as compound solubility and stability, for structural studies. The work presented here describes the design and characterization of a class of dynein probes, one of which we use to obtain an inhibitor-bound structure of dynein.

The first chapter "Chemical inhibitors of AAA proteins" provides a brief overview of AAA proteins in general and the inhibitors that have been designed. The chapter emphasizes on the design and characterization of ciliobrevins, dynapyrazoles and dynarrestin, three classes of dynein

inhibitors with distinct mechanisms of action. Their limitations as cellular probes are discussed and motivates the need for compounds with improved potency and selectivity.

In the second chapter, "Dynapyrazoles acutely inhibit intraflagellar transport", I characterize dynapyrazole-A in a cell-based assay that can measure the effect of the compound on intraflagellar transport (IFT). Dynapyrazole-A is an acute reversible inhibitor of dynein 2-dependent retrograde transport and can be a useful probe to study IFT function. However, as dynapyrazole-A inhibits both isoforms of dynein, its use as a chemical probe is limited due to its cytotoxic effects at treatment times >1 hour. This chapter motivates the need for dynein-2 specific inhibitors.

Finally, I present a third chapter, "Structural insights into the chemical inhibition of dynein", that discusses the design of a dynapyrazole derivative, compound **20**, that inhibits the basal ATPase activity of human and *S. cerevisiae* dynein. I used cryo-EM to obtain a structure of *S. cerevisae* dynein's motor domain in the presence of the dynapyrazole derivative and find that the compound binds to the regulatory ATPase sites in the AAA3 and AAA4 domains, rather than the main catalytic site in the AAA1 domain. This finding addresses a major gap in our knowledge, as inhibitors of dynein's ATPase activity have been assumed to target the AAA1 domain. Inhibitor design efforts can now be focused on the regulatory ATPase sites to obtain potent and selective small molecule probes of dynein.

ACKNOWLEDGEMENTS

I would like to first like to thank Tarun for your mentorship and for teaching me the skills that are necessary to succeed in the research field. To my collaborators Gira Bhabha and Damian Ekiert, thank you for helping make my main project possible. Your enduring optimism was greatly appreciated. To my committee members (Sean Brady, Howard Hang, and Scott Blanchard), thank you for your scientific input and encouragement. To Richard Hite, thank you for agreeing to be my external examiner. To my colleagues, thank you for your helpful scientific discussions and for creating a lab environment that is enjoyable to be in every day. To my friends Tommaso and Carolina, thank you for being like family and for the many fun times. To my mom and grandparents, thank you for supporting all of my endeavors. And lastly, to my best friend and constant companion, Priyanka Verma, thank you for your day-to-day support and encouragement.

TABLE OF CONTENTS

LIST OF FIGURES

LIST OF APPENDICES

LIST OF TABLES

Chapter 1: Chemical inhibitors of AAA proteins

1.1 Introduction

The AAA (ATPases Associated with various cellular Activities) ATPase superfamily consists of functionally diverse proteins that share a structurally conserved ATP-binding domain. Humans contain ~100 AAA proteins that are essential for a wide range of cellular functions, including cell division, intracellular transport, and organelle biogenesis (Erzberger and Berger, 2006; Steinman et al., 2017). To perform these functions, members of this superfamily assemble into oligomeric structures and convert the energy from ATP hydrolysis into mechanical force.

The ATP-binding domain (~250 amino acids, hereafter, AAA domain) share features with the classic phosphate-binding loop (P-loop) NTPases and consists of a AAA-large (AAA-L) and a AAA-small (AAA-S) subdomain (Erzberger and Berger, 2006). Like the P-loop NTPases, the AAA domain contains an αβα core, where the N-terminal β-strand and the following α-helix are connected by a flexible loop. This loop contains the Walker A motif (consensus sequence GxxxxGK[S/T], where x is any residue) that is necessary for ATP binding (Figure 1.1). However, AAA proteins distinguish themselves from P-loop NTPases by the presence of a catalytic glutamate in the Walker B motif (consensus sequence hhhhDE, where h denotes hydrophobic residue) which is essential for ATP hydrolysis (Figure 1.1) (Shalaeva et al., 2018; Walker et al., 1982). The active site also contains sensor 2 and arginine finger residues, which are not conserved across members of the AAA superfamily, possibly resulting in functional diversification (Figure 1.1) (Erzberger and Berger, 2006). Despite containing a structurally conserved AAA domain, AAA proteins can be tuned for specific cellular functions by assembling their domains into a diverse array of oligomeric structures.

AAA proteins function as oligomers that have been observed to adopt ring-like structures, where the hexameric arrangement is most common. Once the oligomeric ensemble forms, ATP binding occurs at the tripartite interface between the AAA-L, AAA-S and the neighboring adjacent AAA large subdomains (Figure 1.1) (Vale, 2000). Most AAA proteins, such as katanin and spastin, contain a single AAA domain that exists in equilibrium between monomers and monohexamers (Vale, 2000). However, a subset of AAA proteins, such as dynein and midasin, contain a hexameric ring with six distinct AAA modules that are contained within a single polypeptide (Vale, 2000). For these proteins, the six AAA domains are interdependent, and have intricate allosteric communications that regulate their overall activity.

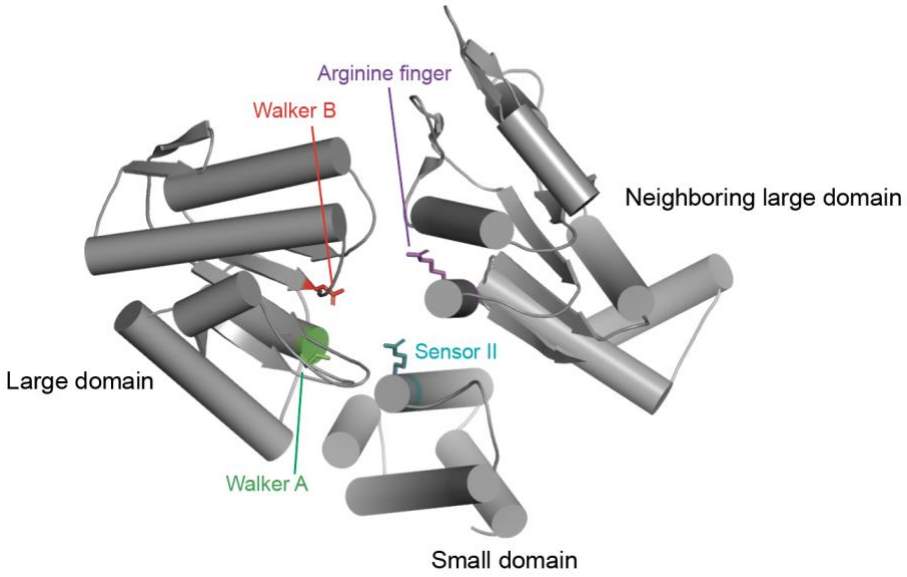

Figure 1.1 Schematic of the AAA module showing the large, small, and neighboring subdomains. Walker A (green), walker B (red), sensor II (cyan), and arginine finger (purple) motifs are indicated.

1.2 Targeting AAA proteins using small molecule inhibitors

AAA proteins can be challenging to study as they carry out cellular functions within the timescale of seconds to minutes. Small molecule inhibitors can be powerful tools to dissect their dynamic mechanisms, as the timescale of perturbation can match that of protein function. Additionally, the inhibition of certain AAA proteins, such as VCP/p97 and dynein 2, can be a therapeutic approach for targeting tumor cells (Höing et al., 2018; Tang et al., 2019). However, the design of small molecule inhibitors of AAA proteins can be challenging for at least three reasons. First, the active site of AAA proteins is conserved across the AAA superfamily. Second, structural data for many of the AAA proteins are lacking, which can be crucial for inhibitor design. Third, certain members of the AAA superfamily have multiple distinct ATPase sites with differing roles in the protein's mechanochemical cycle. Despite these challenges, at least seventeen cell-permeable probes of AAA proteins have been developed and can be classified as either ATP competitive or allosteric inhibitors (Steinman and Kapoor, 2019).

Several inhibitors of the valosin-containing protein, VCP/p97, have been identified and act in either a competitive or allosteric manner (Steinman and Kapoor, 2019). VCP/p97 is needed for the degradation of unfolded and ubiquitylated proteins and inhibition of this protein has been proposed as a therapeutic approach for targeting protein homeostasis in tumor cells. This protein contains two AAA domains per polypeptide protomer (designated D1 and D2), resulting in a double-stacked ring upon oligomerization (van den Boom and Meyer, 2018; White and Lauring, 2007). DBeQ is an inhibitor of p97 and acts in a ATP competitive manner with a half-maximal inhibitory concentration (IC_{50}) of 1.5 μM (Figure 1.2) (Chou et al., 2011). A derivative of DBeQ, CB-5083, was shown to bind to the D2 domain in p97, but failed in Phase 1 clinical trials due to

an unexpected off-target affect (Figure 1.2) (Tang et al., 2019). This outcome highlights the difficulties in designing active site inhibitors that are selective to only one ATPase.

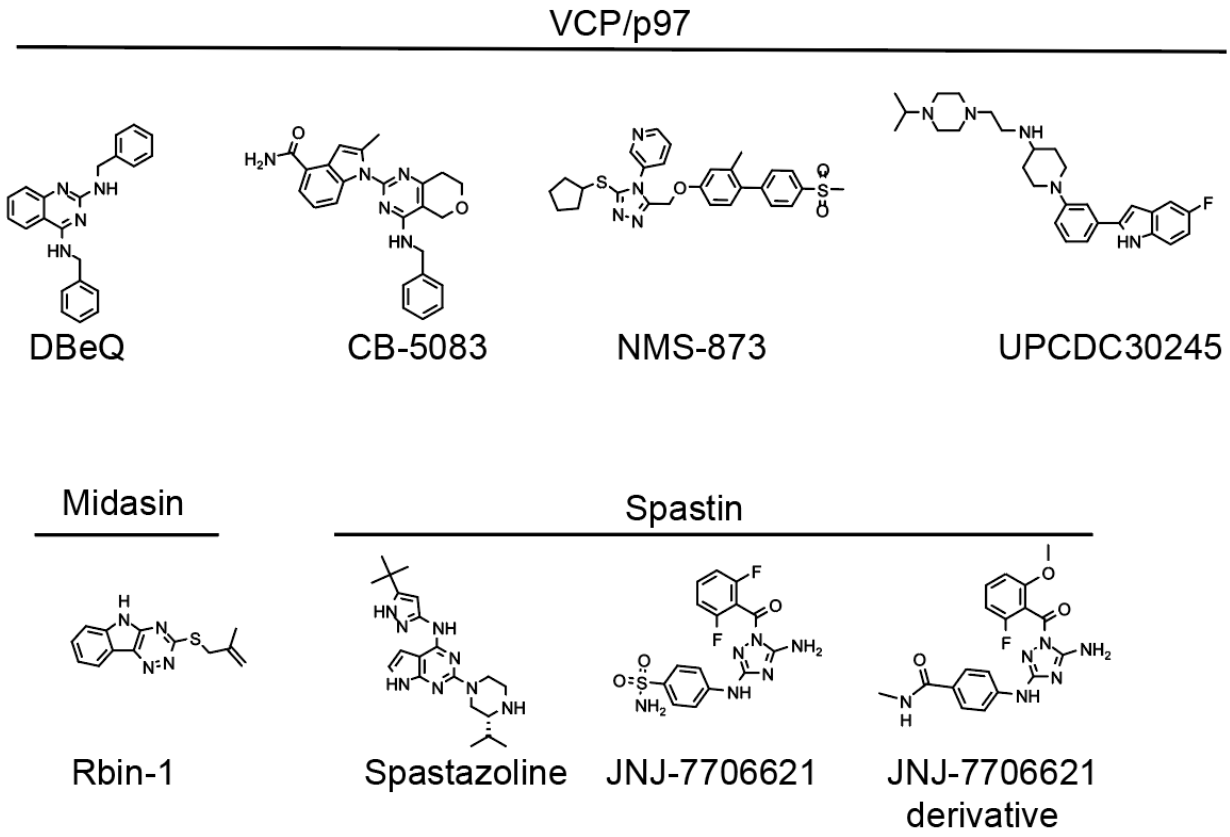

Figure 1.2 Small molecules inhibitors of VCP/p97, midasin, and spastin, which are discussed in this chapter.

The other class of p97 inhibitors behave in an allosteric manner. UPCDC30245 is a phenyl indole derivative of DBeQ that inhibits p97's ATPase activity with an IC_{50} of ~27 nM (Figure 1.2) (Banerjee et al., 2016). A high-resolution (2.3 Å) cryo-EM structure of p97 in the presence of UPCDC30245 revealed that this compound binds at the junction between the D1 and D2 domains (Banerjee et al., 2016). NMS-873 was identified in a high-throughput screen and also inhibits p97's ATPase activity in a non-competitive manner (IC_{50}: ~300 μM) (Figure 1.2). To determine the binding site of NMS-873, azido derivatives of the compound were synthesized and UV-crosslinked to p97 (Magnaghi et al., 2013). Proteolysis and subsequent ESI-MS/MS analysis revealed that the

photo-affinity probe formed a stable adduct with residue Asn616, which is located in a tunnel formed by two D1 and one D2 domains (Magnaghi et al., 2013).

ATP-competitive inhibitors have also been designed for the microtubule-severing enzyme spastin (Steinman and Kapoor, 2019). The pyrazolyl-pyrrolopyrimidine-based compound, spastazoline, targets the active site of human and *Drosophila melanogaster* spastin and impairs ATP-dependent microtubule severing *in vitro* (Figure 1.2) (Cupido et al., 2019; Pisa et al., 2019a). This inhibitor was designed based on a hit from a limited screen of 33 chemically diverse kinase inhibitors that could mimic hydrogen-bonding interactions made by adenine in the AAA active site (Cupido et al., 2019). Through computational docking and mutagenesis studies, the compound's selectivity for spastin was optimized, as indicated by the lack of ATPase inhibition of four related AAA proteins (20 μM spastazoline) and 65 kinases (2 μM spastazoline) (Cupido et al., 2019). These approaches revealed that spastazoline forms a network of hydrogen bonding interactions with backbone residues in the N-loop motif. A subsequent study provided a structural model of *Drosophila melanogaster* spastin in the presence of a spastazoline analog, revealing a binding pose that is similar to that proposed for spastazoline (Pisa et al., 2019b). Taken together, these studies suggest that spastazoline can be a useful cellular probe for spastin.

A second ATP competitive inhibitor of spastin was designed based on JNJ-7706621, an inhibitor of cyclin-dependent and Janus kinases (Figure 1.2) (Lin et al., 2005). JNJ-7706621 blocks the ATPase activity of spastin and the related AAA proteins katanin and fidgetin-like 1 (FIGL1) (Pisa et al., 2019b). To examine the binding mode of JNJ-7706621 in spastin, mutations were designed in the N-loop, P-loop and sensor II motifs that did not impair the biochemical activity of the protein, but could affect inhibitor potency (Pisa et al., 2019b). This was achieved by substituting less conserved residues, known as variability hotspots, with those found at equivalent

positions in related AAA proteins. These analyses revealed that a mutation in the sensor II motif (T692A) increased the potency of JNJ-7706621 by ~7-fold, while a mutation in either the P-loop or N-loop motif resulted in less than a ~2-fold change in inhibitor potency (Pisa et al., 2019b). Indeed, an X-ray structure of *D. melanogaster* spastin (2.3 Å) in the presence of JNJ-7706621 revealed that the inhibitor forms hydrogen-bonding interactions with T692 and residues in the P loop and N loop motif that are not in a variability hotspot position (Pisa et al., 2019b).

A derivative of JNJ-7706621 was designed that retained the diaminotriazole core, likely maintaining the hydrogen-bonding interactions with spastin's active sites residues (Figure 1.2). This derivative potently inhibits spastin, but not FIGL1, VPS4B and katanin. Unexpectedly, an X-ray structure of *D. melanogaster* spastin in the presence of the derivative revealed that the compound forms a network of hydrogen bonding interactions with the backbone of residues in the N-loop motif, as is the case for spastazoline. Thus, these studies revealed that a promiscuous AAA inhibitor can be modified to achieve selective inhibition of one AAA protein.

The design of chemical inhibitors of spastin and VCP/p97 is more readily achievable compared to developing probes for large AAA proteins, such as midasin. Ribozinoindoles or Rbins are small molecule inhibitors of ribosome biogenesis that inhibit the ATPase activity of recombinant midasin (Kawashima et al., 2016). A single-point mutation (F1093L) in midasin was capable of blocking Rbin activity *in vitro* and in cells, indicating that midasin is the physiological target of Rbins (Kawashima et al., 2016).

The *S. cerevisiae* ortholog of midasin, Rea1, is better characterized than its human counterpart, and has been proposed to remodel both nucleolar and nucleoplasmic pre-60S particles (Bassler et al., 2010; Ulbrich et al., 2009). Midasin contains a small domain at the N terminus (N domain) followed by six AAA domains and a 'tail' that consists of the linker, Asp/Glu-rich (D/E-

rich) and MIDAS domain. In *S. pombe* Rea1, the AAA1 and AAA6 domains lack the DE (Asp-Glu) residues in the Walker B motif that are necessary for ATP hydrolysis, suggesting that only the AAA2-AAA5 domains have ATPase activity. Notably, eight mutations that affect Rbin-1 potency all map to the AAA3-S and AAA4-L subdomains, suggesting that the AAA3 site is involved in the compound's mechanism of inhibition (Kawashima et al., 2016). Cryo-EM studies of midasin in the presence of ATP and Rbin-1 revealed that these two ligands trap the protein in a conformational state where the MIDAS domain is docked onto the AAA ring, suggesting that nucleotide-dependent conformational changes in the AAA ring can be transmitted to the C-terminal tail. Thus, studies with Rbins provide an example where small molecules inhibitors can be utilized to trap AAA proteins in distinct conformational states, providing insights into their function.

In the next subchapters, we review the recent advances in developing chemical inhibitors of dynein. We highlight the ciliobrevins, cell-permeable inhibitors of dynein, and the dynapyrazoles, a class of inhibitors that address some of the limitations of the ciliobrevins. We discuss their discovery, use, and how these classes of inhibitors can be improved.

1.3 Chemical inhibitors of dynein

Intracellular transport of organelles, vesicles and cellular proteins are critical for the structural and functional organization of eukaryotic cells. This process is driven by two molecular motors, kinesins and cytoplasmic dyneins, which couple the energy from ATP hydrolysis to transport cellular cargo along polarized microtubule networks (Bhabha et al., 2016). Dyneins move toward the microtubule minus ends (retrograde transport), while kinesins move toward the microtubule plus ends (anterograde transport). The kinesin superfamily contains at least 45 isoforms that are responsible for the transport of specific cellular cargos (Hirokawa et al., 2009).

In contrast, a single isoform of dynein is responsible for most of the retrograde transport in the cell (Roossien et al., 2015). Despite dynein's essential role in intracellular transport, it remains the least understood cytoskeletal motor.

In metazoan cells, two isoforms of cytoplasmic dynein are present, where dynein 1 is responsible for intracellular transport and dynein 2 is restricted to motile and sensory cilia (Roossien et al., 2015). Both isoforms contain a ~380 kDa motor domain that belongs to the AAA (ATPase Associated with various Activities) superfamily. Though the dynein 1 and 2 motor domains share a low sequence identity (30%), they are structurally similar and consist of a hexameric ring of six distinct AAA domains within a single polypeptide, an N-terminal linker, a buttress/strut and a coiled-coil stalk that includes the microtubule binding domain (MTBD) (Figure 1.3) (Roberts, 2018). The buttress emanates from the AAA5 domain and interacts with the stalk to change its microtubule binding affinity. To undergo motility, dynein must coordinate the conformations of these structural elements.

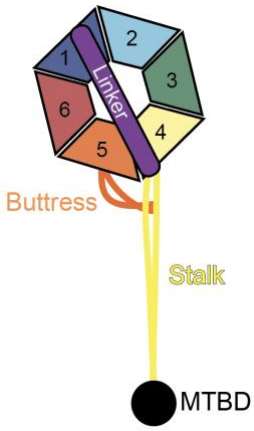

Figure 1.3 Schematic of dynein's motor domain. The AAA1 (blue), AAA2 (light blue), AAA3 (green), AAA4 (yellow), AAA5 (orange) and AAA6 (red) domains are shown. The buttress (orange), stalk (yellow), linker (purple) and the microtubule-binding domain (MTBD, black) are depicted.

Each of dynein's six AAA domains has a distinct role in dynein's chemomechanical cycle and is comprised of a AAA-L (large) and AAA-S (small) subdomain that together with a neighboring AAA-L subdomain form a tripartite interface where nucleotide binding and hydrolysis can occur (Schmidt and Carter, 2016). The first four AAA domains (AAA1-AAA4) contain the Walker A motifs necessary for ATP binding while the AAA5 and AAA6 domains have nucleotide-independent structural roles. Only the AAA1 domain is required for dynein's motility and is considered the main catalytic site (Gibbons and Gibbons, 1987; Kon et al., 2004). The AAA2 domain lacks the catalytic glutamate in the Walker B motif that is necessary for nucleotide hydrolysis, and likely constitutively binds ATP. The AAA3 domain allosterically regulates the activity of AAA1, while the AAA4 domain, which contains the catalytic residues needed for ATP binding and hydrolysis, is not well understood. Current models indicate that ATP binding at the AAA1 site results in closure of the AAA1 nucleotide-binding pocket, which leads to a rigid-body movement of AAA2/AAA3/AAA4 towards the linker. These domain motions are propagated to the AAA5 and AAA6 domains, which result in sliding of the buttress relative to the stalk and the bending of the linker domain. Despite progress in understanding the architecture and function of dynein's motor domain, the roles of the AAA2-AAA6 domains have yet to be fully elucidated.

Cytoplasmic dyneins have intricate allosteric communcations in the motor domain that appear to differ among orthologs. In *S. cerevisiae* dynein, the AAA3 domain was proposed to regulate ATP turnover at the AAA1 site. Specifically, a mutation that blocks ATP hydrolysis in the AAA3 site resulted in a ~10-fold decrease in the protein's overall ATPase rate in the absence and presence of microtubules (Cho et al., 2008). The same mutation in the AAA4 site resulted in only a ~1.5-fold decrease in dynein's overall ATPase rate, suggesting that AAA4 has less of a role in regulating AAA1's activity (Cho et al., 2008). Consistent with these data, cryo-EM

reconstructions of the *S. cerevisiae* motor domain containing a Walker B mutation in the AAA3 domain revealed that the linker remained extended in the presence of ATP (Bhabha et al., 2014). In contrast, 3D classification of WT particles in the presence of ATP showed conformations where the linker is bent, as expected when AAA1 site is occupied by the nucleotide (Bhabha et al., 2014). These data suggested that ATP-binding to the AAA3 site blocks the activity of the AAA1 site. ATP binding to AAA3 site is therefore expected to lead to unregulated ATP turnover at the AAA1 site, which is observed when ATP binding is blocked (Walker A mutation) in the AAA3 site of human dynein 1 (Steinman et al., 2017).

The allosteric communication observed in the *S. cerevisiae* and human dynein 1 may not extend to dynein 2. In the AAA3 domain of dynein 2, the residues in the Walker B motif are lysine and aspartate (KD) rather than the catalytic aspartate and glutamate (DE), suggesting that site is unlikely to support ATP hydrolysis (Schmidt et al., 2015). This difference indicates that the allosteric communication in dynein 2's AAA ring may differ from that in dynein 1.

In cells, dynein transports cargo at fast speeds (~25-100 μm/min) and can therefore complete a cellular process within seconds to minutes timescales (He et al., 2014; Mijalkovic et al., 2017; Steinman et al., 2017). Small molecule probes can be powerful tools for studying dynein's cellular functions, as they can perturb protein function within the timescale of dynein action. However, the design of potent (<1 μM) and selective inhibitors of dynein has been difficult to achieve, largely due to the complexity of dynein's architecture and function.

1.4 Ciliobrevins, cell permeable inhibitors of dynein

The ciliobrevins were discovered in a high-throughput screen for Hedgehog (Hh) pathway inhibitors (Firestone et al., 2012). A limited structure-activity relationship (SAR) analyses yielded four analogs that were named ciliobrevins A-D due to their effects on the cilium length (Firestone et al., 2012). Briefly, Hh signaling occurs in the primary cilium, a microtubule-based antennae-like structure that emanates from the cell body, and controls vertebrae embryonic development and tissue differentiation (Briscoe and Thérond 2013). To activate this pathway, the Sonic Hedgehog ligand binds to the transmembrane protein Patched1 and inhibits its localization into the cilium (Rohatgi et al., 2007). Inhibition of Patched1 allows the seven-transmembrane protein, Smoothened (Smo), to accumulate in the ciliary membrane, triggering a signaling cascade that results in the transcription of downstream Hh responsive genes through the Gli family of proteins (Figure 1.4). The proteolytic processing of Gli to its activated form depends on intraflagellar transport (IFT), a motor-driven process where kinesin 2 and dynein 2 transport the cargoes required for the assembly and maintenance of the cilium (Figure 1.4) (Ishikawa and Marshall, 2017). Knockdown of dynein 2 results in the accumulation of Gli2 in the cilium, and leads to impaired activator and repressor functions of Gli (Kim et al., 2009). Consistent with inhibition of dynein 2, treating cells with the ciliobrevins resulted in an accumulation of Gli2 and IFT88 at the cilium, suggesting that these inhibitors target retrograde transport (Firestone et al., 2012).

The aberrant activation of the Hedgehog pathway has been shown to cause cancer in humans, such as those in the skin, brain, pancreas, gastrointestinal tract, and prostate.(Liao et al., 2009) Hedgehog-driven malignancies can be driven by mutations in one or more Hh pathway genes, most commonly *PTCH1* (Ridky and Cotsarelis, 2015). Vismodegib is a Smo antagonist that is clinically approved for the treatment of basal cell carcinomas, but at least 20% of tumors can

acquire resistance-conferring mutations in Smo (Axelson et al., 2013; Ridky and Cotsarelis, 2015). Due to the high frequency of resistance-conferring mutations upon vismodegib treatment, Hh pathway inhibitors that act downstream of Smo are needed. Dynein-2 specific inhibitors that inhibit Hedgehog signaling, but do not block ciliogenesis, could be powerful therapeutic tools to treat Hh-driven cancers. However, the currently available dynein inhibitors target both dynein 1 and 2, resulting in cell cytotoxicity due to inhibition of dynein 1's housekeeping functions.

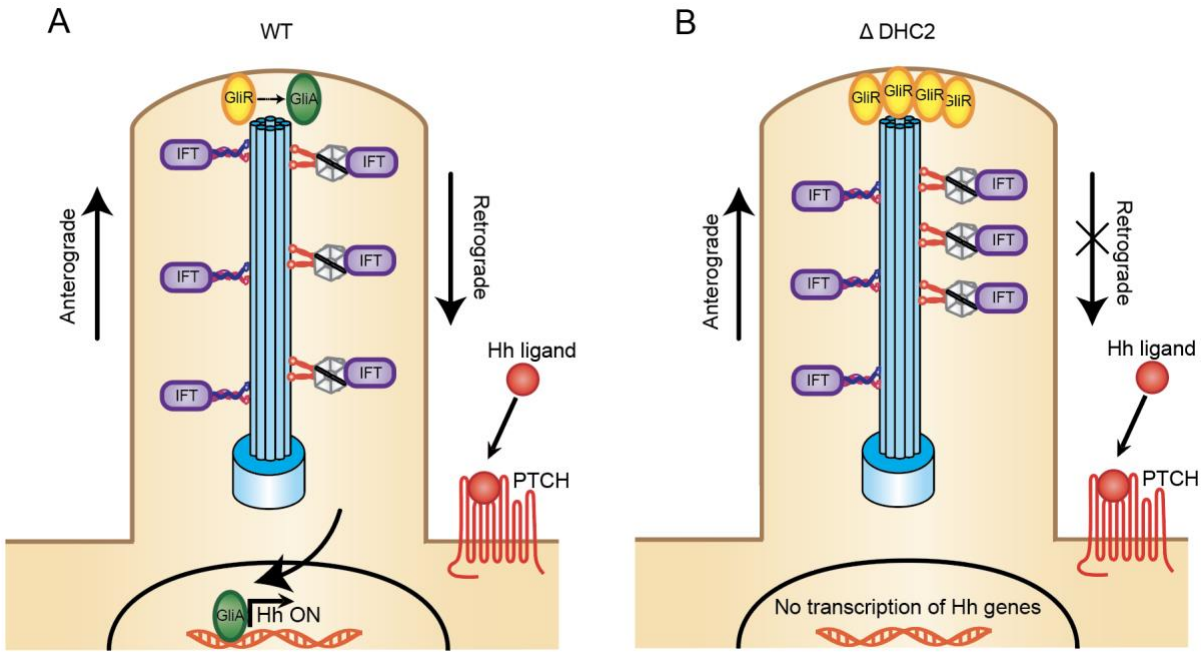

Figure 1.4 Schematic of intraflagellar transport along the cilium. (A) Transport of intraflagellar transport (IFT) cargoes (purple) is required for the localization and activation of Gli repressor (GliR, yellow). Activated Gli (GliA, green) exits the cilium and turns on the transcription of Hedgehog target genes in the nucleus. (B) Deletion of dynein 2 results in inhibition of retrograde transport, preventing the activation of GliR. GliR accumulates at the tip of the cilium and is unable to localize to the nucleus.

Ciliobrevins were confirmed to inhibit dynein after biochemical studies showed inhibition of microtubule gliding driven by dynein 1 purified from bovine brain and of the ATPase activity

of the rat dynein 1 motor domain (Firestone et al., 2012). Follow-up studies showed that ciliobrevins inhibit the ATPase activity of the human dynein 1 and 2 motor domains with a half-maximal inhibitory concentration (IC_{50}) of ~50 μM (See et al., 2016; Steinman et al., 2017).

Ciliobrevins have been used as small molecule probes to study the role of dynein in IFT, primary neurons, and in the transport of mTOR towards the perinuclear domain (Roossien et al., 2015). However, their use in cell-based assays has been treated with caution, as complete dynein inhibition can require high doses (50-100 μM), and selective protein target inhibition can be difficult to achieve at these concentrations (Roossien et al., 2015). Additionally, the selectivity of the ciliobrevins has not been addressed, and it is possible that these inhibitors may also target other proteins in the AAA superfamily (Roossien et al., 2015). Taken together, ciliobrevins are cell permeable inhibitors of dynein, but like many inhibitors identified through high-throughput screens, they require chemical optimization to improve potency and selectivity.

A recent study identified the key pharmacophore of the ciliobrevins that is needed to maintain dynein inhibition (See et al., 2016). The ciliobrevins are 2,4-dichlorobenzoyl dihydroquinazolinones composed of an acrylonitrile moiety and three ring systems: rings A and B comprise the quinazolinone unit, and ring C represents the benzoyl group (Figure 1.5). Limited SAR analyses suggested that the quinazolinone carbonyl, the amide NH 2,4-substituted C ring, and the nitrile group are essential for dynein inhibition (Firestone et al., 2012; See et al., 2016). These data led to efforts to optimize the ciliobrevin pharmacophore by designing analogs that retained the moieties that are essential for dynein inhibition but contained modifications in the 7-position of the A ring. These derivatives were found to preferentially inhibit dynein 2 over dynein 1 in ATPase and cell-based assays (See et al., 2016), but further optimization of the ciliobrevin pharmacophore will be needed to design inhibitors that inhibit only one isoform of dynein.

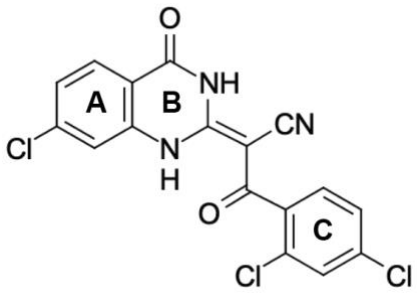

Figure 1.5 Chemical structure of ciliobrevin D.

1.5 Dynapyrazoles, dynein inhibitors with a distinct mechanism of inhibition

Efforts to optimize the ciliobrevin pharmacophore continued with the design of the dynapyrazoles. The ciliobrevins contain a benzoylacrylonitrile functional group that has the potential to isomerize about the benzoylacrylonitrile olefin. Restricting the geometry of the scaffold was hypothesized to lead to improvements in potency and compound stability, but the preferred isomer of the ciliobrevins had not been previously identified (Steinman et al., 2017). Attempts to crystallize ciliobrevin D were unsuccessful, and a derivative with a 2-morpholinoethyl ether substitution was subsequently synthesized and found to readily crystallize (Steinman et al., 2017). X-ray data showed that the derivative exists as a single isomer with an E-olefin configuration, and heterocyclic scaffolds that maintained this geometry were designed. Specifically, the benzoylacrylonitrile-quinazolinone system of the ciliobrevins was replaced by a tricyclic pyrazoloquinazolinone with substitutions at the 6-position of the A ring (Figure 1.6). Of these scaffolds, the compound with a 6-iodo substitution (termed dynapyrazole-A) was shown to inhibit the human dynein 1 and 2-driven microtubule gliding with an IC_{50} of 2.3 ± 1.4 μM and 2.6 ± 1.3 μM, respectively, which is approximately eightfold more potent than ciliobrevin D (Figure 1.6) (Steinman et al., 2017). Additionally, an analog with a 6-trifluoromethyl substitution (termed dynapyrazole-B) inhibited dynein 2-driven microtubule gliding with a potency similar to that of

dynapyrazole-A (IC_{50}: 2.9 ± 0.6 μM) (Figure 1.6). Dynapyrazole-A and -B are collectively known as the dynapyrazoles.

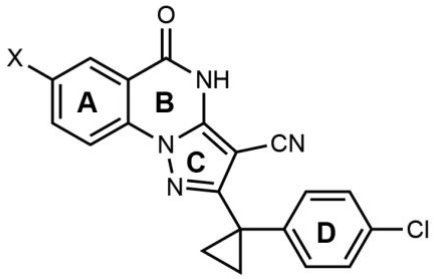

Figure 1.6 Chemical structure of dynapyrazole-A (X=I) and dynapyrazole-B ($X=CF_3$).

Unexpectedly, ATPase assays of human dynein 1 revealed that dynapyrazole-A strongly blocks dynein's ATPase activity only in the presence of microtubules (Steinman et al., 2017). This result suggested that dynapyrazole-A has a distinct mechanism of action, given that ciliobrevins inhibit dynein's ATPase activity in the absence and presence of microtubules. However, it is unclear how modifications in the ciliobrevin scaffold lead to such changes, as it is unknown which of dynein's many potential inhibitor-binding sites the ciliobrevins and dynapyrazoles target.

To understand how dynapyrazole-A inhibits dynein's ATPase activity, ADP-vanadate-dependent photocleavage of human dynein 1 was measured in the presence of inhibitor. This assay is an established read-out of ATP hydrolysis at the AAA1 domain, as the ADP-vanadate complex is only capable of forming in this site (Gibbons and Gibbons, 1987). Dynapyrazole-A (4 μM) reduced the ADP-vanadate-dependent photocleavage of human dynein 1 by ~2.5-fold relative to the DMSO control, suggesting that the inhibitor targets the ability of the AAA1 site to hydrolyze ATP (Steinman et al., 2017). However, given the complexity of dynein's motor domain, it is unclear whether inhibition of the ATPase activity at the AAA1 site is due to direct binding to the

AAA1 domain or to an allosteric site in dynein that regulates the activity of AAA1, such as the AAA3 domain.

To determine if dynapyrazole-A binds to the AAA3 domain, the catalytic lysine in the Walker A motif of the AAA3 site was mutated to an alanine (K1912A). This mutation resulted in an increase in human dynein 1's overall ATPase activity, consistent with the AAA3 domain acting as an allosteric regulator of the AAA1 site (Bhabha et al., 2014; DeWitt et al., 2015). Surprisingly, a dose-dependent analysis showed that dynapyrazole-A inhibited the basal ATPase activity of the AAA3 mutant with an IC_{50} of 5.5 ± 1.6 μM, suggesting that the AAA3 domain is not involved in dynapyrazole-A's mechanism of inhibition (Steinman et al., 2017). Based on this data, and the ADP-vanadate-dependent photocleavage experiments, dynapyrazole-A was proposed to target the AAA1 site. However, further studies will be needed to unambiguously identify the binding site(s) of dynapyrazole-A in dynein.

Consistent with these biochemical studies, dynapyrazole-A inhibits dynein 1 and 2 dependent cellular processes. Specifically, dynapyrazole-A inhibits lysozyme transport in the neurites of CAD cells, a murine cell line that displays neuron-like properties in serum-free cell culture media (Steinman et al., 2017). The bidirectional transport of lysosomes requires kinesins and dynein 1, where disruption of dynein-driven transport results in the inhibition of bidirectional lysosome motility (Barlan et al., 2013). Treatment of CAD neurites with dynapyrazole-A (3.5 μM) suppresses the bidirectional transport of lysosomes at a dose (3.5 μM) that is consistent with the IC_{50} observed for dynein 1-driven microtubule gliding. Additionally, dose-dependent analysis revealed that dynayrazole inhibits Hedgehog pathway activation with an IC_{50} of 1.9 ± 0.6 μM, which can be measured in a murine cell line (Shh-Light2) that expresses a Gli-driven luciferase reporter (Chen et al., 2002; Taipale et al., 2000). These data show that dynapyrazole-A can inhibit

dynein dependent cellular processes and suggest that dynapyrazole-A may be a useful small molecule probe to study dynein function.

1.6 Dynarrestin, a dynein inhibitor with an ATPase-independent mechanism

Dynarrestin is an aminothiazole that was identified in a high-throughput screen for Hedgehog pathway inhibitors (Figure 1.7) (Höing et al., 2018). Dose-dependent analysis showed that dyanarrestin inhibits Gli-driven luciferase expression in Shh-Light2 cells with an IC_{50} of 0.22 μM (Höing et al., 2018). The cellular target of dynarrestin was determined using an unbiased approach in which dynarrestin was conjugated to a biotin tag (compound L568) to pull down interacting proteins for identification via liquid chromatography and label-free quantitative (LFQ) tandem mass spectrometry (LC-MS/MS) (Figure 1.7). This analysis revealed that compound L568 binds to dynein heavy chain (DYNC1H1) and light chain Tctex-1 (DYNLT1) in C3H10T1/2 and Shh-Light2 cells. A pull-down experiment using purified native dynein 1 from bovine brain confirmed that compound L568, and therefore dynarrestin, binds to dynein (Höing et al., 2018).

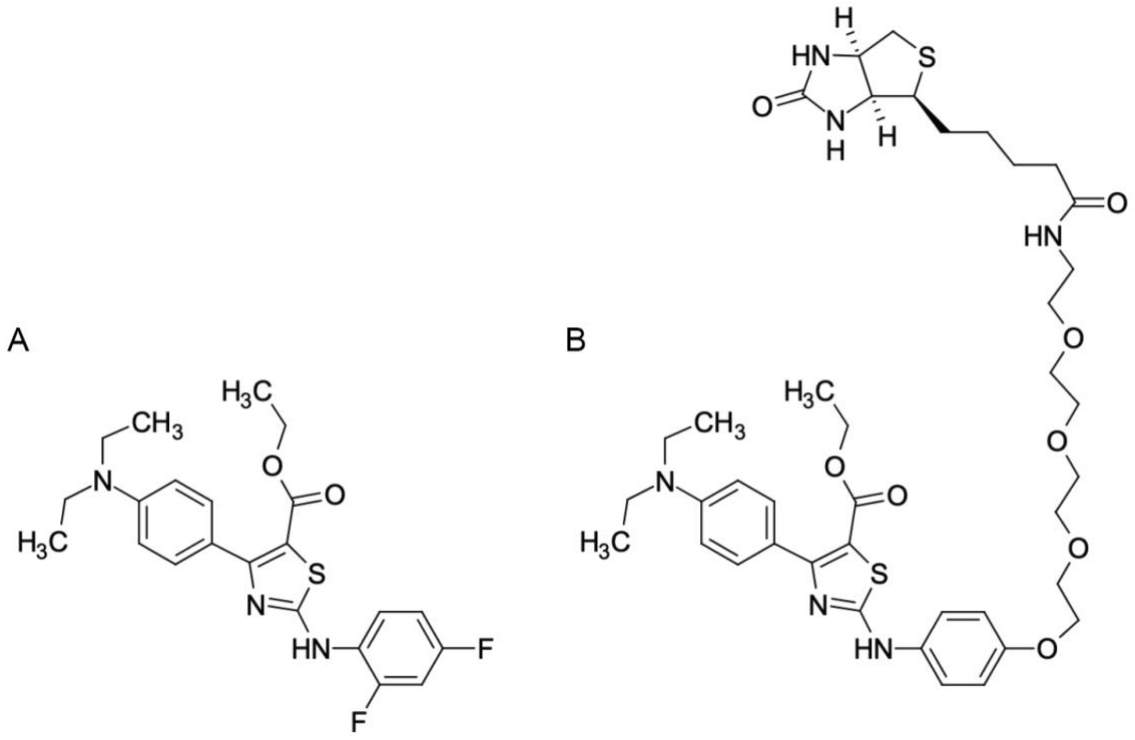

Figure 1.7 Chemical structure of dynarrestin (A) and the active probe compound L568 (B).

Dynarrestin inhibits dynein 1-driven microtubule gliding in a dose-dependent manner (IC_{50}: 5 μM) by decreasing dynein's ability to bind microtubules, which is reversible upon drug washout (Höing et al., 2018). The few microtubules that were bound to dynein showed a decrease in velocity, albeit at a higher concentration of compound (50 μM). Notably, dynarrestin had no effect on kinesin-1 dependent microtubule gliding and did not significantly inhibit the activity of 422 kinases in a kinome-wide ATP-competition assay (Höing et al., 2018). These results suggest that dynarrestin is a direct and specific inhibitor of dynein 1.

Dynarrestin has a distinct mechanism of action compared to the ciliobrevins and dynapyrazoles. Interestingly, dynarrestin did not inhibit the microtubule-stimulated ATPase activity of native dynein 1 purified from bovine brain even at a high concentration of the compound (100 μM) (Höing et al., 2018). This data suggests that dynarrestin inhibits dynein by decoupling ATP hydrolysis from the protein's microtubule binding cycle. A similar mechanism of action has

been proposed for the cofactor Lis1, which regulates microtubule binding and release without affecting ATPase activity (Huang et al., 2012). Based on these data, dynarrestin may not target the AAA ATPase sites in the motor domain, but the inhibitor-binding site has yet to be identified.

Dynarrestin was found to inhibit both dynein 1 and 2 dynein dependent cellular processes. Dynarrestin inhibits the bidirectional movement of endosomes in Cos-7 and IMCD3 cells in a dose-dependent manner (IC50 = 4.2 μM and 3.7 μM, respectively) and is consistent with studies that proposed that kinesins and dynein 1 are functionally coupled on endosomes (Granger et al., 2014; Yeh et al., 2012). In Cos-7 mitotic cells, dynarrestin treatment decreased the number of cells in anaphase, metaphase, and telophase and affected the orientation and pole-to-pole distance of the mitotic spindle (Höing et al., 2018)/ Despite evidence for dynein 1 inhibition in cells, dynarrestin is not cytotoxic to Cos-7 and Shh-Light2 cells, raising the question for how inhibition of an essential protein can result in functional cells.

Dynarrestin also potently inhibits intraflagellar transport in the primary cilium. Specifically, treating IMCD3 cells for one hour with dynarrestin (125 nM) reduces the velocities and frequencies of anterograde and retrograde moving IFT88-GFP foci (Höing et al., 2018). This phenotype can be reproduced by treating IMCD3 cells with ciliobrevin for 30 min, albeit at a higher concentration of compound (15 μM). Unlike the ciliobrevins, dynarrestin did not affect cilia formation after overnight treatment in serum-free culture media, suggesting that this inhibitor can suppress Hedgehog signaling in the cilium without affecting ciliogenesis (Höing et al., 2018).

Based on these phenotypes, dynarrestin was tested for the ability to suppress the proliferation of primary medulloblastoma (MB) cells that lack a copy of patched (*Ptch*−/+), resulting in the upregulation of Hh signaling (Höing et al., 2018). Vismodegib and dynnarestin inhibited proliferation of these cells with similar potencies (IC_{50}: 22 and 68 nM, respectively)

(Höing et al., 2018). Notably, treatment of MB cells with dynarrestin and the Smo agonist, SAG, does not affect dynarrestin's ability to suppress the proliferation of these cells (IC_{50}: 350 nM). In contrast, vismodegib is not toxic to MB cells in the presence of SAG, indicating that the Smo agonist and antagonist are competing for the same target. These results are consistent with dynarrestin acting downstream of Smo to inhibit the proliferation of a Hh-driven cancer.

Taken together, dynarrestin is a more potent inhibitor of dynein 1 and dynein 2 driven cellular processes relative to the potencies of ciliobrevins and dynapyrazoles. This inhibitor has a distinct mechanism of action, where it inhibits dynein's motility without disrupting ATP hydrolysis. Based on the specificity data, dynarrestin may be a useful probe, though its activity against other proteins in the AAA superfamily has been addressed. Like the ciliobrevins and dynapyrazoles, further studies will be needed to determine the dynarrestin's binding site in dynein.

Chapter 2: Dynapyrazoles acutely inhibit intraflagellar transport

2.1 Introduction

Intraflagellar transport (IFT) is required for the assembly and maintenance of primary and motile cilia (Prevo et al., 2017). As cilia cannot synthesize proteins, the proteins required for ciliary assembly must be transported from the cell body and into the cilium by IFT (Ishikawa and Marshall, 2017). Motors of the kinesin 2 family transport ciliary precursors, such as tubulin, pre-assembled radial-spoke complexes and dynein arms, for incorporation into their site of assembly at the tip of the cilium, while dynein 2, or IFT-dynein, recycle turnover products from the tip of the cilium to the base (Prevo et al., 2017). These motors assemble with IFT particles to form IFT trains, which function as adaptors to allow other proteins to be transported (Lechtreck, 2015). Anterograde IFT is necessary for ciliary assembly, while retrograde IFT appears dispensable for this process (Burghoorn et al., 2007; Engel et al., 2012, 2009).

Inhibitors of intraflagellar transport can be useful tools to dissect IFT and its relation to ciliogenesis. Currently, it is unclear how retrograde IFT is coupled to cilium length and maintenance and which proteins and receptors involved in signaling pathways in the cilium are dependent on IFT for their localization. To address these questions, perturbation tools that allow for real-time and controlled inhibition are required.

Ciliobrevins have been used as probes to study IFT functions due to their ability to acutely inhibit ($\leq$ 5 min) this process in both *Caenorhabditis elegans* and in mammalian cell lines (Mijalkovic and Peterman, 2019; See et al., 2016). Specifically, the controlled perturbation of dynein 2 in *C. elegans* by ciliobrevin D allowed investigators to determine that maintenance of ciliary length requires a high fraction of active dynein 2 motors, while the cilium's structural integrity can be maintained with a few active motors (Mijalkovic and Peterman, 2019). These

results would be difficult to obtain with the use of gene editing and expression tools, such as CRISPR and RNAi, as these approaches would lead to long-term cellular changes that would be difficult to correlate to dynein function. However, ciliobrevins require high doses (≥50 μM) to achieve IFT inhibition (Mijalkovic and Peterman, 2019; Ye et al., 2013), which can result in off-target effects and cytotoxicity. More potent inhibitors of dynein 2 are therefore required.

Dynapyrazoles inhibit dynein 2 in biochemical assays and blocks Hedgehog pathway activation at single digit micromolar concentrations (Steinman et al., 2017). Based on these data, it was hypothesized that the dynapyrazoles can inhibit intraflagellar transport at a similar potency. In this chapter, I describe the results from an assay that can monitor intraflagellar transport in the absence or presence of dynapyrazole-A.

2.2 Results

Note to readers: the results discussed below were published in Jonathan Steinman's first-author paper (Steinman et al., 2017) and arose from experiments and analyses that I have performed.

I used spinning-disk confocal microscopy to examine the dynamics of fluorescently labeled intraflagellar transport protein-88 (mNeonGreen-IFT88, Figure 2.1A-C) in the presence of either DMSO or dynapyrazole-A (5 μM) (See et al., 2016; Ye et al., 2013). An established convention allows the wider end of the cilium to be identified as the base, omitting the need for a centrosomal marker (Yang et al., 2015). Time-lapse recordings of cells treated with the vehicle control (0.3% DMSO) revealed anterograde and retrograde moving IFT88 punctae (Yang et al., 2015). In cilia treated with dynapyrazole-A (5 μM), the velocities of retrograde-directed IFT88 punctae are reduced. In contrast, dynapyrazole-A did not appear to inhibit anterograde motion.

To determine the effect of dynapyrazole-A on the velocities and frequencies of IFT88 punctae, I analyzed time-lapse images of cilia using KymographClear and KymographDirect

(Mangeol et al., 2016). These algorithms extract anterograde and retrograde moving particles from kymographs and quantify their velocities (Mangeol et al., 2016). Under control conditions (0.3% DMSO, Figure 2.1B), anterograde particles moved with a mean velocity of 694 ± 117 nm/s (Figure 2.1D and F, mean ± S.D., 429 particles, 38 cilia) and retrograde particles moved at 421 ± 156 nm/s (Figure 2.1D and F, 244 particles, 38 cilia), consistent with a previous study (Ye et al., 2013). Relative to the vehicle control, a short (5 min) incubation with dynapyrazole-A (5 μM) reduced the speed of retrograde particles by ~63% (Figure 2.1C, E and F; mean velocity 156 ± 107 nm/s, 211 particles, 52 cilia). In contrast, anterograde particle velocities were only reduced by ~18% (Figure 2.1C, E and F, 566 ± 116 nm/s, 443 particles, 52 cilia). Dynapyrazole-A treatment (5 μM) also reduced the frequency, or the number of particles moving across a cilium per minute, in both anterograde and retrograde directions by ~25 and ~37%, respectively (Figure 2.1G). These data suggest that dynapyrazole-A reduces the frequency of particles in both directions, but more strongly inhibits the velocities of retrograde-directed particles.

Figure 2.1 Effect of dynapyrazole-A on intraflagellar transport A) Schematic of a cilium showing the microtubule-based axoneme (blue) and dynein (black) transporting an intraflagellar transport particle (purple) containing mNeonGreen-IFT88 (green). Anterograde and retrograde transport directions are indicated. (B–C) Images from time-lapse series and associated kymographs showing motion of mNeonGreen-IFT88-containing particles in primary cilia of murine kidney cells (IMCD3). Cilium tip (red arrowhead) and base (black arrowhead) are indicated. Red (retrograde) and blue (anterograde) traces have been added to one kymograph per condition to illustrate particle tracks. Image scale bar, 3 μm; Kymograph horizontal scale bar, 10 s; kymograph vertical scale bar, 3 μm. (D–E) Velocity distribution histograms showing anterograde and retrograde velocities in the vehicle control (0.3% DMSO, D) and in the presence of dynapyrazole-A (DP-A, 5 μM) (E) at 5 min after initiation of experiment. Intraflagellar transport velocities (F) and frequencies (G) after washout of dynapyrazole-A (DP-A). Bars represent mean + S.D. Data analysis (Va, anterograde velocity, nm/s; Vr, retrograde velocity, nm/s; Fa, anterograde frequency, counts/minute; Fr, retrograde frequency, counts/minute; values are mean ± S.D. Na, number of anterograde particles analyzed; Nr, number of retrograde particles analyzed; C, number of cilia analyzed). DMSO, Va 694 ± 117, Vr 421 ± 156, Fa 11.3 ± 3, Fr 6.5 ± 4, Na 429, Nr 244, C 38; 5 μM 8, Va 566 ± 116, Vr 156 ± 107, Fa 8.5 ± 5, Fr 4.1 ± 3, Na 443, Nr 211, C 52; Washout, Va 697 ± 149, Vr 467 ± 136, Fa 14.2 ± 6, Fr 9.6 ± 7, Na 256, Nr 173, C 18.

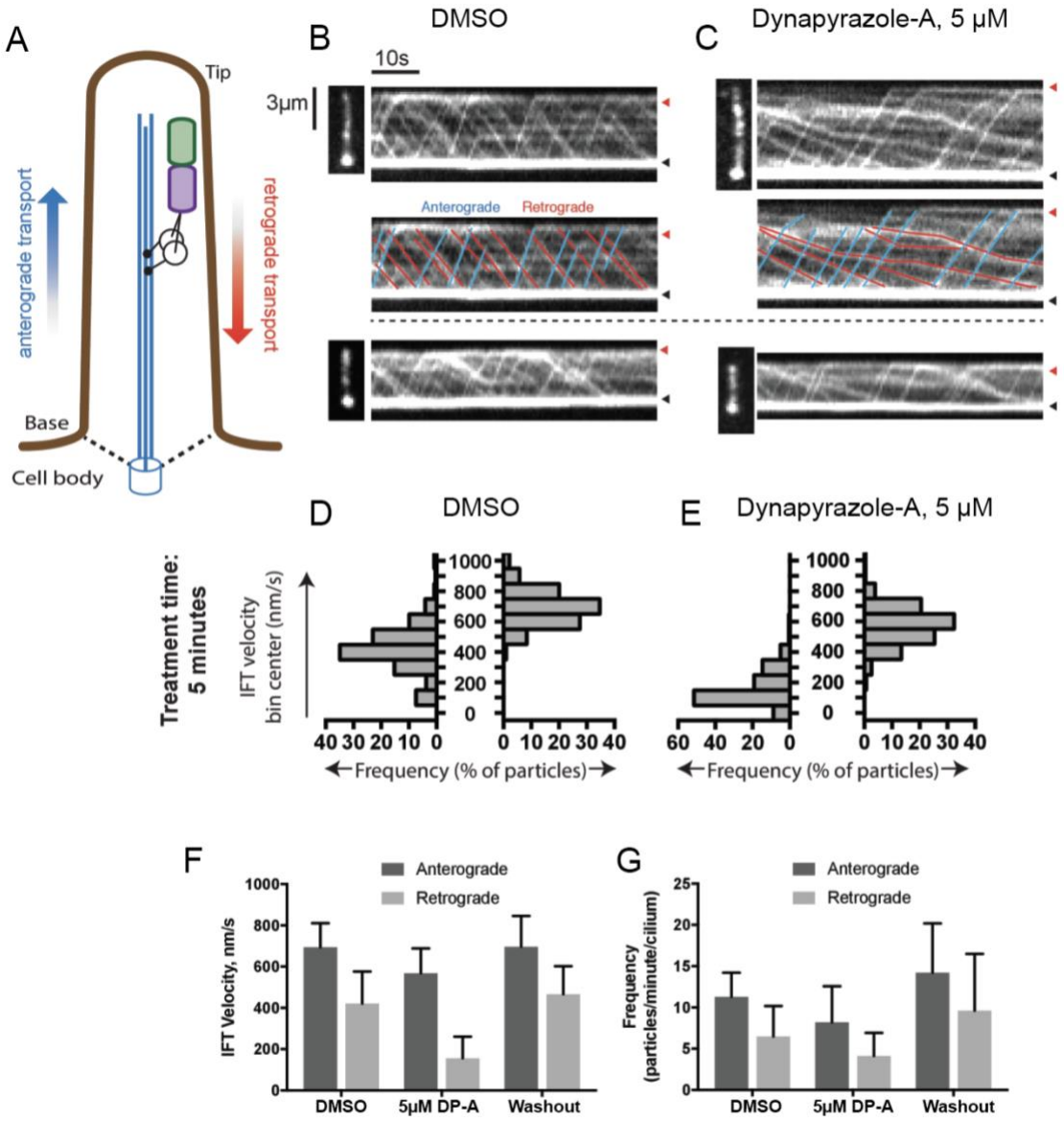
A
Tip
anterograde transport
retrograde transport
Base
Cell body
B
DMSO
10s
3µm
Anterograde
Retrograde
C
Dynapyrazole-A, 5 µM
D
DMSO
E
Dynapyrazole-A, 5 µM
Treatment time:
5 minutes
IFT velocity
bin center (nm/s)
1000
800
600
400
200
0
40 30 20 10 0
0 10 20 30 40
60 40 20 0
Frequency (% of particles)
F
Anterograde
Retrograde
IFT Velocity, nm/s
DMSO
5µM DP-A
Washout
G
Frequency
(particles/minute/cilium)
25
20
15
10
5
0

We next examined if increasing the duration or concentration of dynapyrazole-A could further reduce IFT particle velocities and frequencies. Extending the dynapyrazole-A incubation time to 10 min reduced the velocities of anterograde or retrograde-moving particles by ~13 and ~65%, respectively, but are similar to the percent reductions observed at the 5 min time point (Figure 2.2A-C). The frequencies of anterograde and retrograde-directed particles also decreased by ~32 and ~14%, respectively, but are not further reduced compared to the percent reductions at 5 min. Treatment of cilia with a higher dynapyrazole-A concentration (10 μM, 5 min incubation) also did not substantially reduce the velocities and frequencies of anterograde and retrograde-motion (Figure 2.3A-C). These data show that dynapyrazole-A treatment at the indicated doses and incubation times inhibits IFT but does not abolish this process.

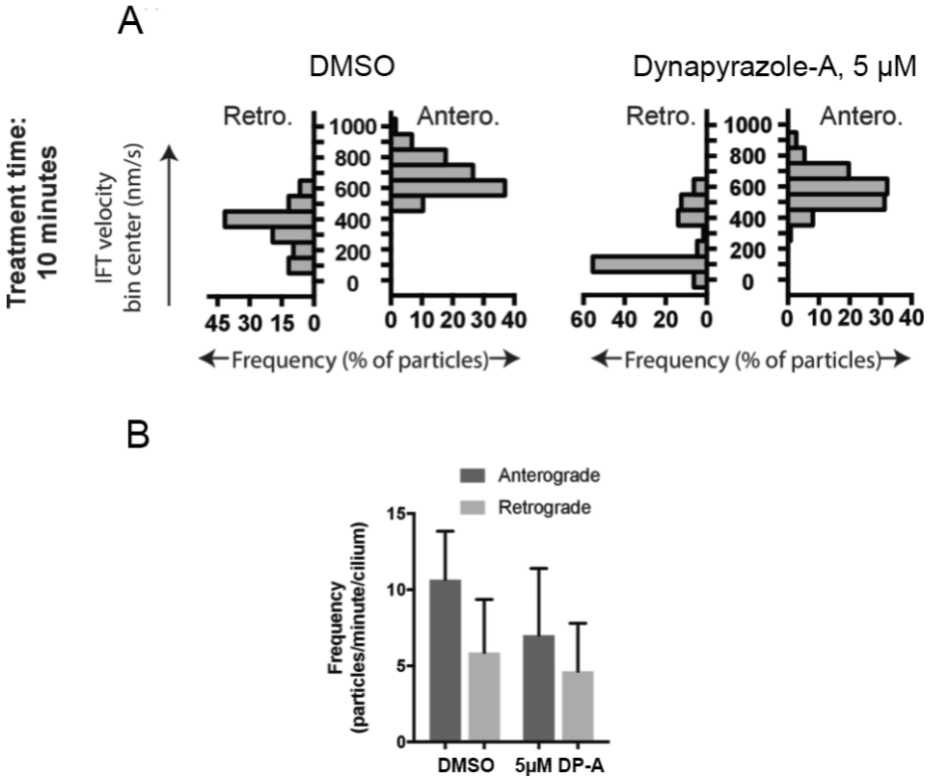

Figure 2.2 Analysis of intraflagellar transport at 10 µM dynapyrazole-A (A) Velocity distribution histograms showing anterograde and retrograde velocities in the vehicle control (0.3% DMSO) and in the presence of dynapyrazole-A (DP-A, 5 µM) (B) at 10 min after treatment. (C) Analysis of intraflagellar transport particle frequencies. Data analysis (Va, anterograde velocity, nm/s; Vr, retrograde velocity, nm/s; Fa, anterograde frequency, counts/minute; Fr, retrograde frequency, counts/minute; values are mean ± S.D. Na, number of anterograde particles analyzed; Nr, number of retrograde particles analyzed; C, number of cilia analyzed). DMSO, Va 655 ± 124, Vr 354 ± 134, Fa 10.2 ± 3, Fr 5.9 ± 3, Na 276; Nr 145, C 18; 5 µM dynapyrazole-A, Va 572 ± 121, Vr 202 ± 180, Fa 6.9 ± 4, Fr 4.2 ± 3, Na 125, Nr 75, C 18.

We next examined whether inhibition of intraflagellar transport by dynapyrazole-A was reversed following washout of the compound. Ciliated cells treated with dynapyrazole-A (5 μM, 5 min) were transferred to solvent-control media with serum (0.3% DMSO, 10% FBS) and incubated for an additional 10 min. Both retrograde and anterograde velocities recovered to control levels (Figure 2.4A, velocities following washout: retrograde: 467 ± 136 nm/s, 173 particles, 18 cilia; anterograde: 697 ± 149 nm/s, 256 particles, 18 cilia) as did transport frequencies (Figure 2.4B). When media with a lower serum concentration was used in washout experiments, retrograde velocities recovered only partially, suggesting that serum may accelerate the partitioning of this compound out of cells (Figure 2.4A). Taken together, our data suggest dynapyrazole-A is likely to be a useful reversible probe to study intraflagellar transport.

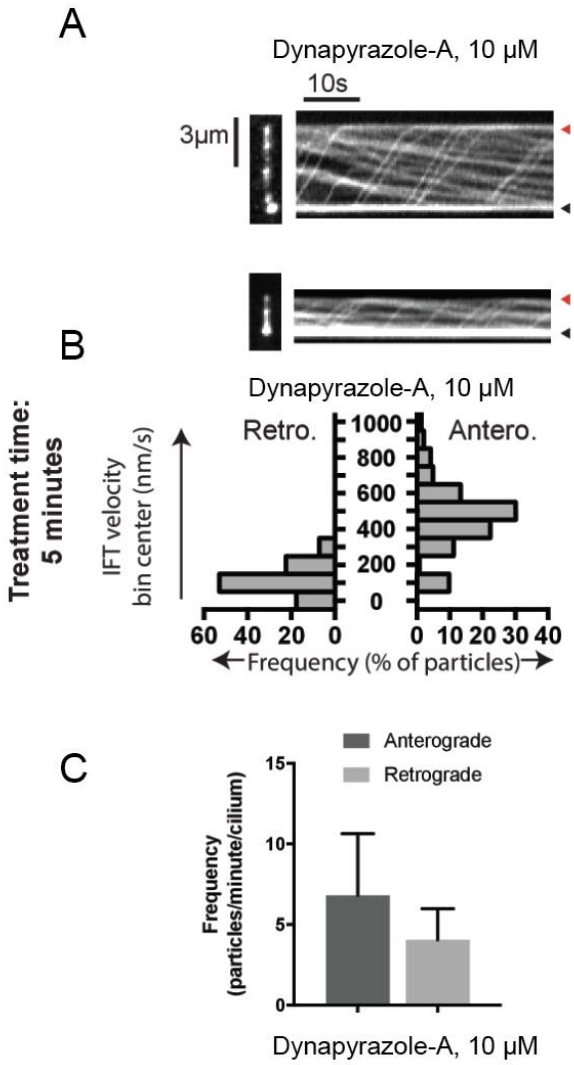

Figure 2.3 Analysis of intraflagellar transport at 10 µM dynapyrazole-A (A) Images from a time-lapse series and associated kymographs of mNeonGreen-IFT88-containing particles in representative primary cilia treated with dynapyrazole-A (10 µM). Still image scale bar, 3 µm; interval between frames, 0.5 s. Kymograph horizontal scale bar, 10 s; vertical scale is identical to cilium image. (B) Velocity distribution histograms for anterograde and retrograde motion. (C) Analysis of particle frequency in the presence of 10 µM dynapyrazole-A. Data analysis (Va, anterograde velocity, nm/s; Vr, retrograde velocity, nm/s; Fa, anterograde frequency, counts/minute; Fr, retrograde frequency, counts/minute; values are mean ± S.D. Na, number of anterograde particles analyzed; Nr, number of retrograde particles analyzed; C, number of cilia analyzed). 10 µM 8, Va 466 ± 183, Vr 121 ± 78, Fa 6.8 ± 4, Fr 4.0 ± 2, Na 143, Nr 85, C 21.

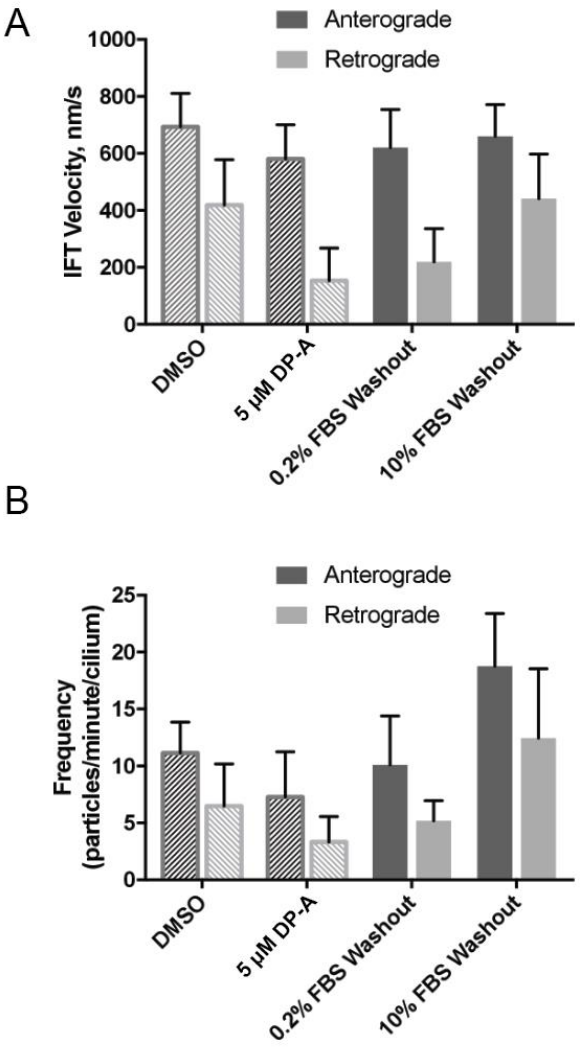

Figure 2.4 The effect of dynapyrazole-A washout on IFT (A) mNeonGreen-IFT88 particle velocities following washout of dynapyrazole-A for 1 hr in media with either low serum (0.2% FBS) or high serum (10% FBS). (B) Particle frequencies following low-serum and high-serum washout. Reference values for solvent control (0.3% DMSO) and inhibited/pre wash-out (5 µM 8) states are shown as checked bars in both (A and B). These values are also shown in Figure 4F and G, respectively, and are included here for reference. Bars represent mean ± S.D. Data analysis (Va, anterograde velocity, nm/s; Vr, retrograde velocity, nm/s; Fa, anterograde frequency, counts/minute; Fr, retrograde frequency, counts/minute; values are mean ± S.D. Na, number of anterograde particles analyzed; Nr, number of retrograde particles analyzed; C, number of cilia analyzed). 0.2% FBS washout, Va 620 ± 134, Vr 219 ± 117, Fa 10.1 ± 4, Fr 5.2 ± 2, Na 111, Nr 57, C 11. 10% FBS washout, Va 660 ± 112, Vr 441 ± 156, Fa 18.8 ± 5, Fr 12.4 ± 6, Na 283, Nr 186, C 16.

2.3 Discussion

The effect of dynapyrazole-A on IFT is similar to the phenotype observed for dynein 2 depletion in *Chlamydomonas reinhardtii.* Previous analyses of a temperature-sensitive mutant in *Chlamydomonas* revealed that dynein 2 depletion causes a ~60–70% reduction in retrograde velocities and a ~20% reduction in anterograde velocities. Notably, the frequency of moving particles was reduced by ~30–60% in both directions (Engel et al., 2012). Based on these results, it was proposed that anterograde and retrograde transport are coupled, such that perturbation of one of the two IFT motor proteins will result in bidirectional inhibition. Thus, dynapyrazole-A allows for the acute and controlled inhibition of intraflagellar transport, which yields a phenotype that is expected for dynein 2 loss-of-function.

Our results suggest dynapyrazole-A can be useful reversible probe to study intraflagellar transport. Relief from dynein inhibition can be best obtained when dynapyrazole-A is removed from cilia using media containing 10% FBS. This is likely due to the hydrophobicity of the compound (calculated logarithm of octanol:water partition coefficient [ClogP]: 4.2). Due to this property, the use of dynapyrazole-A as a cellular probe may require incubating cells with media containing a low percentage of serum (0.2%). Further structure-activity relationship studies on dynapyrazole-A will be needed to identify analogs that maintain dynein inhibition but have lower ClopP values.

2.4 Methods

Murine inner medullary collecting duct (IMCD3) cells stably expressing mNeonGreen-IFT88 were maintained in DMEM/F12 supplemented with 10% FBS.(Ye et al., 2013) 6×10^5 cells were seeded onto 22-mm coverslips in a six well plate and incubated for 24 hours at 37°C. The

media was then replaced with DMEM/F12 + 0.2% FBS and cells were incubated for 24 hours at 37°C to promote cilium formation. Immediately prior to imaging, media was replaced with phenol red-free media (Leibovitz's L-15 + 0.2% FBS) containing either carrier solvent control (0.3% DMSO) or compound. IFT88 transport was observed using a TE2000-E spinning disk confocal microscope (Nikon PlanApo 100x/1.45 objective lens) fitted with a Photometrics Cascade II (EMCCD 512) camera and imaged at a frame rate of 2 frames/s. Kymographs were generated in FIJI using *KymographClear* and the velocities of mNeonGreen-IFT88 foci movement were quantified by *KymographDirect* (Mangeol et al., 2016). The algorithm used to identify IFT88 foci could identify particles with velocities ≥ 25nm/s as moving particles.

For washout experiments, cells were exposed to a 5-min compound treatment as described above. Cells were then washed twice with 5 mL of L-15 supplemented with 10% FBS and 0.3% DMSO. A 5-min incubation followed each wash. Imaging was performed as described above immediately after the second 5-min wash and incubation step had been completed. For washout experiments shown in Figure 2.4, wash steps were performed with either L-15 supplemented with 10% FBS or L-15 supplemented with 0.2% FBS. Following washout of compound, cells were incubated at 37° for 60-min and then imaged.

Chapter 3: Structural Insights into the Chemical Inhibition of Dynein

3.1 Introduction

Dyneins are microtubule-based motor proteins that belong to the AAA (ATPase Associated with various Activities) superfamily, which is defined by a widely conserved AAA domain (Erzberger and Berger, 2006). Dyneins transport diverse cellular cargoes, including organelles, vesicles, chromosomes and mRNAs, toward the minus-end of microtubules. These motor proteins are conserved across eukaryotes and are involved in a wide range of biological functions. In *S. cerevisiae*, only one dynein isoform exists, and is required for the proper positioning of the nucleus during division (Moore et al., 2009). In metazoan cells two isoforms of cytoplasmic dynein are present; dynein 1 is responsible for the majority of microtubule minus-end directed transport in the cytoplasm, and dynein 2 function is restricted to driving intraflagellar transport in cilia and flagella (Roberts, 2018).

Dynein's motor domain, which powers microtubule-based motility, consists of a single polypeptide with six AAA domains that form a ring, an N-terminal linker, and a long mainly coiled-coil stalk that includes the microtubule binding domain (Carter et al., 2011; Kon et al., 2012). Another structural element, named the buttress (or strut), emanates from the AAA5 domain and interacts with and modulates the microtubule binding affinity of the stalk, which extends from the AAA4 domain (Carter et al., 2011; Kon et al., 2012). Similar to other proteins in this superfamily, dynein's six AAA domains are comprised of AAA-L (large) and AAA-S (small) subdomains that together with a AAA-L subdomain of an adjacent AAA domain, form a tripartite interface where ATP binding and hydrolysis can occur (Erzberger and Berger, 2006). The first four AAA domains (AAA1-AAA4) contain the Walker A motifs necessary for ATP binding, while

the AAA5 and AAA6 domains lack this motif and likely have nucleotide-independent structural roles (Schmidt and Carter, 2016). The AAA1 ATPase site is the primary site that drives dynein's motility (Gibbons and Gibbons, 1987; Kon et al., 2004), while the AAA3 active site plays an allosteric role, regulating ATP turnover in the AAA1 domain (Bhabha et al., 2014; DeWitt et al., 2015). The AAA2 domain constitutively binds ATP and lacks the catalytic glutamate in the Walker B motif that is necessary for ATP hydrolysis (Kon et al., 2012; Schmidt et al., 2012). In contrast, the AAA4 domain contains the residues required for ATP binding and hydrolysis, but its function is not well understood. In principle, chemical inhibitors, which can be powerful tools to examine dynein function, could bind at any of these different nucleotide binding sites or another yet uncharacterized site to block dynein's mechanochemical cycle.

At least three different cell-permeable inhibitors of dynein have been reported (Steinman and Kapoor, 2019). Ciliobrevins, cell permeable probes of dynein, were discovered using cell-based screens (Firestone et al., 2012). Dynapyrazoles, designed based on the ciliobrevin scaffold, have improved potency and inhibit the microtubule-stimulated, but not the basal, ATPase activity of human dynein (Steinman et al., 2017). Dynarrestin, which was also discovered using cell-based screens, was able to pull-down dynein complexes from cell extracts but did not block its ATPase activity *in vitro* (Höing et al., 2018). Currently, we lack the structural information required to gain insights into the mechanism of dynein inhibition by any of these compounds. However, for structural studies we require compounds that have the requisite chemical properties and also inhibit dynein's basal ATPase activity, as including micrometer-sized microtubules in these studies can substantially increase technical challenges.

Here we synthesized and tested analogs of dynapyrazoles to identify inhibitors of the basal ATPase activity of dynein. We employed x-ray crystallography, cryo-EM approaches and

computational docking to develop structural models for how these dynapyrazole analogs bind *Saccharomyces cerevisiae* dynein, which has been extensively used for structural studies of this motor protein (Bhabha et al., 2014; Carter et al., 2011; Niekamp et al., 2019; Schmidt et al., 2012). Mutagenesis and single molecule fluorescence analyses were used to test the model of dynein inhibition. Our findings reveal how chemical inhibitors can disrupt the allosteric communication within dynein's AAA ring to block activity.

3.2 Results

To identify inhibitors of dynein's basal ATPase activity we generated compounds that retained the pyrimidine-4-one based core that is common to the ciliobrevins and dynapyrazoles (hereafter, compound **1** and **2**) and therefore would likely maintain dynein inhibition (ring B, Figure 3.1A) (Firestone et al., 2012; See et al., 2016). A facile synthesis of these compounds was afforded by condensation of the 3-cyclopropyl-cholorophenyl substituted aminopyrazole with either 2- or 3-substituted (3-dimethylamino)acrylates in the presence of an acid to yield 5- or 6-substituted pyrazolo-pyrimidinones (Figure 1B).

We generated compounds **3-19** and tested their activity against a previously reported recombinant motor domain construct of human cytoplasmic dynein 1 (hereafter, Hs-dynein 1, aa. 1320-4646, Figure 3.1C and Supplementary Figure 1A) (Steinman et al., 2017). Hs-dynein 1's basal ATP hydrolysis rate was 0.50 ± 0.07 s^{-1} (1 mM MgATP, mean ± standard deviation (SD), n=5, Figure 1E), consistent with previous studies (Steinman et al., 2017). Gratifyingly, we found that compounds (20 μM) with aryl-ether substitutions at the 6-position of the pyrazolopyrimidine core inhibited Hs-dynein 1's ATPase activity in the absence of microtubules (Figure Supplememtary 1A). In particular, a *meta*-chlorophenoxy ether substitution at the 6-position

(compound **19**) led to the strongest inhibition (residual ATPase activity: ~32%, range 29-34%, n=2, 1 mM MgATP, Figures 3.1C, 3.1D and Supplementary Figure 1A). Compounds with a *para*- or *ortho*-chloro groups on the pendent phenyl ring (compounds **17** and **13**, respectively) were less potent, as was an analog (**16**) with a *meta*-methoxy substitution (Figures 3.1C and Supplementary 1A). Dose-dependent analyses indicated that compound **19** inhibits Hs-dynein 1's basal ATPase activity with an IC_{50} of 16 ± 2.3 μM (1 mM MgATP, mean ± SD, n=4, Figure 3.1E).

We further characterized compound **19**'s effect on Hs-dynein 1 by testing if this dynapyrazole derivative also inhibits Hs-dynein 1's microtubule stimulated ATPase activity. In the presence of microtubules (2.5 μM), Hs-dynein 1's ATPase rate was 1.04 ± 0.15 s^{-1} (mean ± SD, n=3), ~2-fold higher than the basal rate, as expected for this construct (Figure 3.1E).(Steinman et al., 2017) Dose-dependent analysis revealed that compound **19** inhibited the microtubule-stimulated ATPase activity of Hs-dynein 1 with an estimated IC_{50} of ~30 μM (1 mM MgATP, n=3, Figure 3.1E). Complete inhibition was not observed, possibly due to limited compound solubility at high doses in this assay. We also examined if compound **19** inhibits the ATPase activity of other AAA proteins that have been previously characterized (Cupido et al., 2019). We measured the steady-state ATPase activities of recombinant Hs-FIGL1, Hs-PCH2, Mm-VCP, Xl-katanin, and Dm-spastin, which we have previously described (Cupido et al., 2019), in the presence of compound **19** (20 μM, 1 mM MgATP). This dynapyrazole derivative did not show appreciable inhibition (<10% reduction) of these AAA proteins other than Hs-FIGL1 (~70% inhibition) (n=2, Supplementary Figure 1B). Taken together, compound **19** inhibits dynein's basal ATPase activity, which compound **1** does not (Steinman et al., 2017), and could therefore be suitable for structural studies and serve as a scaffold for structure-guided design.

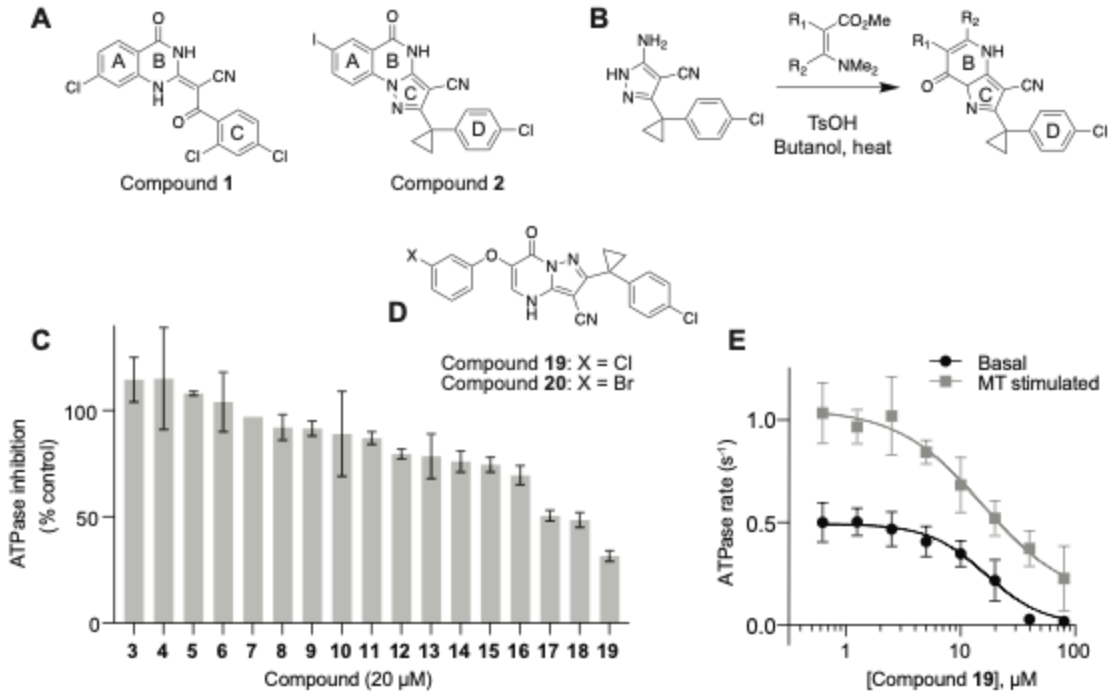

Figure 3.1. Inhibition of human dynein 1's ATPase activity by dynapyrazole derivatives. (A) Chemical structure of the ciliobrevin D (compound **1**) and dynapyrazole-A (compound **2**). A, B, C and D rings are highlighted. (B) Synthesis of bicyclic dynapyrazole derivatives from a common precursor (TsOH: paratoluenelsulfonic acid). (C) Effect of dynapyrazole derivatives on Hs-dynein 1's (N-terminal hexahistixine tag, aa. 1320–4646, uniprot: Q14204) basal ATPase activity. Compounds were tested at 20 μM. Data are mean ± range (n=2, for chemical structures see Figure S1A). (D) Chemical structures of compounds **19** and **20**. (E) ATPase activity of Hs-dynein 1 in the presence of compound **19** with or without the addition of microtubules (2.5 μM). Data are mean ± SD of n ≥ 3 and were fit to a sigmoidal dose-response curve.

One of the highest resolution (3.3 Å) structural models of the dynein motor domain was determined using *S. cerevisiae* dynein.(Schmidt et al., 2012) Therefore, to maximize our chances of gaining structural insights into compound-motor domain interactions, we tested if the pyrazolo-pyrimidinone-based compounds also bound and inhibited *S. cerevisiae* dynein. For these experiments we first generated a previously described construct that contains the motor domain and has been characterized to be an active ATPase (VY137, aa. 1219-4093, hereafter, GFP-Sc-Dyn, Figure 3.2A).(Reck-Peterson et al., 2006) Dose-dependent analyses indicate that compound

19 inhibits GFP-Sc-Dyn's basal ATPase activity with an IC_{50} of 7.8 ± 1.0 μM (1 mM MgATP, mean ± SD, n=3, Figure 3.2B).

S. cerevisiae constructs that contain a Walker B mutation in the AAA1 site (E1848Q) and in which the microtubule binding domain (MTBD) and most of the coiled-coil stalk are replaced with lysozyme (VY972, hereafter, Sc-Dyn-lysoMut) have been shown to be well-suited for structural studies using X-ray crystallography and cryo-EM (Figure 3.2A). (Bhabha et al., 2014) As this construct is inactive, we used a construct with a wild-type, hydrolysis-competent AAA1 domain (E1849) that is otherwise identical to VY972 (VY1027, hereafter, Sc-Dyn-lyso) and determined that compound **19** inhibits Sc-Dyn-lyso's ATPase activity with an IC_{50} of 13 ± 3.1 μM (1 mM MgATP, mean ± SD, n=3, Figures 3.2A and 3.2C).

We also generated compound **20**, with the *meta-chloro* in compound **19** replaced by a *meta*-bromo substitution (Figure 3.1D). We reasoned that bromine's anomalous diffraction may aid in locating the compound in the X-ray diffraction data (Arkhipova et al., 2017). We found that compound **20** inhibits the basal ATPase activity of Sc-Dyn-lyso (IC_{50}: 16 ± 4.9 μM, 1 mM MgATP, mean ± SD, n=3, Figure 3.2C). To examine binding of compound **20** to Sc-Dyn-lysoMut, we used microscale thermophoresis (MST), a technique that uses temperature-induced changes in the mobility of fluorescent molecules as a readout to measure intermolecular interactions.(Jerabek-Willemsen et al., 2014) Compound **20** binds Sc-Dyn-lysoMut with an estimated of K_d of 43 μM (range 36-52 μM, n=2, Figure 3.2D); saturation of the binding curve was not observed likely due to compound solubility limits (Figure 3.2D). Taken together, these data suggest that the Sc-Dyn-lysoMut construct can be employed for our structural studies in the presence of compound **20**.

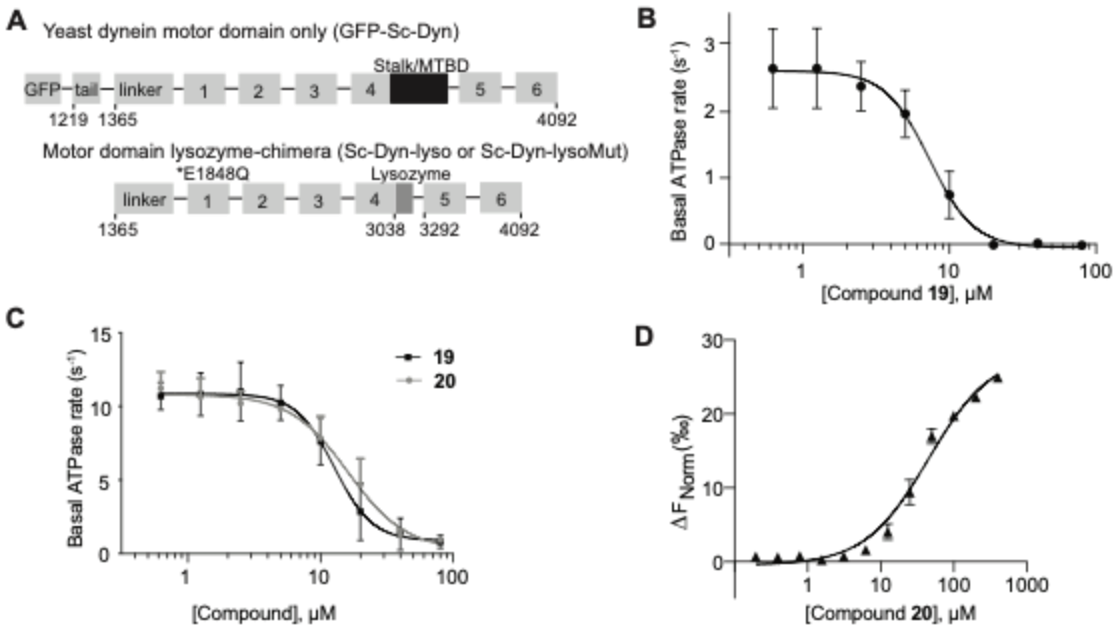

Figure 3.2. Dynapyrazole derivatives inhibit *Saccharomyces cerevisiae* dynein. (A) Schematic showing the domain organization for the *S. cerevisia*e dynein motor domain construct (GFP-Sc-Dyn) and either the WT lysozyme-chimera (Sc-Dyn-lyso) or lysozyme-chimera mutant constructs (Sc-Dyn-lysoMut). The position of the stalk and microtubule-binding domain (MTBD) in GFP-Sc-Dyn is shown (black box). A lysozyme replaces the MTBD and most of the stalk in the Sc-Dyn-lyso and Sc-Dyn-lysoMut constructs (dark gray box). The black asterisk indicates a Walker B mutation (E1848Q) in the AAA1 site of the Sc-Dyn-lysoMut construct. The first and last residues of each construct are indicated. (B) Basal ATPase activity of GFP-Sc-Dyn in the presence of compound **19**. Data are mean ± SD of n=3 and were fit to a sigmoidal dose-response curve. (C) Basal ATPase activity of Sc-Dyn-lyso in the presence of either compound **19** or **20**. Data are mean ± SD of n=3 and were fit to a sigmoidal dose-response curve. (D) Microscale thermophoresis analysis of compound **20**'s interactions with Sc-Dyn-lysoMut. Data are mean ± range of n = 2 and were fit using Equation (2) and converted to ΔF_{norm} using Equation (3) (see methods).

We obtained diffracting crystals of Sc-Dyn-lysoMut in the presence of compound **20** and in the absence of nucleotide. Our screening conditions were based on those previously reported for this construct in the presence of AMPPNP.(Bhabha et al., 2014) We solved the model by molecular replacement to ~4.5 Å resolution (Figures 3.3A, 3.3B and Table 3.1). At this resolution

most of the α helices are well resolved but many of the individual β strands are not (Supplementary Figure 2A). Density for each of the six AAA domains, as well as the linker, truncated stalk and lysozyme is observed (Figure 3.3B).

We first analyzed electron density in the nucleotide-binding pockets that are not accounted for by the protein backbone. In the AAA1 domain, a small positive electron density is observed near the P-loop in the Fo-Fc map (Figure 3.3C). Based on its overall size, this density may correspond to an anion (Figure 3.3C). In the AAA2, AAA3 and AAA4 nucleotide-binding sites, electron densities are present in both the 2Fo-Fc and Fo-Fc maps (Figures 3.3D-3.3F). These densities are larger than what would be expected for an anion or water molecule and may correspond to either nucleotide or compound **20**, but are not well-resolved enough to interpret. We note that the densities are not large enough to accommodate compound **20** or nucleotide. In addition, an anomalous signal was not detected in the diffraction data, possibly due to the flexibility of the bromo-phenyl moiety, low compound affinity, or the current resolution. Overall, hints of additional density was observed in the AAA2, AAA3 and AAA4 nucleotide-binding sites, but establishing their identity was difficult due to the resolution of this model.

We next examined the conformation of the individual AAA domains. The AAA1 domain is in an open conformation, similar to what is observed in the nucleotide-free model of *S. cerevisiae* dynein (pdb 4AKG, hereafter, apo-model) (Supplementary Figures S2B-S2D), consistent with no nucleotide or chemical inhibitor bound. In the apo-model, the AAA3 domain adopts a semi-closed conformation relative to the AAA1 domain, which can close further upon nucleotide binding (Bhabha et al., 2014; Kon et al., 2012; Schmidt et al., 2012; Zhang et al., 2017). The conformation of the AAA3 domain in our X-ray model is similar to that apo-model (Supplementary Figures S2E-G), suggesting that nucleotide is not bound to this site.

We also examined the overall conformation of the AAA ring in the presence of compound **20**. We observed that the linker is extended and docked onto the AAA5-L subdomain (Figure 3.3B), indicating that the motor domain is in a post-powerstroke state (Burgess et al., 2003). Therefore, we aligned the Sc-Dyn-lysoMut X-ray model (hereafter, X-ray model) to other structural models of *S. cerevisiae dynein* with a similarly extended linker conformation such as those that represent the nucleotide-free (apo-model) and AMPPNP-bound states (pdb 4W8F, hereafter AMPPNP-model).(Bhabha et al., 2014; Schmidt et al., 2012) Alignment of the X-ray model with the apo-model on the AAA1-L subdomain revealed that the stalk, buttress and the AAA5-AAA6 domains adopt similar conformations (Figure 3.3G). However, the AAA2/AAA3/AAA4 domains, as a unit, rotate (~8°) towards the linker, when compared to the apo-model. A similar alignment showed that the AAA2/AAA3/AAA4 unit has rotated much less in the X-ray model compared to the AMPPNP-model (Figure 3.3H). The AAA ring is more planar in the X-ray model compared to the apo-model, but less planar than that in the AMPPNP-model (Supplementary Figures S2H, S2I, and S2J). Taken together, the X-ray model reveals a conformational change in one-half of the AAA ring, despite the lack of nucleotide or chemical inhibitor density in the AAA1 site. Interestingly, this conformation has only been observed in structural models of dynein where AMPPNP is bound to the AAA1 site.(Bhabha et al., 2014; Niekamp et al., 2019) However, a higher resolution model of Sc-Dyn-lysoMut in the presence of compound **20** is needed to determine if the inhibitor binds to the AAA3 or AAA4 sites.

Figure 3.3. X-ray model of Sc-Dyn-lysoMut in the presence of compound 20. (A) Schematic of the Sc-Dyn-lysoMut construct. Individual AAA domains are shown (AAA1: blue, AAA2: light blue, AAA3: green, AAA4: yellow, AAA5: orange, AAA6: red). Linker (purple), buttress (orange), stalk (yellow) and lysozyme (gray) are also depicted. Red asterisk indicates that the construct contains a Walker B mutation (E1848Q) in the AAA1 domain. (B) Refined model of Sc-Dyn-lysoMut. Domains are color-coded based on the schematic shown in Figure 3A. (C-F) *2Fo – Fc* (gray mesh, 1.0 σ contour) and *F*o – *F*c (orange mesh, 3.0 σ contour) densities are shown in the AAA1 (C), AAA2 (D), AAA3 (E), and AAA4 (F) domains. (G, H) Visualization of interalpha carbon distances between the X-ray model and either the apo (PDB: 4AKG) (G) or AMPPNP (PDB: 4W8F) model (H)**.** Models were aligned on the AAA1-L subdomain. Linker was removed for clarity. Black arrows indicate direction of domain movement in the X-ray model relative to either of the two nucleotide states, while the size of the arrow indicates the magnitude of movement.

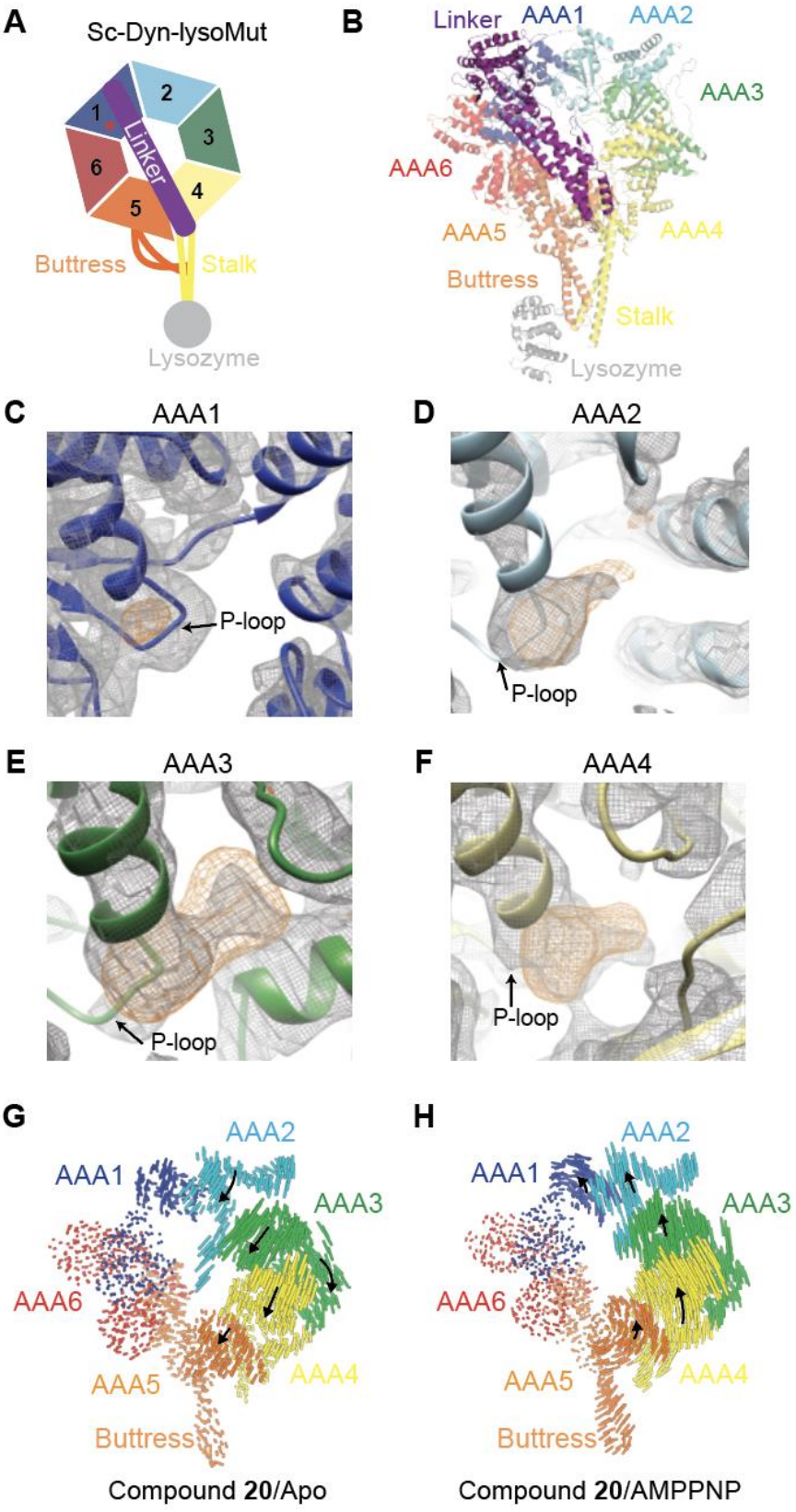
A
Sc-Dyn-lysoMut
1
2
3
4
5
6
Linker
Buttress
Stalk
Lysozyme
B
Linker
AAA1
AAA2
AAA3
AAA6
AAA5
AAA4
Buttress
Stalk
Lysozyme
C
AAA1
P-loop
D
AAA2
P-loop
E
AAA3
P-loop
F
AAA4
P-loop
G
AAA2
AAA1
AAA3
AAA6
AAA5
AAA4
Buttress
Compound 20/Apo
H
AAA2
AAA1
AAA3
AAA6
AAA5
AAA4
Buttress
Compound 20/AMPPNP

Our X-ray model clearly revealed the conformation of the AAA ring in the presence of compound **20**, but the resolution did not allow us to clearly identify the binding site(s) of the chemical inhibitor. Therefore, we next turned to single-particle cryo-EM studies employing the same mutant construct (Sc-Dyn-lysoMut) we used for X-ray crystallography.(Bhabha et al., 2014) We hypothesized that a large cryo-EM dataset may lead to a higher resolution model for the motor protein, as we would have the opportunity to classify out compositional and conformational heterogeneity, which may be limiting the resolution of our X-ray structure. We prepared samples of Sc-Dyn-lysoMut in the presence of compound **20** (80 μM) and without any nucleotide present, and collected a large dataset on a Titan Krios microscope equipped with K2 camera (4892 movies, Supplementary Figures 3, 4A, and 4B). Due to the challenges presented by sample heterogeneity and particle damage during the freezing process, we used extensive data processing and classification strategies, which included data from two other datasets in the initial processing steps (described in detail in methods and Figure S3). After 3D classification and refinement we obtained a reconstruction with an average resolution of ~3.9 Å with 136,180 particles (Map 1, Supplementary Figures 3B and 4C). We found that the overall conformation of dynein's AAA ring in this reconstruction was similar to that observed in our X-ray model (Figure 3.4A), as indicated by the root-mean square displacement (RMSD) of 1.512 Å (2354 c-alpha positions).

Based on the differences in local resolution (Figure 3.4B), it was clear that heterogeneity within the AAA ring was still limiting the resolution of the EM map. Therefore we used masking, signal subtraction, and 3D classification to process densities corresponding to the AAA2-AAA4, AAA5-AAA6 and AAA6-AAA2 domains separately, resulting in three independent reconstructions (see methods, Supplementary Figure 3B). This process revealed heterogeneity in the AAA1 domain, such that density for the AAA1-S subdomain is either present (Map 2, ~4.5 Å)

or weak/missing (Map 3, ~7.9 Å). When density for the AAA1 domain is clearly defined, we can conclude that AAA1 is in an open state, as expected when it is nucleotide-free. After further masking and signal subtraction, we obtained higher resolution maps of the AAA2/AAA3/AAA4 (Map 4, ~3.5 Å) and AAA5/AAA6 domains (Map 5, ~3.7 Å) (Supplementary Figures 3B, 4D and Table 3.2). Consistent with the reported resolution for these domains, densities for many side chains are observed (Supplementary Figure 4E).

The cryo-EM map revealed no additional density in the AAA1 nucleotide-binding pocket (Figure 3.4C), which is consistent with the observation that the AAA1 domain adopts an open conformation. However, the AAA2, AAA3 and AAA4 nucleotide-binding pockets all clearly show the presence of additional density that is not accounted for by the protein (Figures 3.4D-3.4F). AAA2 lacks catalytic activity and is therefore expected to be constitutively bound to ATP (Schmidt et al., 2012). Indeed, the map reveals a ligand density in the AAA2 nucleotide-binding site that is consistent with the size and shape of ATP (Supplementary Figure 5A).

We next examined the cryo-EM map that corresponds to the AAA3 and AAA4 binding sites, which revealed additional densities that are consistent with the size and shape of compound **20** (Figures 3.4G and 3.4I). Three lines of evidence suggest that this density corresponds to compound **20**. First, the AAA3 domain is in a semi-closed conformation, similar to the X-ray- and apo-models, and it is therefore unlikely that nucleotide is bound at the AAA3 site (Supplementary Figure 5D). Second, the protein was purified in the absence of nucleotide, which is unlikely to yield a protein containing ATP or ADP in the AAA1, AAA3 and AAA4 sites.(Schmidt et al., 2012) Third, if nucleotide were present, we would expect it to be bound at AAA1, especially since the E1849Q mutation renders this domain hydrolysis deficient. Therefore, we conclude that the densities in the AAA3 and AAA4 sites correspond to compound **20**, which was present in 50-fold

molar excess in our sample relative to the protein concentration. Taken together, our cryo-EM data provide a structural model where compound **20** occupies the AAA3 and AAA4 nucleotide-binding sites.

Figure 3.4 (A) X-ray model (gray) aligned to the cryo-EM model of Sc-Dyn-lysoMut (purple). Lysozyme is omitted from the X-ray model for calculation of RMSD between the two models. (B) EM map (Map 1) of Sc-Dyn-lysoMut colored by local resolution, as estimated by RELION 3.0. (C-E) EM density corresponding to the nucleotide-binding sites of either the AAA1 (Map 2) (C), AAA2 (Map 4) (D), AAA3 (Map 4) (E), or AAA4 (Map 4) (F) domains. Densities (Map 4) corresponding to the Sc-Dyn-lysoMut model (AAA2L: cyan, AAA3L: green, AAA4L: yellow, AAA5L: orange) are shown in gray, whereas densities (Map 4) for the ligand are shown as blue meshes. For each AAA domain, the location of the large and small subdomains are indicated. (G) Two views of pose 1-AAA3 overlayed with the EM density (Map 4, blue mesh). Compound **20** is shown as a stick model (carbon: orange, oxygen: red, nitrogen: blue, chlorine: green, bromine: dark red). (H) View of compound **20** in the nucleotide-binding site of the AAA3 domain. The predicted inhibitor-protein interactions (black dashed line) are shown (N-loop: green, P-loop: yellow, sensor II: blue) (I) Two views of pose 1-AAA4 overlayed with the EM density (Map 4, blue mesh). Compound **20** is shown as a stick model (carbon: orange, oxygen: red, nitrogen: blue, chlorine: green, bromine: dark red). (J) View of compound **20** in the nucleotide-binding site of the AAA4 domain. The predicted inhibitor-protein interactions (black dashed line) are shown (N-loop: green, P-loop: yellow, sensor II: blue, arginine finger: gray). (K) Steady-state ATPase activity of GFP-Sc-Dyn and its mutants in the presence of 2 mM MgATP. Data are mean ± S.D. for GFP-Sc-Dyn (n=4) and the AAA3/AAA4 mutant (n=3). Data are mean ± range for the AAA3 mutant (n=2).

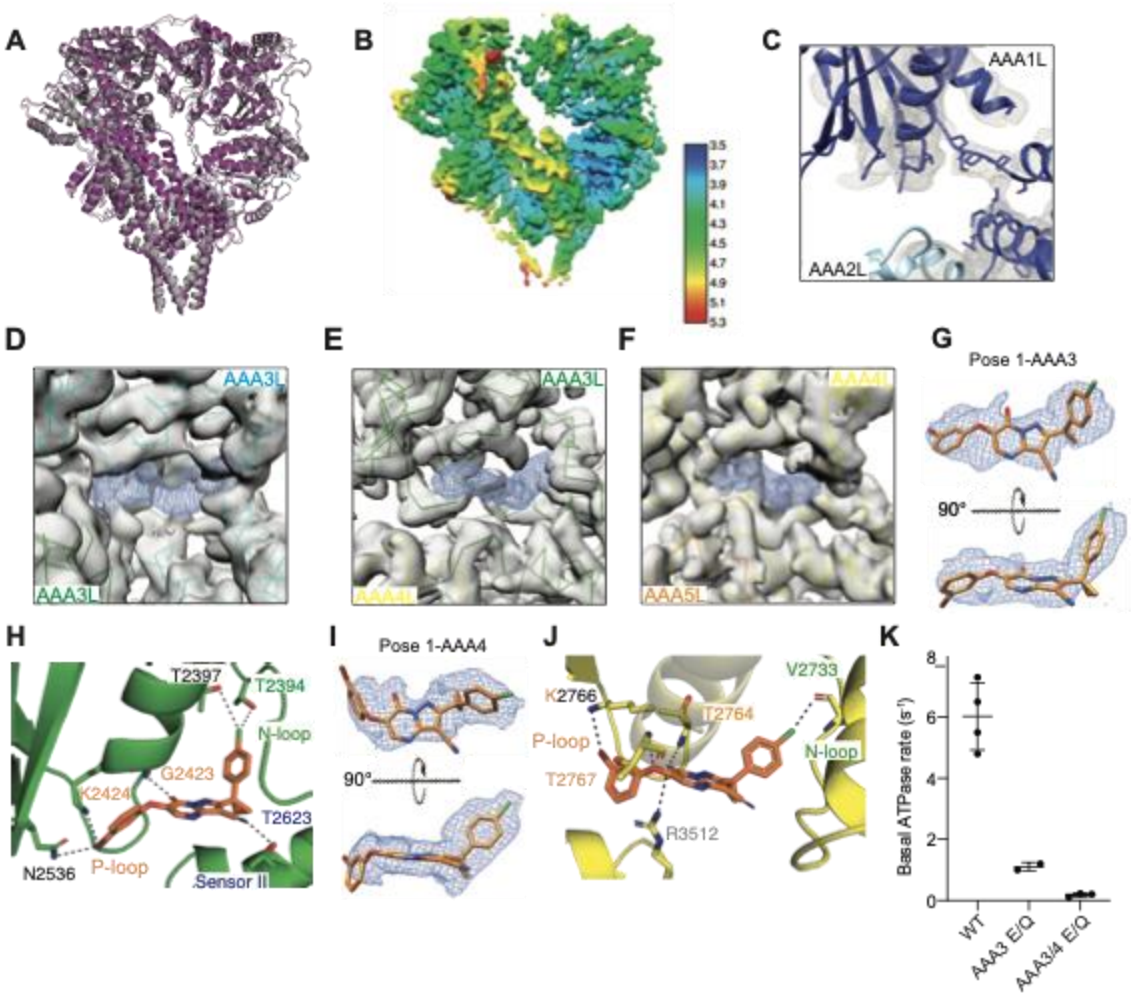
A
B
C
AAA1L
AAA2L
3.5
3.7
3.9
4.1
4.3
4.5
4.7
4.9
5.1
5.3
D
AAA3L
AAA3L
E
AAA3L
AAA4L
F
AAA4L
AAA5L
G
Pose 1-AAA3
90°
H
T2397
T2394
N-loop
G2423
K2424
T2623
N2536
P-loop
Sensor II
I
Pose 1-AAA4
90°
J
K2766
T2764
V2733
P-loop
T2767
N-loop
R3512
K
Basal ATPase rate (s⁻¹)
8
6
4
2
0
WT
AAA3 E/Q
AAA3/4 E/Q

The local resolution of our cryo-EM reconstruction at the inhibitor binding sites is not high enough to unambiguously identify the inhibitor binding pose. Therefore, to identify the key inhibitor-target interactions, we performed computational docking of compound **20** into the AAA3 and AAA4 sites and ATP into the AAA2 site using the GlideEM script in the Schrodinger software (Schrodinger LLC) (see methods) (Robertson et al., 2019). This script utilizes the GLIDE docking scoring function and the real space cross-correlation score to the EM map to generate binding poses of a ligand that are energetically favored and that can be accommodated by the density(Robertson et al., 2019). The enolate form of compound **20** was used for computational docking, which was calculated to be the major tautomer at pH 7.0 (see methods). This analysis generated five candidate poses of compound **20** for the AAA3 site, and four poses for the AAA4 site (Figures 3.4G, 3.4I and Supplementary Figures 5B, S5C).(Robertson et al., 2019) For the AAA2 site, the GlideEM script revealed a pose of ATP that is similar to that previously reported (Schmidt et al., 2012). For the AAA3 and AAA4 sites, we selected the orientation of the ligand that best fits into the EM density, as indicated by the docking model-EM map correlation coefficient (Afonine et al., 2018). The poses that best fit into the EM densities in the AAA3 and AAA4 sites (hereafter, pose 1-AAA3 and pose 1-AAA4) had a value of 0.73 and 0.74, respectively, indicating a good fit (Figures 3.4G, 3.4I and Supplementary Figures 5B and 5C)(Afonine et al., 2018). Visual inspection of the map also clearly identified this as an appropriate binding pose.

For pose 1-AAA3, the 3-cyclopropyl-chlorophenyl moiety of compound **20** is buried in the adenine-binding pocket and is within van der waals distance to hydrophobic residues in the N-terminal loop motif (N-loop) (Figures 3.4H and Supplementary Figure 5E). The backbone of the phosphate-binding loop (P-loop) residue G2423, which interacts with the β-phosphate of AMPPNP in the AMPPNP-model (chain B), forms a hydrogen-bonding interaction with the

carbonyl oxygen of the enolatepyrimidinone moiety (Figures 3.4H and Supplementary Figure 5E) (Bhabha et al., 2014). The N-loop residue, T2394, and a residue that neighbors the N-loop motif, T2397, form a halogen-bonding interaction with the chloro-phenyl moiety. The threonine in the sensor II motif (T2623) hydrogen bonds with the cyano moiety, while the catalytic lysine (K2424) and residue N2536 form halogen bonds with the bromo-phenyl group. These proposed interactions may explain how compound **20** can displace nucleotide to bind to the AAA3 ATP-binding site.

In pose 1-AAA4, compound **20** binds to the nucleotide-binding pocket in the AAA4 domain in a similar orientation shown for the AAA3 site (Figure 3.4J and Supplementary Figure 5F). The 3-cyclopropyl phenyl moiety fits into the adenine-binding pocket of the AAA4 site and is stabilized by hydrophobic interactions with N-loop residues V2730, P2731, and V2733. The chloro-phenyl moiety forms a halogen-bonding interaction with the backbone of N-loop residue V2733. Additionally, the arginine finger (R3512) and the backbone of P-loop residue, T2764, hydrogen bond with the carbonyl oxygen of the enolatepyrimidinone moiety. The backbone of P-loop residue T2767 forms a hydrogen-bonding interaction with the phenoxy moiety of compound **20**. Taken together, these analyses suggest that compound **20** adopts a similar orientation in both the AAA3 and AAA4 sites and forms a network of interactions with the P- and N-loops motifs in dynein.

The cryo-EM model suggests that the dynapyrazole derivatives bind to the AAA3 and AAA4 domains. However, loss of ATP binding or hydrolysis in either of these sites individually is not sufficient to abolish dynein's ATPase activity.(Cho et al., 2008; Kon et al., 2004) As the dynapyrazole derivatives inhibit dynein's ATPase activity, we predicted that mutating the AAA3 and AAA4 sites simultaneously may yield an inactive ATPase. We generated two mutants of GFP-Sc-Dyn that are deficient in ATP hydrolysis in either the AAA3 domain (E2488Q) or in both the

AAA3 and AAA4 domains (E2488Q/E2819Q) and characterized their steady-state ATP-hydrolysis activity at a concentration of MgATP (2 mM) that is close to physiological conditions. GFP-Sc-Dyn had a basal ATPase activity of ~6.0 s^{-1}, which is consistent with published values (n=4, Figure 3.4K) (Cho et al., 2008). The catalytic activity of the AAA3 mutant (E2488) was reduced by ~6 fold relative to that of GFP-Sc-Dyn (~1.1 s^{-1}, n=2, Figure 3.4K), which is similar to the ~10 fold reduction that was previously observed for a dynein motor domain construct containing this mutation (Cho et al., 2008). In contrast, a mutant containing a Walker B mutation in both the AAA3 and AAA4 sites sites resulted in an inactive enzyme (~0.18 s^{-1}, n=3, Figure 3.4K). This result is consistent with our structural data and suggests that the AAA3 and AAA4 domains may act synergistically to regulate dynein's ATPase activity.

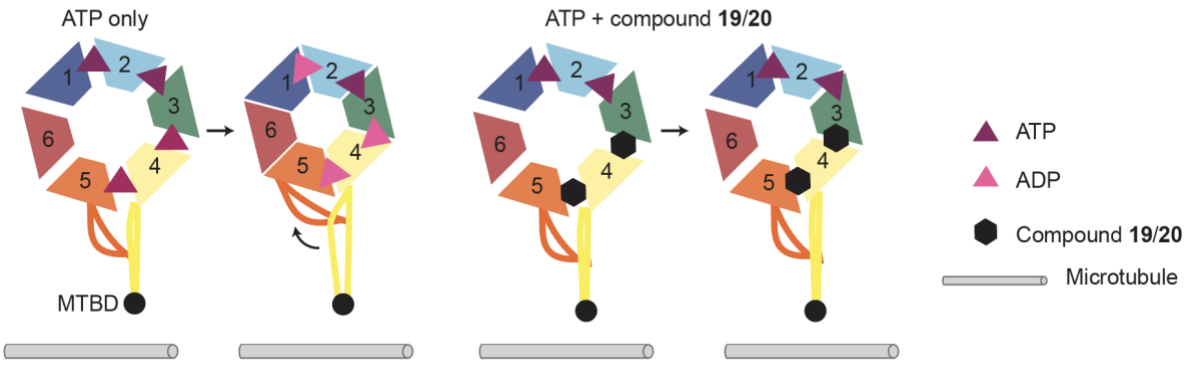

Figure 3.5 Model for the inhibition of *S. cerevisiae* dynein by the dynapyrazole derivatives. Schematic of the *S. cerevisiae* dynein motor domain. Individual domains are shown and color-coded based on the schematic shown in Figure 3A. The microtubule binding domain (MTBD) at the tip of the stalk is shown (black circle). Upon ATP binding and hydrolysis in the AAA1, AAA3, and AAA4 domains, the two halves of the AAA ring rotate towards each other, resulting in closure of the AAA ring, and the buttress slides relative to the stalk, changing the stalk registry. In the presence of ATP (purple triangle) and the dynapyrazole analog (black hexagon), the nucleotide binds to the AAA1 site, but cannot be hydrolyzed. One-half (AAA2-AAA4) of AAA ring rotates but is not sufficient to induce conformational changes in the other half of the ring. The buttress does not slide relative to the stalk, resulting in weak microtubule binding affinity.

3.3 Discussion

While inhibitors of dynein have been described before, their binding sites have been difficult to identify. This is largely due to the inherent flexibility of the dynein motor domain, which makes it a challenging target for structural biology and limits achievable resolution. Here we describe derivatives of dynapyrazoles that inhibit the ATPase activity of human dynein 1 and *S. cerevisiae* dynein, and report X-ray and cryo-EM models of the dynein motor domain in the presence of compound **20**. The resolution of our cryo-EM model is comparable to that of prior X-ray models of the *S. cerevisiae* dynein motor domain (3.3-3.8 Å) (Bhabha et al., 2014; Schmidt et al., 2012), and is substantially higher than those reported for other cryo-EM models of the dynein motor domain (~7-20 Å) (Bhabha et al., 2014; Niekamp et al., 2019; Toropova et al., 2014). This model reveals the inhibitor binding sites, as density for compound **20** is observed in the AAA3 and AAA4 domains. Together, our findings suggest that compound **20** inhibits dynein by disrupting allosteric communication across the AAA ring, and not by binding to AAA1, which is the main site of ATP hydrolysis in dynein.

The dynapyrazole derivative binds to the AAA3 and AAA4 sites, resulting in a conformational change in the AAA ring relative to both the apo- and AMPPNP-model. Current models suggest that ATP binding to the AAA1 site initiates a rigid body movement of the AAA2/AAA3/AAA4 unit towards the linker domain (Bhabha et al., 2014; Schmidt et al., 2015). These conformational changes are propagated to the other half of the ring (AAA5/AAA6), which in turn pulls the buttress motif relative to the stalk domain to alter microtubule binding affinity (Figure 3.6) (Bhabha et al., 2014; Niekamp et al., 2019; Schmidt et al., 2015). In our model, compound **20** binding to the AAA3 and AAA4 sites results in a rotation of the AAA2/AAA3/AAA4 block towards the linker domain to produce a more planar AAA ring, a

conformation that is intermediate between the apo and AMPPNP-bound states. Similar conformational changes were observed in a model of a dynein stalk mutant solved in the presence of AMPPNP (Niekamp et al., 2019). This stalk mutation has been proposed to decouple the two halves of the AAA ring, resulting in weak microtubule binding affinity. We propose that compound binding to the AAA3 and AAA4 sites similarly prevents the propagation of conformational changes between the two halves of the AAA ring (Figure 3.5).

How does compound binding to the AAA3 and AAA4 sites result in inhibition of dynein's basal ATPase activity? Based on previous data showing that AAA1 is the main catalytic site (Gibbons and Gibbons, 1987; Kon et al., 2004) and our data showing that the dynapyrazole derivatives inhibit dynein's basal ATPase activity (Figures 3.1E, 3.2B and 3.2C), we expected that these compounds may bind and inhibit AAA1. However, unexpectedly, our structure shows that the nucleotide-binding pocket of AAA1 is empty, while compound **20** is bound at the AAA3 and AAA4 sites. Additionally, our cryo-EM data shows that the AAA1 domain is in an open conformation (Map 1), suggesting that the AAA1 catalytic site does not have high affinity for compound **20** (Supplementary Figure 3B). Previous work has shown that a Walker B mutation in the AAA3 domain reduces dynein's overall ATPase activity by ~10-fold (Cho et al., 2008). To understand how these two sites may function together to regulate ATPase activity, we measured the basal ATPase activity of a AAA3/AAA4 double Walker B mutant, which should be incapable of hydrolyzing ATP at these sites. We observed a ~40-fold reduction in Sc-Dynein's basal ATPase rate compared to the WT protein (Figure 4K). These data indicate that blocking ATP hydrolysis at the AAA3 site, and to a greater extent AAA3 and AAA4 together, affects the ATPase activity of the AAA1 site, which is likely the activity being read out in ATPase assays. We note that blocking nucleotide hydrolysis in the AAA3 and AAA4 domains of *D. discoideum* dynein led to only a ~4-

fold reduction in the protein's basal catalytic activity relative to that of the WT protein, suggesting that *D. discoideum* and *S. cerevisiae* may have different allostery mechanisms (Kon et al., 2012). In the presence of the dynapyrazole derivatives, the AAA3 and AAA4 sites are similarly blocked, which may explain how compound binding to the AAA3 and AAA4 domains results in inhibition of dynein's ATPase activity and suggests a model where the dynapyrazole derivatives indirectly inhibit ATP hydrolysis at the AAA1 site.

Computational docking suggests key interactions with ATP-binding residues in the AAA3 and AAA4 sites that likely contribute to dynein inhibition by these compounds. The dynapyrazole derivatives adopt an ATP-like conformation, where the cyclopropyl-phenyl moiety buries itself within the adenine-binding site, and the halo-phenoxy enolatepyrimidinone moieties interact with the P-loop motif. Notably, the proposed inhibitor-target interactions are different from those observed for other active-site binding chemical inhibitors of AAA proteins, such as spastazoline and CB-5083, which contact residues in the N-loop and sensor II motifs (Pisa et al., 2019a; Tang et al., 2019). Further studies will examine if modifying the scaffold to allow for hydrogen-bonding interactions with the N-loop motif can lead to an improvement in potency.

Our model reveals the binding sites for a dynein inhibitor, suggests an allosteric mechanism of inhibition, and lays the groundwork for the design of isoform-selective inhibitors of dynein. Sequence comparisons indicate that the residues in the AAA3 and AAA4 sites in dynein 1 and 2 are not well conserved. In fact, the residues that are within 4 Å of the bound nucleotide in the AAA3 and AAA4 sites are 53% and 35% identical, respectively, between dynein 1 and 2, which enables the design of inhibitors that interact with residues that are specific to one isoform (Supplementary Figure 6). This approach would be less feasible if the inhibitor bound to the AAA1 site, as the residues within 4 Å of the bound nucleotide in AAA1 are identical between human

dynein 1 and 2 (Supplementary Figure 6). In principle, compounds that bind to the regulatory sites, AAA3 and AAA4, can be modified to achieve selective isoform-selective inhibition.

3.4 Methods

Protein purification:

The human cytoplasmic dynein 1 construct (Hs-Dynein 1, uniprot: Q14204) containing an N-terminal hexahistixine (6x-His) was expressed using the baculovirus/insect cell expression system and purified as previously described (Steinman et al., 2017). *Xenopus laevis* katanin (Xl-katanin), *Mus musculus* VCP (Mm-VCP), *Homo sapiens* PCH2 (Hs-PCH2), *Homo sapiens* FIGL1 (Hs-FIGL1), and *Drosophila melanogaster* spastin (Dm-spastin) were expressed and purified as previously described (Cupido et al., 2019).

All *S. cerevisiae* dynein constructs were purified as previously described with some modifications (Reck-Peterson et al., 2006). Eight liters of *S. cerevisiae* cells were grown until stationary phase and harvested by centrifugation. Cells were washed with water, and resuspended in 5X lysis buffer (150 mM HEPES, pH 7.4, 250 mM K-Ac, 10 mM $Mg(Ac)_2$, 2 mM EGTA). Cells were slowly pipetted into liquid nitrogen and then lysed using a coffee grinder. The resulting powder was resuspended in 2.5X lysis buffer (75 mM HEPES, pH 7.4, 125 mM K-Ac, 5 mM $Mg(Ac)_2$, 0.5 mM EGTA, 3 mM DTT, 0.2 mM ATP, 1 mM PMSF) and clarified by ultracentrifugation (37,000 rpm for 2 hours). The supernatant was poured into a column containing IgG beads (Sepharose 6 Fast Flow, GE Healthcare) and allowed to bind to the beads by gravity-flow. The beads were washed with wash buffer (30 mM HEPES, pH 7.4, 50 mM K-Ac, 2 mM Mg-Ac, 1 mM EGTA, 10% glycerol, 200 mM KCl, 2 mM DTT, 100 μM ATP, 0.4 mM PMSF, 0.25% Triton-X). Beads were subsequently washed with TEV buffer (50 mM Tris-HCl, pH 7.4,

150 mM K-Ac, 2 mM $Mg(Ac)_2$, 1 mM EGTA, 10% glycerol, 0.5 M TCEP, 0.1 M PMSF) and resuspended in TEV buffer (3 mL) containing TEV protease (25 μg) for overnight on-column TEV cleavage at 4°C. Protein was eluted and concentrated using an Amicon Ultra (100 kDa). The protein was subjected to size-exclusion chromatography (Superdex 200I, GE Healthcare) and eluted in size-exclusion buffer (20 mM Tris, pH 8.0, 50 mM K-Ac, 2 mM $Mg(Ac)_2$, 1 mM EGTA, 10% glycerol, 1 mM TCEP).

Co-crystallization of Sc-Dyn-lysoMut with compound 20

Sc-Dyn-lysoMut was concentrated to ~8 mg/mL and compound **20** was added (final compound concentration 100 μM, 2% DMSO) in size-exclusion buffer. A seed stock was prepared by using Seed Bead (Hampton Research, HR2-320) to crush crystals of Sc-Dyn-lysoMut that were generated using a previous condition (Bhabha et al., 2014). Seeds were added to the protein-compound complex (1:4 dilution) and mixed with an equal amount of reservoir solution (100 mM Bis-Tris pH 6.8-7.2, 200 mM sodium acetate, 8-13.5% PEG 3350, and 10 mM TCEP) using the sitting drop method. Crystals were allowed to form at 18°C. Prior to cooling in liquid nitrogen, the crystals were supplemented with ethylene glycol to give a final precipitant (PEG 3350, ethylene glycol) concentration of 35%.

Data Collection and Refinement

Diffraction data were collected at the NSLS-II 17-ID-2 (FMX) beamline at Brookhaven National Laboratory and indexed to P21212 and reduced using XDS (Table 3.1) (Kabsch, 2010). The X-ray data was phased by molecular replacement using Phaser (McCoy et al., 2007). A nucleotide-free model of the *S. cerevisiae* dynein motor domain (PDB: 4AI6) was used as the search model to

yield a solution. The model was adjusted in Coot (Emsley et al., 2010) and refined using Phenix (McCoy et al., 2007). The lysozyme, which is not present in the search model, was built by rigid body docking of the lysozyme coordinates from PDB: 4W8F into the defined electron density.

Cryo-EM sample preparation and data collection

For cryo-EM of *S. cerevisiae* (Sc-Dyn-lysoMut) in the presence of compound **20**, freshly purified protein was diluted to either 0.15 or 0.5 mg/mL and mixed with 2X compound **20** stock solution (final concentration: 80 μM compound **20**, 0.2% DMSO). Samples were applied to glow discharged Quantifoil 1.2/1.3 copper grids and plunge frozen in liquid ethane using Vitrobot IV (Thermo Fisher Scientific). Dose-fractionated (50 frames, 10s exposure, 44 e^- per $Å^2$) super-resolution image stacks were collected on a 300-kV Titan Krios electron microscope (Thermo Fisher Scientific) equipped with a K2-summit detector (Gatan) using automated data collection (SerialEM). Datasets were collected over three separate sessions, where the first two were collected at 1.3 Å per pixel and the last collected at 1.0 Å per pixel.

Data processing and analysis

Two datasets were originally acquired on two different grids that only differed by their protein concentration (0.15 vs 0.5 mg/ml). For these first two datasets, per pixel drift correction and dose-weighting was performed using MotionCor2. The motion-corrected, dose-weighted images were imported into CryoSPARC and contrast transfer function (CTF) parameters were estimated using CTFFind4. For dataset 1, approximately 1,000 particles were manually picked and subjected to 2D classification. Classes that represented different orientations of the protein were used as templates for automatic particle picking. Multiple rounds of 2D classification were performed to

discard classes that displayed ice or carbon contamination, or poorly resolved averages. Particles from the classes with the best alignment parameters were selected and used to build an *ab initio* model as a reference for 3D refinement. A similar process was followed for dataset 2, but for the final refinement, the 124,891 particles selected were combined with the 25,016 particles from the dataset 1, reaching a resolution of ~4.4 Å. The results obtained from those datasets were subsequently used at three stages for the processing of dataset 3. The 2D classes were used to auto-pick, the best particles were then used as seeds to drive 2D classification, and the 3D map was used as a reference for 3D refinement.

Dataset 3 was collected in super-resolution at a higher pixel size (0.518 Å/pixel) and processed using RELION 3.0. First, correction of inter-frame movement for each pixel and dose-weighting was performed using RELION 3.0's implementation of MotionCor2. Motion-corrected images were first binned to 1.3 Å per pixel and the CTF parameters were estimated as previously described (Rohou and Grigorieff, 2015). 2D class averages from the first two datasets were used as templates for automatic particle picking in RELION 3.0. To expedite 2D classification, the 4,723,853 particles picked were split into 24 sub-sets. Addition of the best 149,907 particles from datasets 1 and 2 to each subset facilitated the separation of good particles from junk during the 2D classification of dataset 3. Each subset was then subjected to seven rounds of 2D classification. Particles selected from dataset 3 were re-extracted at a pixel size of 0.518 A/pixel. While the 3D model obtained from dataset 2 was used as a reference, only particles from dataset 3 were used for refinement. After a round of 3D classification with eight classes, the two best classes were merged and refined to 3.9 Å.

Local resolution estimation revealed that the AAA3 and AAA4 domains contained the highest resolution information, while the map showed lack of density for the AAA1 domain. To increase local resolution, we performed a wide range of signal subtractions to refine individual or adjacent AAA domains. Among those, three locally refined maps of 2 or 3 adjacent AAA domains lead to improved resolution: AAA6-AAA1 (Map 2), AAA2-AAA4 (Map 4), and AAA5-AAA6 (Map 5). The model was constructed using coordinates from the X-ray model presented here. Rigid body fit of each individual AAA small and large domain was performed using PHENIX, as part of the real-space refinement procedure (ADP refinement, local grid search, secondary structure restraints, Ramachandran restraints). Coot, Chimera, and Pymol were used to visualize and analyze the maps and models.

Computational docking and refinement

Ligand docking was performed using the GlideEM script in the Schrödinger software (Robertson et al., 2019). The individual AAA2, AAA3, and AAA4 domains were extracted from the model and subjected to computational docking separately. The major tautomer at pH 7.0 of compound **20** was assigned performed using the LigPrep panel in Maestro. Default parameters were used for GlideEM docking, except for the following modifications: RECEP_CCUT=0.24, RECEP_VSCALE=0.9, EPIK_PENALTIES=False, HBOND_DONOR_AROMH=True, HBOND_ACCEP_HALO=True. Real space refinement was performed in PHENIX using default settings except that the OPLS3e /VSGB2.1 force field was used with a weight factor of 1.

Radioactive ATPase assay

ATPase assays using Hs-dynein 1 were performed as previously described, except that the protein concentration was reduced to 30 nM and the reaction time was extended to 45 min (Steinman et al., 2017). If microtubules were present, the buffer (25 mM PIPES pH7.0, 30 mM KCl, 1 mM

EGTA, 5 mM MgCl2, 0.01% Triton™ X-100, 1 mM DTT) contained 20 μM taxol. For structure-activity relationship studies with the dynapyrazole derivatives, percent inhibition of the ATPase activity was calculated by normalizing the ATPase rate in the presence of compounds to DMSO control. To determine the IC_{50} of compounds **19** and **20,** the measured activity was plotted against concentration of compound 19 and the data were fit using the sigmoidal dose response curve (Equation (1)) in Prism v. 8.0 (GraphPad Software Inc).

$$Y = Y_{min} + \frac{(Y_{max} - Y_{min})}{1 + 10^{(logIC50 - x)h}} \quad (1)$$

NADH-coupled steady state ATPase assay for K_{cat} analyses

To determine the catalytic activity of GFP-Sc-Dyn and its mutants, an enzymatic ATP regeneration system was used. For GFP-Sc-Dyn and its mutants, the assay buffer contains 30 mM HEPES pH 7.4, 50 mM K-Acetate, 2 mM magnesium acetate, 1 mM EGTA, 0.01% Triton X-100, and 1 mM DTT. A 20 μL reaction was prepared in a flat bottom 384 well black polystyrene plate (Greiner Bio One, Wemmel, Belgium, catalog # 781090) and contained protein (Sc-Dyn-lyso: 5 nM, GFP-Sc-Dyn: 50 nM) and 1X NADH mix. 1X NADH mix contains 200 μM NADH (Sigma, N7410), 1 mM phosphoenol pyruvic acid monopotassium salt (Sigma, P7127), 33.3 U/mL D-lactic dehydrogenase (Sigma, L3888), and 55 U/mL pyruvate kinase (lyophilized powder, Sigma, P9136). The reaction was initiated with the addition of 10X MgATP (2 μL), and the fluorescence signal was monitored using a Synergy NEO Microplate Reader (λex = 340 nm, 440 nm emission filter). The slope of the fluorescence values versus time was calculated to give the rate of fluorescence decrease. The ATPase rate was calculated from the rate of fluorescence decrease from a standard curve measuring the contribution of ADP to the NADH fluorescence signal.

NADH-coupled steady state ATPase assay for analysis of compound 19 and 20

A 20 µL reaction was prepared in a flat bottom 384 well black polystyrene plate (Greiner Bio One, Wemmel, Belgium, catalog # 781090) and contained Sc-Dyn-lyso, 1X NADH mix, and compound. 1X NADH mix contains 200 µM NADH (Sigma, N7410), 1 mM phosphoenol pyruvic acid monopotassium salt (Sigma, P7127), 33.3 U/mL D-lactic dehydrogenase (Sigma, L3888), and 55 U/mL pyruvate kinase (lyophilized powder, Sigma, P9136). For Sc-Dyn-lyso, a ten dose serial dilution was performed in DMSO starting at 4 mM compound **19** or **20**. For Hs-FIGL, Dm-spastin, Mm-VCP/p97, Xl-katanin, and Hs-PCH2, compound **19** (1 mM in DMSO) was diluted 1:25 in buffer to achieve 2X compound. For typical conditions, 2X compound (10 µL) was added to protein/NADH mix (8 µL) and incubated for 10 min at RT. The reaction was initiated with the addition of 10 mM MgATP (2 µL), and the fluorescence signal was monitored using a Synergy NEO Microplate Reader (λex = 340 nm, 440 nm emission filter). The slope of the fluorescence values versus time was calculated to give the rate of fluorescence decrease. The ATPase rate was calculated from the rate of fluorescence decrease from a standard curve measuring the contribution of ADP to the NADH fluorescence signal.

Assay buffers:

Sc-Dyn-lyso (5 nM): 30 mM HEPES pH 7.4, 50 mM KOAc, 1 mM EGTA, 2 mM MgOAc, 1 mM DTT, 10% glycerol, 0.01% Triton™ X-100

Xl-katanin (50 nM): 25 mM K-HEPES pH 7.5, 70 mM KCl, 20 mM $(NH4)_2SO_4$, 5 mM $MgCl_2$, 2.5 mM DTT, 0.01% w/v Triton™ X-100

Mm-p97 (400 nM): 30 mM HEPES pH 7.4, 50 mM KOAc, 1 mM EGTA, 2 mM MgOAc, 1 mM DTT, 0.01% w/v Triton™ X-100

Hs-FIGL (50 nM): 25 mM Na-MES pH 6.5, 70 mM KOAc, 20 mM $(NH4)_2SO_4$, 5 mM $Mg(OAc)_2$, 1 mM TCEP, 0.01% w/v Triton™ X-100

Dm-spastin (75 nM): 25 mM K-HEPES pH 7.5, 225 mM KCl, 2.5 mM $(NH4)_2SO_4$, 5 mM $MgCl_2$, 2.5 mM DTT, 1 mg/mL BSA, 0.005% w/v Triton™ X-100

Hs-PCH2 (250 nM): 25 mM Tris-HCl pH 8.5, 150 mM KCl, 20 mM $(NH4)_2SO_4$, 5 mM $MgCl_2$, 2.5 mM DTT, 1 mg/mL BSA, 0.025% (v/v) Triton™ X-100

Microscale thermophoresis assay (MST)

The binding affinities of compound **20** to Sc-Dyn-lysoMut was measured using Monolith NT.115 (NanoTemper Technologies, Munich, Germany). Sc-Dyn-lysoMut was labeled with the Monolith NT Protein Labeling Kit RED-NHS. To obtain a fluorescence intensity between 200 and 1100 counts at 20% LED power, a final concentration of 30-50 nM protein was used. The MST assays were performed in the following buffer: 20 mM Tris-HCl pH 8.0, 50 mM K-Ac, 2 mM $Mg(Ac)_2$, 1 mM EGTA, and 10% glycerol. A 50X compound stock was prepared by a 1:2 serial dilution of the compound in DMSO starting from 20 mM (12 doses total). The 50X compound stock was diluted in buffer to obtain a 2X compound stock. The 2X protein stock was mixed well with 2X compound and incubated for 10 min at RT in the dark. Each sample was transferred to a Monolith

premium capillary tube, and measurements were performed at 40% MST power. A binding curve was observed at 1.5s after the start of thermophoresis. The K_D was determined by fitting the F_{norm} values to Equation (2) using Prism v. 8.0 (GraphPad Software Inc) at different concentrations of compound 20. F_{norm} values were converted to ΔF_{norm} using Equation (3).

$$Y = Y_{min} \quad + ((Y_{max} - Y_{min} \quad) (1 - \frac{(B - K_D - X + \sqrt{(B+A+K_D)^2 - 4[AB]}}{2P}) \tag{2}$$

$$\Delta F_{norm} = \frac{F_{hot}}{F_{cold}} - F_{unbound} \tag{3}$$

In Equation (2), *A* is the compound concentration, *B* denotes the protein concentration, *AB* is the concentration of bound complex and K_D denotes the equilibrium dissociation constant. In Equation (3) F_{hot} denotes the fluoresence value at the hot state and F_{hot} represents the fluoresence value at the cold state. $F_{unbound}$ indicates the mean fluoresence at the unbound state.

Chemical Synthesis

General. Solvents and reagents were purchased from VWR or Sigma Aldrich. All reactions involving air- or moisture-sensitive compounds were performed under nitrogen atmosphere using dried glassware. ^{1}H and ^{13}C NMR spectra were recorded at 500MHz and 125Mz respectively, on a Bruker Advance III HD 500 MHz NMR spectrometer equipped with at TCI cryogenic probe with enhanced ^{1}H and ^{13}C detection. All data was collected at 298K, signals were reported in ppm, internally referenced for ^{1}H and ^{13}C to chloroform signal at 7.26 ppm or 77.0 ppm; to DMSO signal at 2.50 ppm or 39.5 ppm, or TMS at 0 ppm. Chemical shifts are reported in parts per million (ppm) and the coupling constants (*J*) are expressed in hertz (Hz). Splitting patterns are designated as

follows: s, singlet; d, doublet; t, triplet; m, multiplet; dd, doublet of doublets; ddd, double of doublets of doublets; dt, doublet of triplets. Flash chromatography purifications were performed on Combi*Flash* Rf (Teledyne ISCO) as the stationary phase. Melting points were determined on a MP50 Melting Point System (Mettler Toledo). Purity for all tested compounds was determined through high-performance liquid chromatography and all compounds were found to be > 95% pure.

General method A (used to prepare compounds **6, 8, 9, 10, 13, 17, 18, 19, 20**)

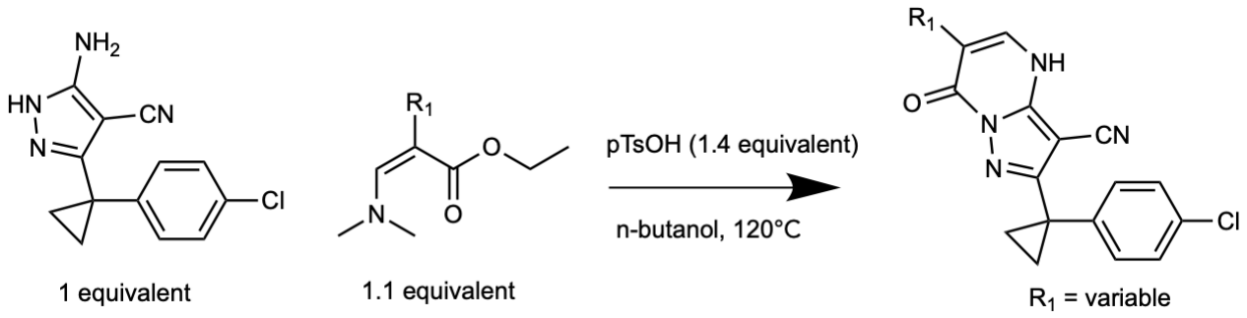

A mixture of the appropriate ethyl or methyl (Z)-2-(alkyloxy)-3-(dimethylamino)prop-2-enoate (1.1 equivalents), 5-amino-3-[1-(4-chlorophenyl)cyclopropyl]-1H-pyrazole-4-carbonitrile (**1**, 1 equivalent), and *p*-toluenesulfonic acid hydrate (1.4 equivalents) in 1-butanol was stirred at 120 °C for 16 h. The reaction mixture was concentrated in vacuo. The residue was purified column chromatography (silica gel, hexane/ethyl acetate) and washed with ethyl acetate to give the desired product.

General method B (used to prepare compound **16**)

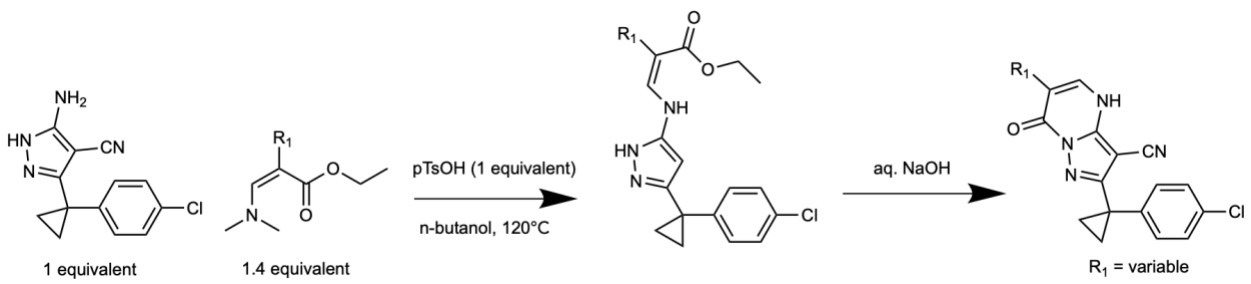

To a solution of ethyl (E)-3-(dimethylamino)-2-(aryloxy)prop-2-enoate (1.4 equivalents) in butanol were added **1** (1 equivalent), *p*-toluenesulfonic acid hydrate (1 equivalent). The mixture was stirred at 120 °C for 3 days. The mixture was cooled to room temperature and concentrated *in vacuo*. The residue was purified by column chromatography (0% - 60% hexane in ethyl acetate) to give the corresponding ethyl (E)-3-[[3-[1-(4-chlorophenyl)cyclopropyl]-4-cyano-1H-pyrazol-5-yl]amino]-2-(aryloxy)prop-2-enoate, which was subsequently dissolved in ethanol and treated with aqueous sodium hydroxide (1.8 equivalents NaOH) at room temperature. The mixture was concentrated after being stirred at room temperature for 6 h. The mixture was neutralized with 1N HCl and extracted with ethyl acetate. The combined organic layer was washed with water and brine, dried over $MgSO_4$, filtered and concentrated *in vacuo*. The residue was purified by column chromatography (silica-gel, 50% - 100% hexane in ethyl acetate) to give the desired product.

General method C (used to prepare compound **4**)

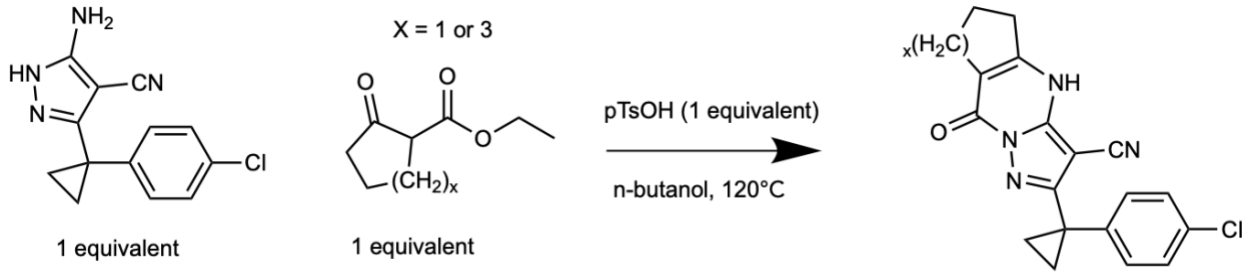

A mixture of the appropriate ethyl 2-oxocycloalkane carboxylate (1 equivalent), **1** (1 equivalent)

and *p*-toluenesulfonic acid hydrate (1 equivalent) in n-butanol was stirred at 120 °C for 1.5 h. The reaction was concentrated *in vacuo*. The residue was purified by column chromatography (silica-gel, 50-100% ethyl acetate in hexane) to give the desired product.

General method D (used to prepare compound **5, 7, 11, 14, 15**)

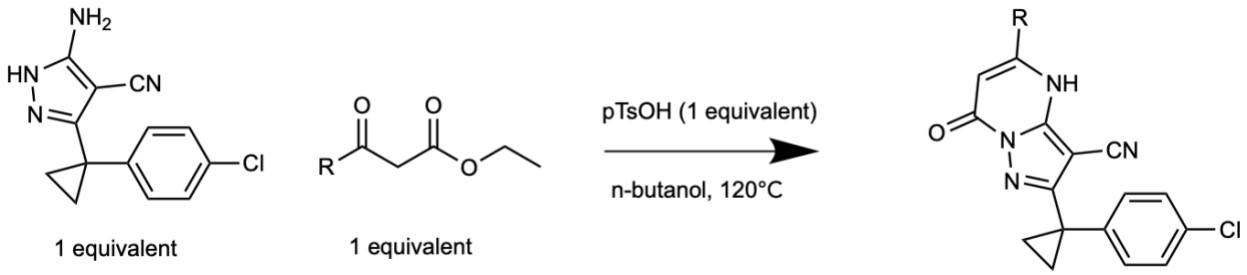

A mixture of **1** (1 equivalent), the appropriate 3-substituted ethyl-3-oxopropanoate (1 equivalent) and *p*-toluenesulfonic acid hydrate (1 equivalent) in n-butanol was stirred at 120°C for 2 h. The reaction was cooled to room temperature. Resulting precipitates were collected and washed with methanol to give the desired product.

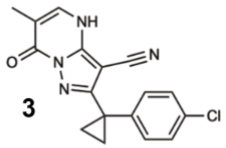

3

To a solution of methyl (E)-3-(dimethylamino)-2-methyl-prop-2-enoate (180 mg, 1.26 mmol) in n-butanol were added p-toluenesulfonic acid hydrate (359 mg, 1.89 mmol) and 3-amino-5-[1-(4-chlorophenyl)cyclopropyl]-1H-pyrazole-4-carbonitrile (326 mg, 1.26 mmol). The mixture was stirred at 120 °C for 16 h. The mixture was poured into water and extracted with EtOAc. The organic layer was washed with water, then washed with brine, dried over magnesium sulfate, and concentrated in vacuo. The residue was purified by column chromatography (silica-gel, 10%-60%

ethyl acetate in hexane) to give crude product (140 mg). The crude material (29 mg) was purified with preparative HPLC (water/CH3CN, 0.1% formic acid) to give 2-[1-(4-chlorophenyl)cyclopropyl]-6-methyl-7-oxo-4H-pyrazolo[1,5-a]pyrimidine-3-carbonitrile (**3**, 16 mg, 49 µmol, 3.91% yield) as a colorless solid. 1H NMR (500 MHz, DMSO-d6) δ 13.22 (s, 0H), 7.71 (s, 1H), 7.47 – 7.14 (m, 4H), 1.94 (s, 3H), 1.46 (s, 2H), 1.30 (s, 2H). MS m/z 325.0 [M+1]+.

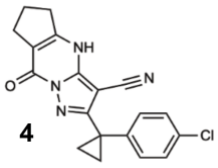

4

A mixture of ethyl 2-oxocyclopentanecarboxylate (30.2 mg, 193 µmol, 27.9 µL), 3-amino-5-[1-(4-chlorophenyl)cyclopropyl]-1H-pyrazole-4-carbonitrile (50.0 mg, 193 µmol) and TsOH.H2O (36.8 mg, 193 µmol) in n-BuOH (1.50 mL) was stirred at 120 °C for 1.5 h. The reaction was concentrated in vacuo. The residue was purified by column chromatography (silica-gel, 50-100% EtOAc in hexane) to give 2-(1-(4-chlorophenyl)cyclopropyl)-8-oxo-5,6,7,8-tetrahydro-4H-cyclopenta[d]pyrazolo[1,5-a]pyrimidine-3-carbonitrile (**4**, 44.7 mg, 127 µmol, 66% yield) as an off white solid. 1H NMR (500 MHz, DMSO-d6) δ 13.50 (s, 1H), 7.36 (d, J = 7.9 Hz, 2H), 7.28 (d, J = 7.8 Hz, 2H), 2.91 (t, J = 7.6 Hz, 2H), 2.69 (t, J = 7.2 Hz, 2H), 2.13 – 2.03 (m, 2H), 1.50 (s, 2H), 1.37 (s, 2H). MS m/z: 351.2 [M+1]+.

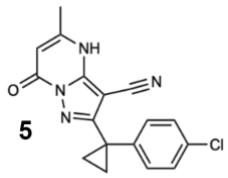

5

The mixture of ethyl 3-oxobutanoate (50.0 mg, 384 µmol) , 3-amino-5-[1-(4-chlorophenyl)cyclopropyl]-1H-pyrazole-4-carbonitrile (99.4 mg, 384 µmol) and TsOH.H2O (73.1

mg, 384 µmol) in BuOH (3.0 mL) was stirred at 120 °C for 2 h. The reaction mixture was cooled to room temperature. The precipitate was collected and washed with MeOH to give 2-[1-(4-chlorophenyl)cyclopropyl]-5-methyl-7-oxo-4H-pyrazolo[1,5-a]pyrimidine-3-carbonitrile (**5**, 62.4 mg, 192 µmol, 50% yield) as an off-white solid. ^{1}H NMR (500 MHz, DMSO-*d*6) δ 13.17 (s, 1H), 7.38 – 7.34 (m, 2H), 7.31 – 7.26 (m, 2H), 5.83 (s, 1H), 2.29 (s, 3H), 1.50 (s, 2H), 1.37 (s, 2H). MS m/z: 325.1 [M+1]+.

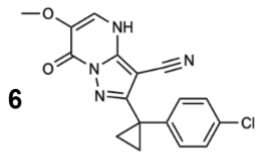

6

General method A was used to obtain 2-[1-(4-chlorophenyl)cyclopropyl]-6-methoxy-7-oxo-4H-pyrazolo[1,5-a]pyrimidine-3-carbonitrile (**6**, 66% yield). 1H NMR (500 MHz, DMSO-d6) δ 13.18 (s, 1H), 7.77 (s, 1H), 7.38 (d, J= 8.5 Hz, 2H), 7.31 (d, J= 8.3 Hz, 2H), 3.77 (s, 3H), 1.53 (q, J= 4.5 Hz, 2H), 1.39 (q, J= 4.5 Hz, 2H). MS m/z: 341.1 [M+1]+.

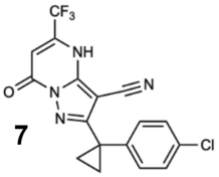

7

General method D was used to obtain 2-(1-(4-chlorophenyl)cyclopropyl)-7-oxo-5-(trifluoromethyl)-4,7-dihydropyrazolo[1,5-a]pyrimidine-3-carbonitrile (**7**, 7.7% yield)1H NMR (500 MHz, DMSO-d6) δ 7.34 (d, J = 7.9 Hz, 2H), 7.26 (d, J = 7.6 Hz, 2H), 5.92 (s, 1H), 1.49 (s, 2H), 1.32 (s, 2H). 1H was hidden. MS; m/z 379.1 (M+1).

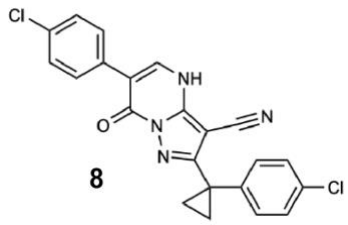

8

To a solution of methyl (Z)-2-(4-chlorophenyl)-3-(dimethylamino)prop-2-enoate (111 mg, 464 µmol) in butanol (5.00 mL) were added 1 (100 mg, 387 µmol), p-toluenesulfonic acid hydrate (74 mg, 387 µmol). The mixture was stirred at 120 °C for 3 hour. The mixture was cooled to room temperature. The resulting solid was collected by filtration using methanol to give 6-(4-chlorophenyl)-2-[1-(4-chlorophenyl)cyclopropyl]-7-oxo-4H-pyrazolo[1,5-a]pyrimidine-3-carbonitrile (**8**, 74 mg, 176 µmol, 45% yield) as a white solid. 1H NMR (500 MHz, DMSO-d6) δ 13.88 (s, 1H), 8.19 (s, 1H), 7.76 – 7.68 (m, 2H), 7.56 – 7.48 (m, 2H), 7.44 – 7.37 (m, 2H), 7.36 – 7.30 (m, 2H), 1.60 – 1.52 (m, 2H), 1.46 – 1.39 (m, 2H). MS m/z: 419 [M-H]-.

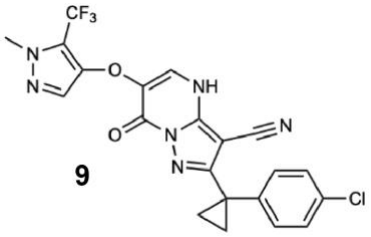

9

General method A was used to obtain 2-[1-(4-chlorophenyl)cyclopropyl]-6-[1-methyl-5-(trifluoromethyl)pyrazol-3-yl]oxy-7-oxo-4H-pyrazolo[1,5-a]pyrimidine-3-carbonitrile (**9**, 43% yield). 1H NMR (500 MHz, DMSO-d6) δ 8.00 (s, 1H), 7.44 – 7.36 (m, 2H), 7.35 – 7.27 (m, 2H), 6.34 (s, 1H), 3.80 (s, 3H), 1.55 – 1.47 (m, 2H), 1.38 – 1.30 (m, 2H). MS m/z: 475.2 [M+1]+.

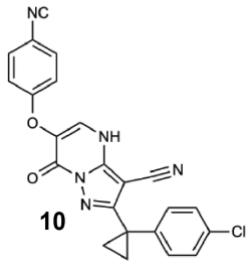

10

General method A was used to obtain 2-[1-(4-chlorophenyl)cyclopropyl]-6-(4-cyanophenoxy)-7-oxo-4H-pyrazolo[1,5-a]pyrimidine-3-carbonitrile (**10**, 9.9% yield). 1H NMR (500 MHz, DMSO-d6) δ 7.95 (s, 1H), 7.76 (d, J = 8.9 Hz, 2H), 7.41 – 7.35 (m, 2H), 7.34 – 7.27 (m, 2H), 7.06 (d, J = 8.9 Hz, 2H), 1.54 – 1.48 (m, 2H), 1.35 – 1.30 (m, 2H). MS m/z: 428.2 [M+1]+.

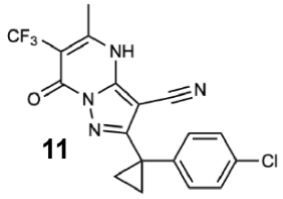

11

A mixture of **1** (100 mg, 387 µmol), ethyl 3-oxo-2-(trifluoromethyl)butanoate (77 mg, 387 µmol), and p-toluenesulfonic acid hydrate (74 mg, 387 µmol) in butanol (5.00 mL) was stirred at 100 °C for 8 h. The reaction was concentrated *in vacuo*. The residue was purified by column chromatography (silica-gel, 20-80% ethyl acetate in hexane) and washed with diisopropyl ether to give 2-[1-(4-chlorophenyl)cyclopropyl]-5-methyl-7-oxo-6-(trifluoromethyl)-4H-pyrazolo[1,5-a]pyrimidine-3-carbonitrile (**11**, 56.0 mg, 143 µmol, 37% yield) as a pale yellow solid. 1H NMR (500 MHz, Chloroform-*d*) δ 10.99 (s, 1H), 7.32 (d, *J* = 8.4 Hz, 2H), 7.28 – 7.23 (m, 2H), 2.53 – 2.48 (m, 3H), 1.71 – 1.66 (m, 2H), 1.36 (q, *J* = 4.5 Hz, 2H). MS m/z 393.318 $[M+1]_+$.

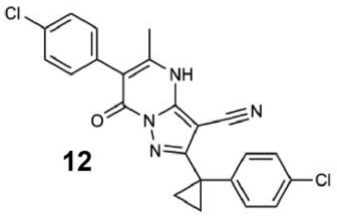

12

A mixture of 2-[1-(4-chlorophenyl)cyclopropyl]-6-iodo-5-methyl-7-oxo-4H-pyrazolo[1,5-a]pyrimidine-3-carbonitrile (11, 10 mg, 22 μmol), cyclopentyl(diphenyl)phosphane;dichloromethane;dichloropalladium;iron (1.83 mg, 2.22 μmol), potassium carbonate (6.1 mg, 44.4 μmol), and (4-chlorophenyl)boronic acid (4.2 mg, 26.7 μmol) in EtOH (0.5 mL) and toluene (0.5 mL) was stirred at 80 °C for 5.5 h. The reaction was concentrated in vacuo. The residue was purified by column chromatography (silica-gel, 0-100% ethyl acetate in hexane) to give 6-(4-chlorophenyl)-2-[1-(4-chlorophenyl)cyclopropyl]-5-methyl-7-oxo-4H-pyrazolo[1,5-a]pyrimidine-3-carbonitrile (**12**, 3.6 mg, 8.3 μmol, 37% yield) as a yellow solid. 1H NMR (500 MHz, DMSO-d6) δ 13.30 (s, 1H), 7.50 (d, J = 8.0 Hz, 2H), 7.37 (d, J = 8.5 Hz, 2H), 7.34 – 7.26 (m, 4H), 2.16 (s, 3H), 1.39 (s, 2H), 1.23 (s, 2H). MS m/z 435.3 [M+1]+.

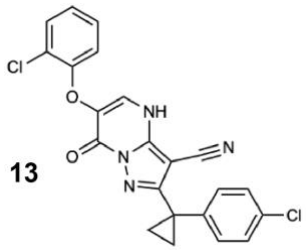

13

General method A was used to obtain 6-(2-chlorophenoxy)-2-[1-(4-chlorophenyl)cyclopropyl]-7-oxo-4H-pyrazolo[1,5-a]pyrimidine-3-carbonitrile (**13**, 20% yield). 1H NMR (500 MHz, Chloroform-d) δ 8.09 (s, 1H), 7.48 (d, J = 7.9 Hz, 1H), 7.36 (d, J = 8.6 Hz, 2H), 7.30 (d, J = 8.6 Hz, 2H), 7.22 – 7.15 (m, 1H), 7.01 (t, J = 8.3 Hz, 1H), 6.94 – 6.86 (m, 1H), 1.53 – 1.47 (m, 2H),

1.35 (t, J = 5.6 Hz, 2H). MS m/z: 437.2 [M+1]+.

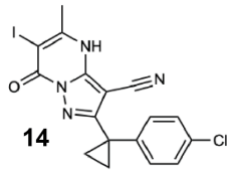

14

A mixture of ethyl 3-oxobutanoate (50.0 mg, 384 µmol, 48.6 µL), 3-amino-5-[1-(4-chlorophenyl)cyclopropyl]-1H-pyrazole-4-carbonitrile (99.4 mg, 384 µmol) and TsOH.H2O (73.1 mg, 384 µmol) in n-BuOH (3.0 mL) was stirred at 120 °C for 2 h. The reaction was cooled to rt. The precipitate was collected and washed with MeOH to give 2-[1-(4-chlorophenyl)cyclopropyl]-5-methyl-7-oxo-4H-pyrazolo[1,5-a]pyrimidine-3-carbonitrile (**14**, 62.4 mg, 192 µmol, 50% yield) as an off white solid. 1H NMR (500 MHz, DMSO-d6) δ 13.17 (s, 1H), 7.38 – 7.34 (m, 2H), 7.31 – 7.26 (m, 2H), 5.83 (s, 1H), 2.29 (s, 3H), 1.50 (s, 2H), 1.37 (s, 2H). MS m/z 325.1 [M+1]+.

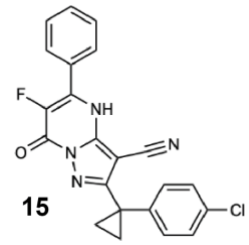

15

A mixture of 1 (54.5 mg, 211 µmol), ethyl (E)-3-(dimethylamino)-2-fluoro-3-phenyl-prop-2-enoate (50.0 mg, 211 µmol) and p-toluenesulfonic acid hydrate (43.9 mg, 255 µmol) in n-butanol (2.0 mL) was stirred at 130 °C for 2 h. The reaction mixture was concentrated in vacuo. The residue was purified by column chromatography (silica-gel, 50-80%, ethyl acetate in hexane). The resulting solid was triturated with ethyl acetate to give 2-[1-(4-chlorophenyl)cyclopropyl]-6-fluoro-7-oxo-5-phenyl-4H-pyrazolo[1,5-a]pyrimidine-3-carbonitrile (**15**, 29 mg, 72.1 µmol, 34%

yield) as a colorless solid. 1H NMR (500 MHz, DMSO-d6) δ 7.82 – 7.65 (m, 2H), 7.66 – 7.46 (m, 3H), 7.37 (d, J= 8.1 Hz, 2H), 7.30 (d, J= 8.2 Hz, 2H), 1.62 – 1.46 (m, 2H), 1.45 – 1.28 (m, 2H). MS m/z 405.1 [M+1]+.

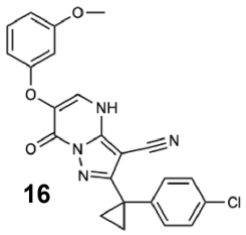

16

General method B was used to obtain 2-[1-(4-chlorophenyl)cyclopropyl]-6-(3-methoxyphenoxy)-7-oxo-4H-pyrazolo[1,5-a]pyrimidine-3-carbonitrile (**16**, 80% yield). 1H NMR (500 MHz, DMSO-d6) δ 13.68 (s, 1H), 8.21 (s, 1H), 7.38 (d, J = 8.5 Hz, 2H), 7.32 (d, J = 8.5 Hz, 2H), 7.21 – 7.16 (m, 1H), 6.65 – 6.57 (m, 3H), 3.73 (s, 3H), 1.56 – 1.49 (m, 2H), 1.43 – 1.33 (m, 2H). MS m/z: 433.1 $[M+1]^+$.

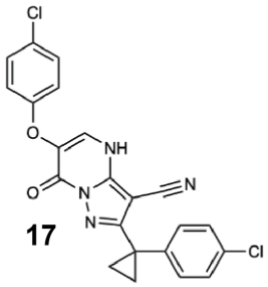

17

General method A was used to obtain 6-(4-chlorophenoxy)-2-(1-(4-chlorophenyl)cyclopropyl)-7-oxo-4,7-dihydropyrazolo[1,5-*a*]pyrimidine-3-carbonitrile (**17,** 14.08% yield). 1H NMR (500 MHz, DMSO-d6) δ 13.69 (s, 1H), 8.09 (s, 1H), 7.48 – 7.24 (m, 6H), 7.00 (d, J = 6.9 Hz, 2H), 1.50 (s, 2H), 1.35 (s, 2H). MS m/z: 437.1 [M+1]+.

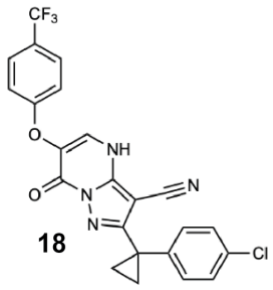

18

General method A was used to obtain 2-[1-(4-chlorophenyl)cyclopropyl]-7-oxo-6-[4-(trifluoromethyl)phenoxy]-4H-pyrazolo[1,5-a]pyrimidine-3-carbonitrile (**18**, 17% yield) as a pale yellow solid. 1H NMR (500 MHz, DMSO-d6) δ 8.15 (s, 1H), 7.66 (d, J = 8.4 Hz, 2H), 7.49 – 7.04 (m, 6H), 1.64 – 1.28 (m, 4H). MS m/z: 469 [M-H]-.

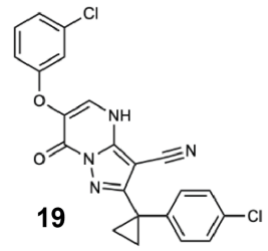

19

General method A was used to obtain6-(3-chlorophenoxy)-2-[1-(4-chlorophenyl)cyclopropyl]-7-oxo-4H-pyrazolo[1,5-a]pyrimidine-3-carbonitrile (**19**, 10% yield) as a beige solid. 1H NMR (500 MHz, DMSO-*d*6) δ 8.26 (s, 1H), 7.38 (d, *J*= 8.6 Hz, 2H), 7.36 – 7.29 (m, 3H), 7.18 (d, *J*= 2.3 Hz, 1H), 7.10 (dd, *J*= 8.0, 1.9 Hz, 1H), 7.06 (dd, *J*= 8.4, 2.5 Hz, 1H), 1.57 – 1.46 (m, 2H), 1.45 – 1.34 (m, 2H). MS m/z: 439 $[M+H]^+$.

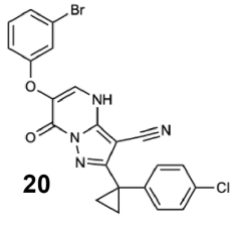

20

General method A was used to obtain 6-(3-bromophenoxy)-2-[1-(4-chlorophenyl)cyclopropyl]-7-oxo-4H-pyrazolo[1,5-a]pyrimidine-3-carbonitrile (**20**, 2.6% yield) as a beige solid. ^{1}H NMR (500 MHz, DMSO-d_6) δ 8.07 (s, 1H), 7.38 (d, 2H), 7.27 (m, 3H), 7.32 (d, 2H), 7.10 (7.15, 1.9 Hz, 1H), 7.01 (dd, 1H), 1.35 (m, 2H), 1.51 (m, 2H). MS m/z: 483 $[M+H]^+$.

Appendices

Supplementary Figure 1 Chemical structures of dynapyrazole derivatives. Basal ATPase activity of Hs-dynein 1 in the presence of dynapyrazole derivatives (20 μM). Chemical structure of each dynapyrazole derivative is shown. (B) Percent steady-state ATPase activity of five AAA proteins in the presence of compound **19** (20 μM). Lines represent mean ± range (n = 2). Compounds **2-19** were synthesized by Yasuhiro Hirata and Yoshiyuki Fukase.

A Structure-activity relationship for compounds with aminopyrazole core

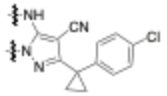

Compound	Substituents	Percent Residual A ATPase activity (range)
3		115 (104-125)
4		115 (91-140)
5		104 (90-118)
6		100 (97-102)
7	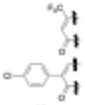	99 (78-120)
8		97 (97-97)
9		92 (88-95)
10		89 (69-109)
11		87 (84-90)
12		80 (77-82)
13		79 (68-89)
14		76 (71-81)
15		75 (71-78)
16		70 (65-74)
17		51 (48-53)
18		49 (45-52)
19		32 (29-34)

B

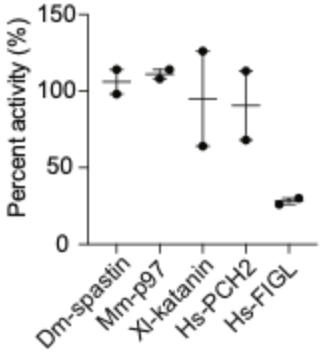

Supplementary Figure 2 X-ray model of Sc-Dyn-lysoMut in the presence of compound 20. (A) Electron densities (blue mesh) of β-strands and α-helices in the AAA1, AAA2, AAA3, and AAA4 sites. Color coding of domains is the same as in Figure 3A. (B-D) Comparison of the AAA1 domain between the X-ray model (gray) and either the *S. cerevisiae* apo (cyan) (B), human ADP (PDB: 5NUG, green) (C), or *S. cerevisiae* AMPPNP (PDB: 4W8F, blue) (D) model. Models are aligned on the AAA1-L subdomain. (E-G) Comparison of the AAA3 domain between the X-ray model (gray) and either the *S. cerevisiae* apo (cyan) (E), human ADP (PDP: 5NUG, green) (F), or Sc-Dyn-lysoMut AMPPNP (PDB: 4W8F, blue) (G) model. Models are aligned on the AAA3-L subdomain. (H-J) Comparison of one side of the AAA ring in the X-ray model (H), apo-model (I), and the AMPPNP-model (J) (PDB: 4W8F). The box highlights the gap between the linker and the AAA1/AAA2/AAA3/AAA4 domains. Color coding of domains is the same as in Figure 3A; models are aligned on the AAA1-L subdomain.

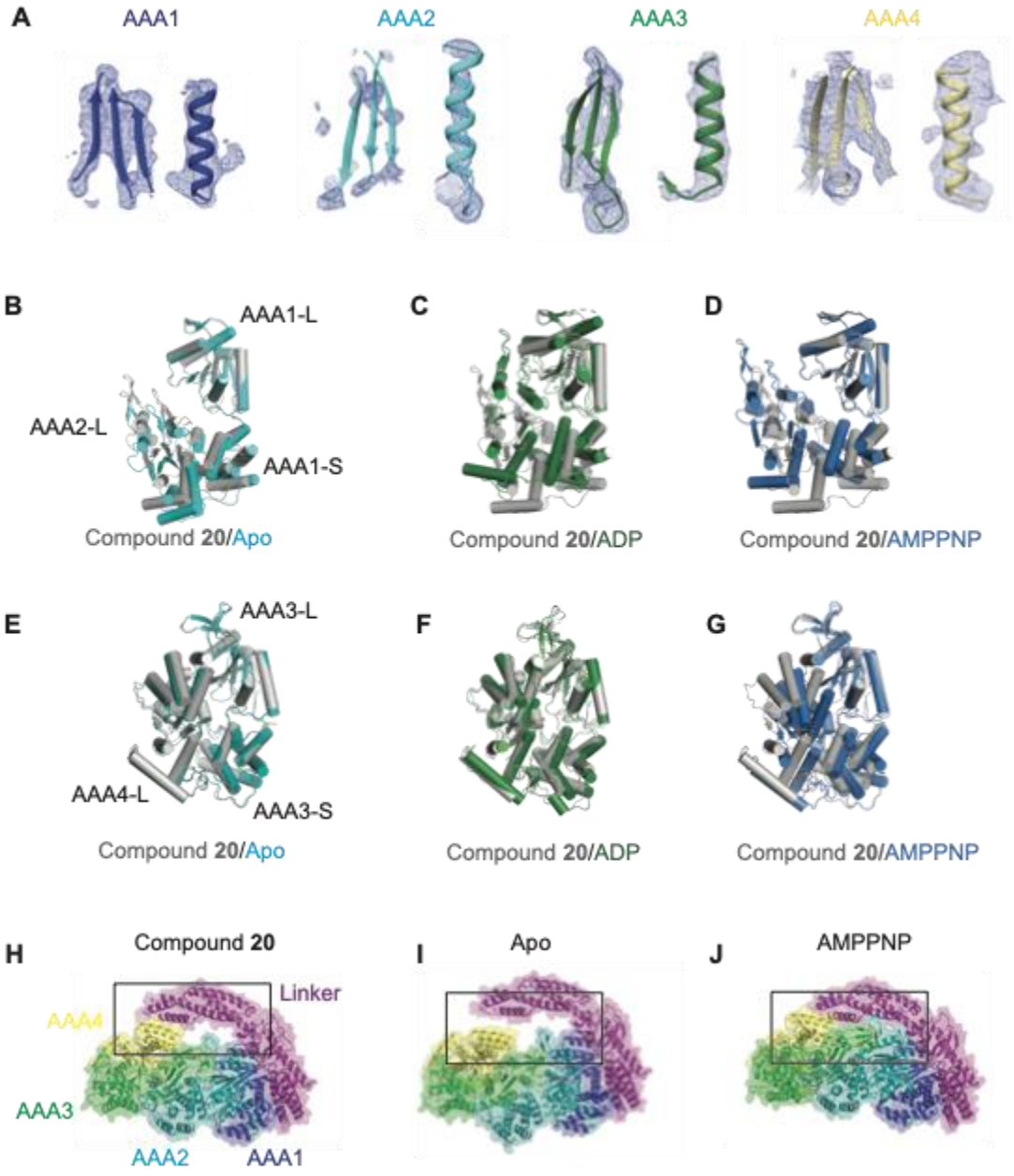
A
AAA1
AAA2
AAA3
AAA4
B
AAA1-L
AAA2-L
AAA1-S
Compound 20/Apo
C
Compound 20/ADP
D
Compound 20/AMPPNP
E
AAA3-L
AAA4-L
AAA3-S
Compound 20/Apo
F
Compound 20/ADP
G
Compound 20/AMPPNP
H
Compound 20
Linker
AAA4
AAA3
AAA2
AAA1
I
Apo
J
AMPPNP

Supplementary Figure 3 Processing of the Cryo-EM data for Sc-Dyn-lysoMut in the presence of compound 20. (A) The workflow used to process datasets 1 and 2 in CryoSparc. (B) The workflow used to process dataset 3 in RELION 3.0.

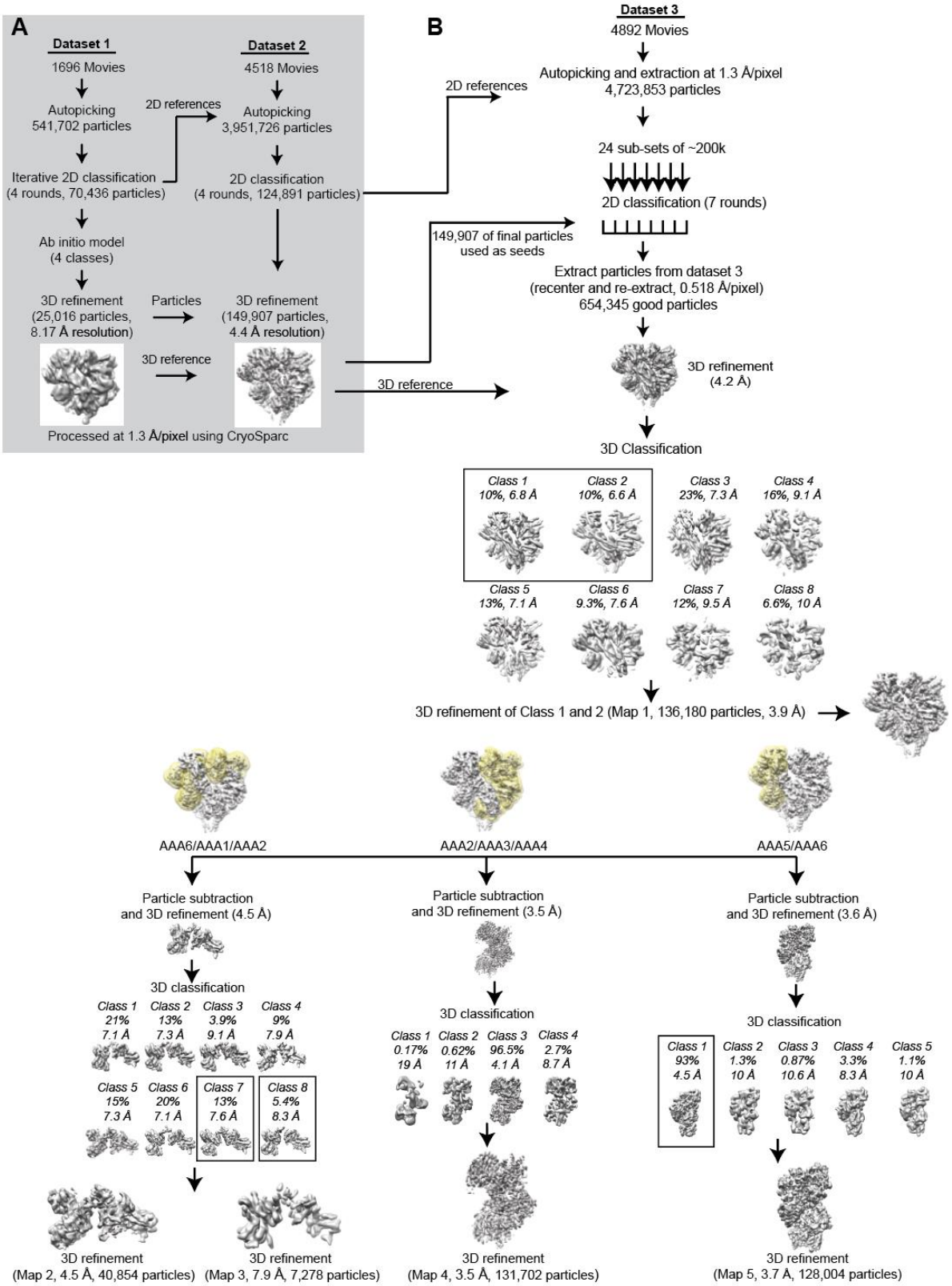
A
Dataset 1
1696 Movies
Autopicking
541,702 particles
Iterative 2D classification
(4 rounds, 70,436 particles)
Ab initio model
(4 classes)
3D refinement
(25,016 particles,
8.17 Å resolution)
Dataset 2
4518 Movies
Autopicking
3,951,726 particles
2D classification
(4 rounds, 124,891 particles)
2D references
Particles
3D refinement
(149,907 particles,
4.4 Å resolution)
3D reference
Processed at 1.3 Å/pixel using CryoSparc
B
Dataset 3
4892 Movies
Autopicking and extraction at 1.3 Å/pixel
4,723,853 particles
2D references
24 sub-sets of ~200k
2D classification (7 rounds)
149,907 of final particles
used as seeds
Extract particles from dataset 3
(recenter and re-extract, 0.518 Å/pixel)
654,345 good particles
3D refinement
(4.2 Å)
3D reference
3D Classification
Class 1
10%, 6.8 Å
Class 2
10%, 6.6 Å
Class 3
23%, 7.3 Å
Class 4
16%, 9.1 Å
Class 5
13%, 7.1 Å
Class 6
9.3%, 7.6 Å
Class 7
12%, 9.5 Å
Class 8
6.6%, 10 Å
3D refinement of Class 1 and 2 (Map 1, 136,180 particles, 3.9 Å)
AAA6/AAA1/AAA2
AAA2/AAA3/AAA4
AAA5/AAA6
Particle subtraction
and 3D refinement (4.5 Å)
3D classification
Class 1
21%
7.1 Å
Class 2
13%
7.3 Å
Class 3
3.9%
9.1 Å
Class 4
9%
7.9 Å
Class 5
15%
7.3 Å
Class 6
20%
7.1 Å
Class 7
13%
7.6 Å
Class 8
5.4%
8.3 Å
3D refinement
(Map 2, 4.5 Å, 40,854 particles)
3D refinement
(Map 3, 7.9 Å, 7,278 particles)
Particle subtraction
and 3D refinement (3.5 Å)
3D classification
Class 1
0.17%
19 Å
Class 2
0.62%
11 Å
Class 3
96.5%
4.1 Å
Class 4
2.7%
8.7 Å
3D refinement
(Map 4, 3.5 Å, 131,702 particles)
Particle subtraction
and 3D refinement (3.6 Å)
3D classification
Class 1
93%
4.5 Å
Class 2
1.3%
10 Å
Class 3
0.87%
10.6 Å
Class 4
3.3%
8.3 Å
Class 5
1.1%
10 Å
3D refinement
(Map 5, 3.7 Å, 128,004 particles)

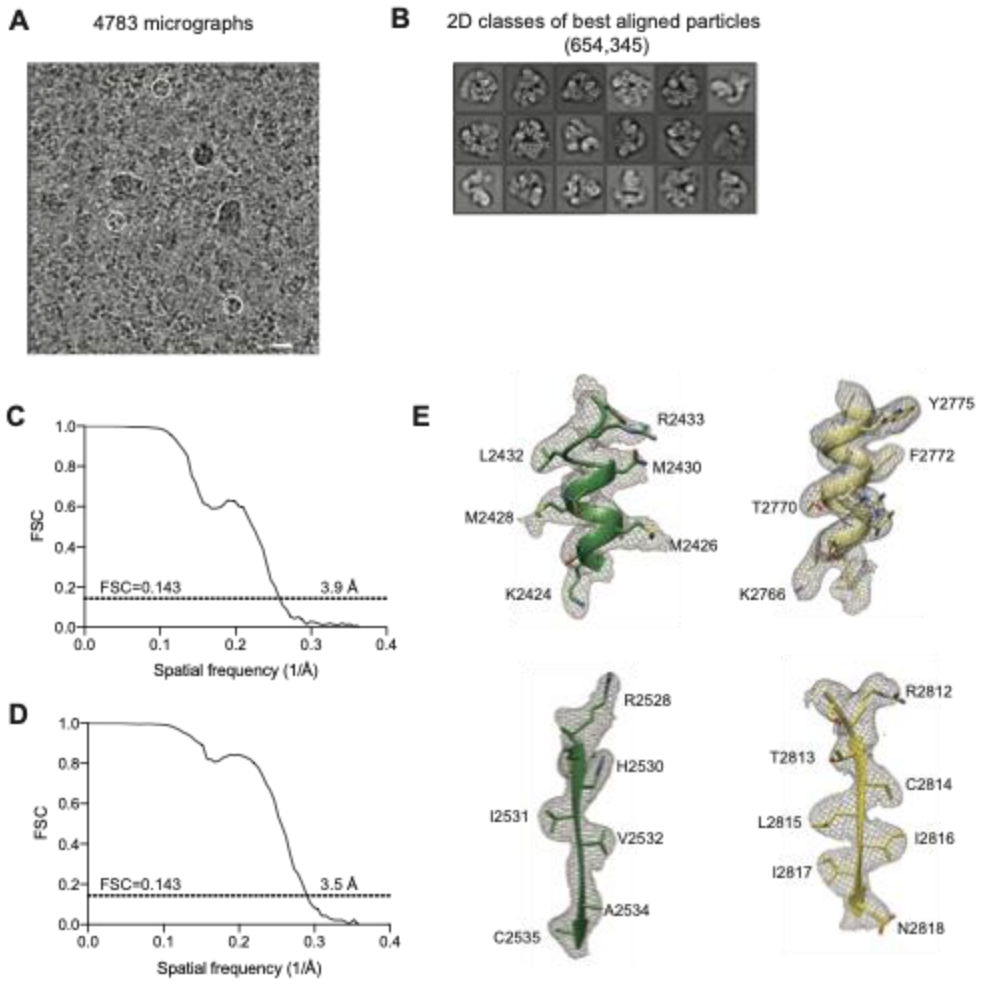

Supplementary Figure 4 Cryo-EM analysis of Sc-Dyn-lysoMut in the presence of compound 20. (A) Representative micrograph from dataset 3 (total: 4892 micrographs). White scale bar represents 20 nm. (B) 2D classes of best aligned particles (654,345). (C) Gold-standard Fourier Shell Correlation (FSC) curve calculated for the Sc-Dyn-lysoMut map (see Figure S3B). The resolution was estimated at ~3.9 Å (FSC=0.143). (D) Gold-standard Fourier Shell Correlation (FSC) curve calculated for the signal subtracted map of the AAA2/AAA3/AAA4 domains (see Figure S3B). The resolution was estimated at ~3.5 Å (FSC=0.143). (E) EM densities (Map 4, gray mesh) of β-strands and α-helices in the AAA3 (green) and AAA4 (yellow) domains. Amino acid residues are indicated and the color coding of domains is the same as in Figure 3A.

Supplementary Figure 5 Analysis of compound binding to Sc-Dyn-lysoMut. (A) Orientation of ATP in the AAA2 site generated by the GlideEM script and overlayed with the EM density (Map 4, blue mesh). ATP is shown as a stick model (carbon: orange, oxygen: red, nitrogen: blue). (B, C) Poses of compound **20** generated by the Glide EM script for the AAA3 (B) and AAA4 (C) sites and overlayed with the EM density (Map 4, blue mesh). Compound **20** is shown as a stick model (carbon: orange, oxygen: red, nitrogen: blue, chlorine: green, bromine: dark red). (D) Comparison of the AAA3 domain between the cryo-EM reconstruction of Map 3 (magenta) and either the X-ray model (gray) or apo-model (cyan). Models are aligned on the AAA3-L subdomain. (E, F) Schematic for the predicted hydrogen bonding (black dashed lines), halogen bonding (green dashed lines) and van der waals interactions (ticked curved lines) between compound **20** and either the N-loop, P-loop or sensor II motifs (N-loop: green, P-loop: yellow, sensor II: blue) in the AAA3 (E) or AAA4 (F) nucleotide-binding pockets.

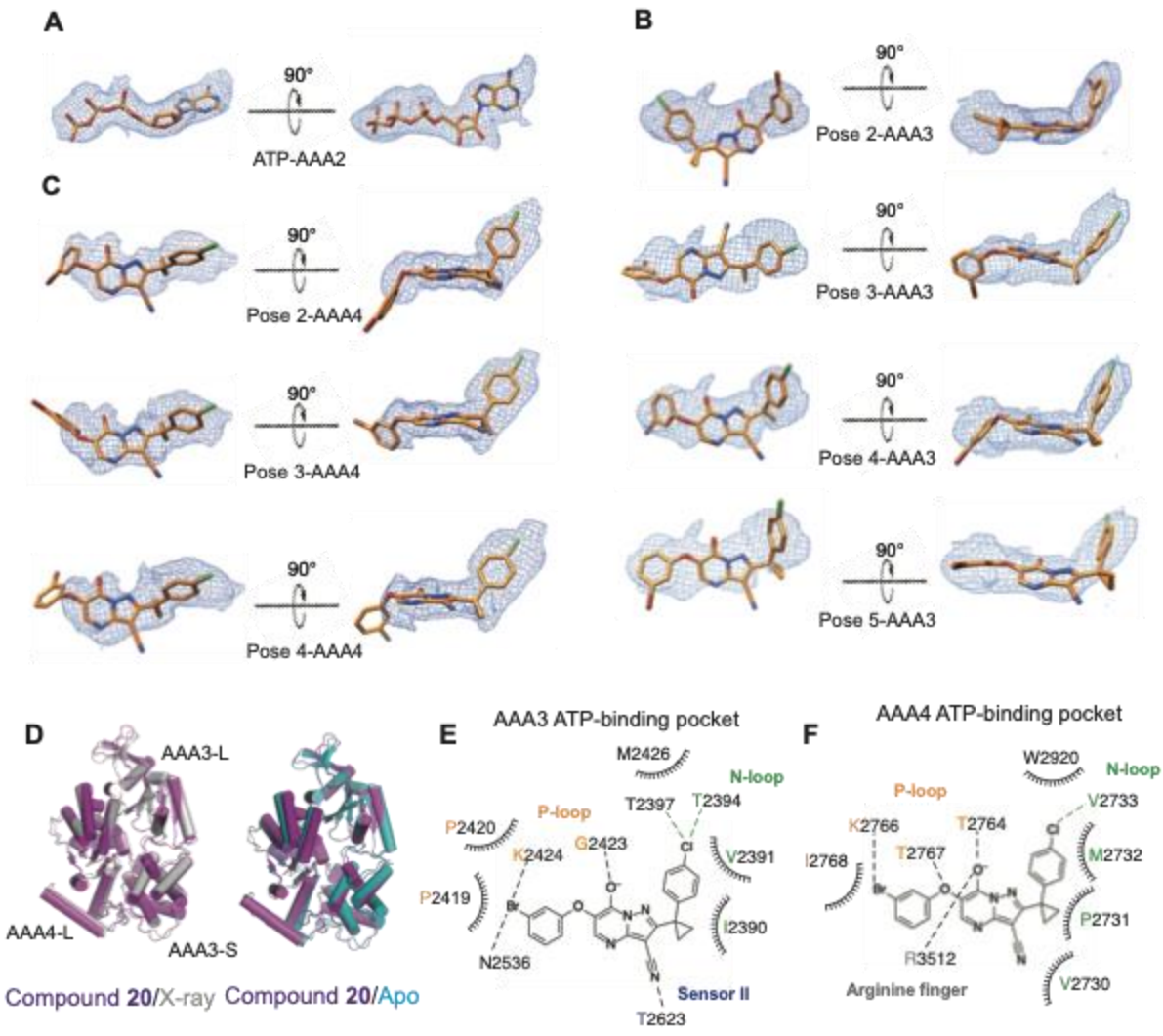
A
90°
ATP-AAA2
B
90°
Pose 2-AAA3
C
90°
Pose 2-AAA4
90°
Pose 3-AAA3
90°
Pose 3-AAA4
90°
Pose 4-AAA3
90°
Pose 4-AAA4
90°
Pose 5-AAA3
D
AAA3-L
AAA4-L
AAA3-S
Compound 20/X-ray Compound 20/Apo
E
AAA3 ATP-binding pocket
M2426
N-loop
T2397
T2394
P-loop
P2420
G2423
K2424
V2391
P2419
I2390
N2536
Sensor II
T2623
F
AAA4 ATP-binding pocket
W2920
N-loop
P-loop
V2733
K2766
T2764
I2768
T2767
M2732
P2731
R3512
Arginine finger
V2730

Supplementary Figure 6 Sequence analysis of human cytoplasmic dynein isoforms 1 and 2. Alignments were performed using the Clustal Omega algorithm for the following AAA domains: (A) human dynein 1 AAA1 (N1867-E2331) and human dynein 2 AAA1 (Q1650-E2082) (B) human dynein 1 AAA3 (S2540-V2838) and human dynein 2 AAA3 (S2233-V2540) (C) human dynein 1 AAA4 (D2880-I3224) and human dynein 2 AAA4 (P2591-E2920). Residues in gray boxes are identical across isoforms. For the AAA1 alignments, black asterisks denote residues < 4 Å from ADP-Vanadate in the AAA1 site of human dynein 2 (PDB 4RH7). For the AAA3 and AAA4 alignments, black asterisks indicate the structurally corresponding residues that are < 4 Å from AMPPNP in the AAA3 and AAA4 sites of *S. cerevisiae* dynein (PDB: 4W8F). Uniprot accession numbers: dynein 1-Q14204, dynein 2-Q8NCM8.

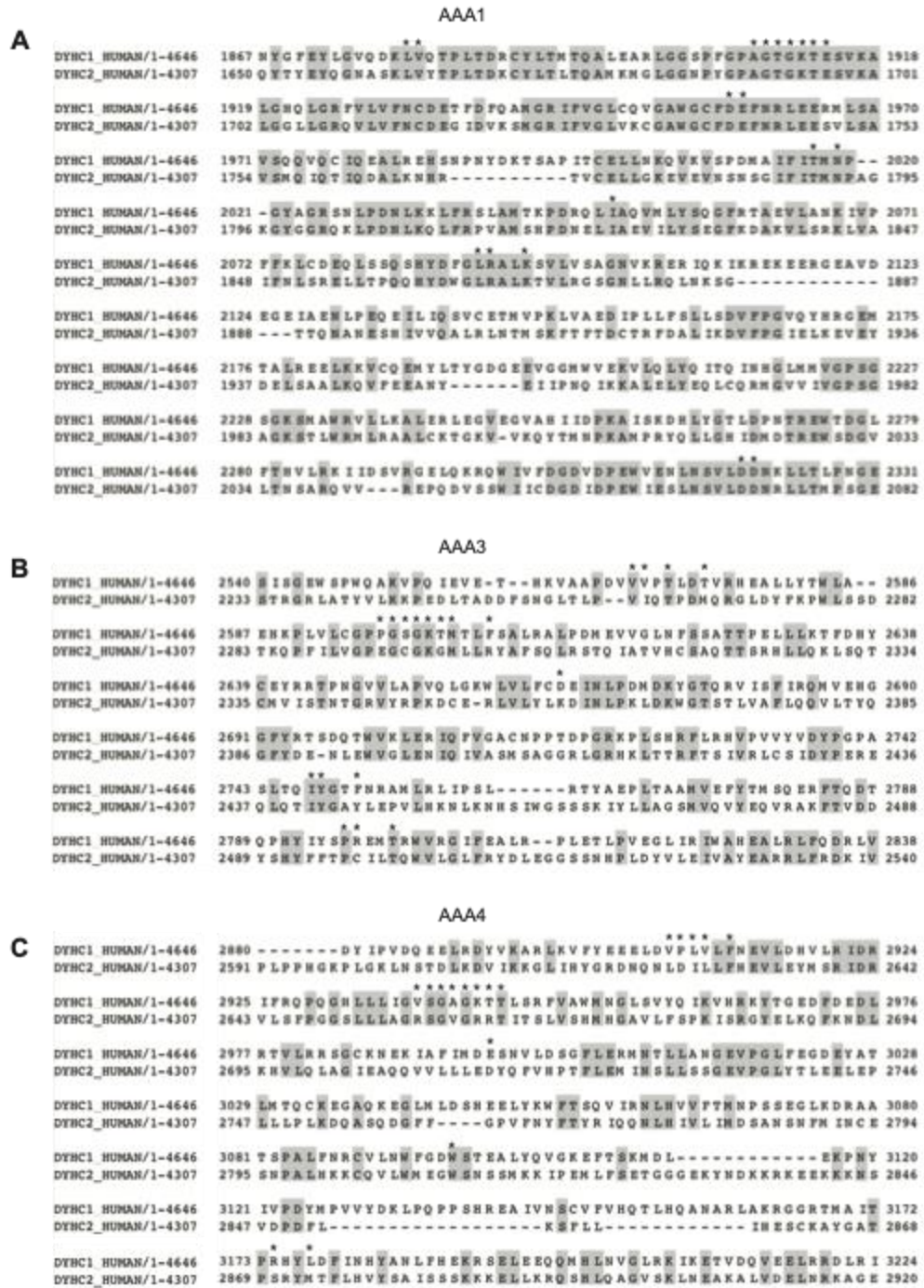
AAA1
A
DYHC1_HUMAN/1-4646 1867 NYGFEYLGVQDKLVQTPLTDRCYLTMTQALEARLGGSPFGPAGTGKTESVKA 1918
DYHC2_HUMAN/1-4307 1650 QYTYEYQGNASKLVYTPLTDKCYLTLTQAMKNGLGGNPYGPAGTGKTESVKA 1701
DYHC1_HUMAN/1-4646 1919 LGNQLGRFVLVFNCDETFDFQAMGRIFVGLCQVGAWGCFDEFNRLEERMLSA 1970
DYHC2_HUMAN/1-4307 1702 LGGLLGRQVLVFNCDEGIDVKSMGRIFVGLVKCGAWGCFDEFNRLEESVLSA 1753
DYHC1_HUMAN/1-4646 1971 VSQQVQCIQEALREHSNPNYDKTSAPITCELLNKQVKVSPDMAIFITMNP-- 2020
DYHC2_HUMAN/1-4307 1754 VSMQIQTIQDALKNHR----------TVCELLGKEVEVNSNSGIFITMNPAG 1795
DYHC1_HUMAN/1-4646 2021 -GYAGRSNLPDNLKKLFRSLAMTKPDRQLIAQVMLYSQGFRTAEVLANKIVP 2071
DYHC2_HUMAN/1-4307 1796 KGYGGRQKLPDNLKQLFRPVAMSHPDNELIAEVILYSEGFKDAKVLSRKLVA 1847
DYHC1_HUMAN/1-4646 2072 FFKLCDEQLSSQSHYDFGLRALKSVLVSAGNVKRERIQKIKRREKEERGEAVD 2123
DYHC2_HUMAN/1-4307 1848 IFNLSRELLTPQQHYDWGLRALKTVLRGSGNLLRQLNKSG------------ 1887
DYHC1_HUMAN/1-4646 2124 EGEIAENLPEQEILIQSVCETNVPKLVAEDIPLLFSLLSDVFPGVQYNRGEM 2175
DYHC2_HUMAN/1-4307 1888 ---TTQNANESNIVVQALRLNTNSKFTFTDCTRFDALIKDVFPGIELKEVEY 1936
DYHC1_HUMAN/1-4646 2176 TALREELKKVCQEMYLTYGDGEEVGGNWVEKVLQLYQITQINSGLNMVGPSG 2227
DYHC2_HUMAN/1-4307 1937 DELSAALKQVFEEANY------EIIPNQIKKALELYEQLCQRMGVVIVGPSG 1982
DYHC1_HUMAN/1-4646 2228 SGKSMAWRVLKALERLEGVEGVAHIIDPKAISKDHLYGTLDPNTREWTDGL 2279
DYHC2_HUMAN/1-4307 1983 AGKSTLWRMLRAALCKTGKV-VKQYTMNPKAMPRYQLLGHIDMDTREWSDGV 2033
DYHC1_HUMAN/1-4646 2280 FTSVLRKIIDSVRGELQKRQWIVFDGDVDPEWVENLNSVLDDNKLLTLPNGE 2331
DYHC2_HUMAN/1-4307 2034 LTNSARQVV---REPQDVSSWIICDGDIDPEWIESLNSVLDDNRLLTMPSGE 2082
AAA3
B
DYHC1_HUMAN/1-4646 2540 SISGEWSPWQAKVPQIEVE-T--HKVAAPDVVVPTLDTVRHEALLYTWLA-- 2586
DYHC2_HUMAN/1-4307 2233 STRGRLATYVLKKPEDLTADDFSNGLTLP--VIQTPDMQRGLDYFKPWLSSD 2282
DYHC1_HUMAN/1-4646 2587 ENKPLVLCGPPGSGKTMTLFSALRALPDMEVVGLNFSSATTPELLLKTFDHY 2638
DYHC2_HUMAN/1-4307 2283 TKQPFILVGPEGCGKGMLLRYAFSQLRSTQIATVHCSAQTTSRHLLQKLSQT 2334
DYHC1_HUMAN/1-4646 2639 CEYRATPNGVVLAPVQLGKWLVLFCDEINLPDMDKYGTQRVISFIRQMVEHG 2690
DYHC2_HUMAN/1-4307 2335 CMVISTNTGRVYRPKDCE-RLVLYLKDINLPKLDKWGTSTLVAFLQQVLTYQ 2385
DYHC1_HUMAN/1-4646 2691 GFYRTSDQTWVKLERIQFVGACNPPTDPGRKPLSHRFLRHVPVVYVDYPGPA 2742
DYHC2_HUMAN/1-4307 2386 GFYDE-NLEWVGLENIQIVASMSAGGRLGRHKLTTRFTSIVRLCSIDYPERE 2436
DYHC1_HUMAN/1-4646 2743 SLTQIYGTFNRAMLRLIPSL------RTYAEPLTAAHVEFYTMSQERFTQDT 2788
DYHC2_HUMAN/1-4307 2437 QLQTIYGAYLEPVLNKNLKNHSIWGSSSKIYLLAGSMVQVYEQVRAKFTVDD 2488
DYHC1_HUMAN/1-4646 2789 QPHYIYSPREMTRWVRGIFEALR--PLETLPVEGLIRIMAHEALRLFQDRLV 2838
DYHC2_HUMAN/1-4307 2489 YSHYFFTFCILTQWVLGLFRYDLEGGSSNNFLDYVLEIVAYEARRLFRDKIV 2540
AAA4
C
DYHC1_HUMAN/1-4646 2880 -------DYIPVDQEELRDYVKARLKVFYEEELDVPLVLFNEVLDHVLRIDR 2924
DYHC2_HUMAN/1-4307 2591 PLPPNGKPLGKLNSTDLKDVIKKGLIHYGRDNQNLDILLFNEVLEYMSRIDR 2642
DYHC1_HUMAN/1-4646 2925 IFRQFQGHLLLIGVSGAGKTTLSRFVAWMNGLSVYQIKVHRKYTGEDFDEDL 2976
DYHC2_HUMAN/1-4307 2643 VLSFGGSLLLAGRSGVGRRTITSLVSHMHGAVLFSPKISRGYELKQFKNDL 2694
DYHC1_HUMAN/1-4646 2977 RTVLRRSGCKNEKIAFIMDESNVLDSGFLERMNTLLANGEVPGLFEGDEYAT 3028
DYHC2_HUMAN/1-4307 2695 KHVLQLAGIEAQQVVLLLEDYQFVHPTFLEMIMSLLSSGEVPGLYTLEELEP 2746
DYHC1_HUMAN/1-4646 3029 LMTQCKEGAQKEGLMLDSNEELYKWFTSQVIRNLHVVFTMNPSSEGLKDRAA 3080
DYHC2_HUMAN/1-4307 2747 LLLPLKDQASQDGFF----GPVFNYFTYRIQQNLHIVLIMDSANSNFMINCE 2794
DYHC1_HUMAN/1-4646 3081 TSPALFNRCVLNWFGDWSTEALYQVGKEFTSKMDL------------EKPNY 3120
DYHC2_HUMAN/1-4307 2795 SNPALNKKCQVLMMEGWSNSSMKKIPEMLFEETGGGEKYNDKKRKEEKKKNS 2846
DYHC1_HUMAN/1-4646 3121 IVPDYMPVVYDKLPQPPSHREAIVNSCVFVHQTLHQANARLAKRGGRTMAIT 3172
DYHC2_HUMAN/1-4307 2847 VDPDFL-------------------KSFLL------------IHESCKAYGAT 2868
DYHC1_HUMAN/1-4646 3173 PRHYLDFINHYANLFHEKRSELEEQQMHLNVGLRKIKETVDQVEELRRDLRI 3224
DYHC2_HUMAN/1-4307 2869 PSRYMTFLHVYSAISSSKKKELLKRQSHLQAGVSKLNEAKALVDELNKKAGE 2920

Table 3.1 X-ray data collection and refinement statistics

	Sc-Dyn-lysoMut
Data collection	
Space group	$P2_12_12$
Cell dimensions	
a, *b*, *c* (Å)	135.06, 157.92, 179.31
α, β, γ (°)	90.00 90.00 90.00
Resolution (Å)	47.66-4.50
Wavelength (Å)	0.920094
R_{meas}	28.6 (168.7%)
$I / \sigma I$	5.99 (1.13)
Completeness (%)	99.5 (98.3)
Total reflections	157857
Unique reflections	23226 (3601)
CC1/2	48.4
Refinement	
Resolution (Å)	50-4.5
No. reflections	157857 (23457)
R_{work}/Rf_{ree}	0.247/0.289
No. atoms	
Protein	42311
Ligand/Ion	N/A
Water	N/A
B-factors	
Protein	225
Ligand/Ion	N/A
Water	N/A
R.m.s deviations	
Bond lengths (Å)	0.002
Bond angles (°)	0.5
Clashscore	5.3
Rotamer Outliers	3.8
Ramachandran	
Favored (%)	94
Allowed (%)	6
Ramachandran Outliers (%)	0

*Data in brackets indicate the high-resolution shell

Table 3.2 Cryo-EM data collection and refinement statistics

Data Collection	Dataset 1		Dataset 2		Dataset 3
Microscope	Titan Krios		Titan Krios		Titan Krios
Camera	K2 Summit		K2 Summit		K2 Summit
Voltage (kV)	300		300		300
Frames	50		50		50
Exposure time (s)	10		10		10
Total dose (ē/Å^2)	71		52		44
Defocus range	-1.5 to -3		-0.9 to -1.7		-1 to -1.5
Super resolution pixel size (Å)	0.6675		0.6675		0.518
Micrographs	1696		4518		4893
Model composition	Sc-Dyn-lysoMut	AAA2/ AAA3/ AAA4	AAA6/ AAA1/ AAA2	AAA5/ AAA6	
Non-hydrogen atoms	42370	19070	14794	14430	
Protein residues	2613	677	936	889	
Ligands (ATP/Compound **19**)	1/2	1/2	0/0	0/0	
Resolution	~3.9	~3.5	~4.7	~3.7	
Map sharpening B-factors (Å2)	-100	-50	-100	-100	
Overall FSC†	0.143	0.143	0.143	0.143	
Correlation coefficient	0.68	0.83	0.63	0.77	
Mean B-factor (Å^2)	100.58	31.46	106.89	80.18	
rmsd (bonds)	0.01	0.004	0.016	0.011	
rmsd (angles)	1.137	0.849	0.982	1.125	
MolProbity score	2.16	1.91	2.17	2.19	
Clashscore, all atoms	14.07	5	6.09	10.90	
Sidechain outliers	1.73	2	3.49	2.74	
Ramachandran plot:					
Favored	95.43	94	93.64	95.60	
Outliers	0.54	0.7	0.54	0.46	

REFERENCES

Afonine PV, Klaholz BP, Moriarty NW, Poon BK, Sobolev OV, Terwilliger TC, Adams PD, Urzhumtsev A. 2018. New tools for the analysis and validation of cryo-EM maps and atomic models. *Acta Crystallogr D Struct Biol* **74**:814–840.

Arkhipova V, Guskov A, Slotboom D-J. 2017. Analysis of the quality of crystallographic data and the limitations of structural models. *J Gen Physiol* **149**:1091–1103.

Axelson M, Liu K, Jiang X, He K, Wang J, Zhao H, Kufrin D, Palmby T, Dong Z, Russell AM, Others. 2013. US Food and Drug Administration approval: vismodegib for recurrent, locally advanced, or metastatic basal cell carcinoma. *Clin Cancer Res* **19**:2289–2293.

Banerjee S, Bartesaghi A, Merk A, Rao P, Bulfer SL, Yan Y, Green N, Mroczkowski B, Neitz RJ, Wipf P, Falconieri V, Deshaies RJ, Milne JLS, Huryn D, Arkin M, Subramaniam S. 2016. 2.3 Å resolution cryo-EM structure of human p97 and mechanism of allosteric inhibition. *Science* **351**:871–875.

Barlan K, Lu W, Gelfand VI. 2013. The microtubule-binding protein ensconsin is an essential cofactor of kinesin-1. *Curr Biol* **23**:317–322.

Bassler J, Kallas M, Pertschy B, Ulbrich C, Thoms M, Hurt E. 2010. The AAA-ATPase Rea1 drives removal of biogenesis factors during multiple stages of 60S ribosome assembly. *Mol Cell* **38**:712–721.

Bhabha G, Cheng H-C, Zhang N, Moeller A, Liao M, Speir JA, Cheng Y, Vale RD. 2014. Allosteric communication in the dynein motor domain. *Cell* **159**:857–868.

Bhabha G, Johnson GT, Schroeder CM, Vale RD. 2016. How Dynein Moves Along Microtubules. *Trends Biochem Sci* **41**:94–105.

Burgess SA, Walker ML, Sakakibara H, Knight PJ, Oiwa K. 2003. Dynein structure and power stroke. *Nature* **421**:715–718.

Burghoorn J, Dekkers MPJ, Rademakers S, de Jong T, Willemsen R, Jansen G. 2007. Mutation of the MAP kinase DYF-5 affects docking and undocking of kinesin-2 motors and reduces their speed in the cilia of Caenorhabditis elegans. *Proc Natl Acad Sci U S A* **104**:7157–7162.

Carter AP, Cho C, Jin L, Vale RD. 2011. Crystal structure of the dynein motor domain. *Science* **331**:1159–1165.

Chen JK, Taipale J, Cooper MK, Beachy PA. 2002. Inhibition of Hedgehog signaling by direct binding of cyclopamine to Smoothened. *Genes Dev* **16**:2743–2748.

Cho C, Reck-Peterson SL, Vale RD. 2008. Regulatory ATPase sites of cytoplasmic dynein affect processivity and force generation. *J Biol Chem* **283**:25839–25845.

Chou T-F, Brown SJ, Minond D, Nordin BE, Li K, Jones AC, Chase P, Porubsky PR, Stoltz BM, Schoenen FJ, Patricelli MP, Hodder P, Rosen H, Deshaies RJ. 2011. Reversible inhibitor of p97, DBeQ, impairs both ubiquitin-dependent and autophagic protein clearance pathways. *Proc Natl Acad Sci U S A* **108**:4834–4839.

Cupido T, Pisa R, Kelley ME, Kapoor TM. 2019. Designing a chemical inhibitor for the AAA protein spastin using active site mutations. *Nat Chem Biol* **15**:444–452.

DeWitt MA, Cypranowska CA, Cleary FB, Belyy V, Yildiz A. 2015. The AAA3 domain of cytoplasmic dynein acts as a switch to facilitate microtubule release. *Nat Struct Mol Biol* **22**:73–80.

Emsley P, Lohkamp B, Scott WG, Cowtan K. 2010. Features and development of Coot. *Acta*

Crystallogr D Biol Crystallogr **66**:486–501.
Engel BD, Ishikawa H, Wemmer KA, Geimer S, Wakabayashi K-I, Hirono M, Craige B, Pazour GJ, Witman GB, Kamiya R, Marshall WF. 2012. The role of retrograde intraflagellar transport in flagellar assembly, maintenance, and function. *J Cell Biol* **199**:151–167.
Engel BD, Ludington WB, Marshall WF. 2009. Intraflagellar transport particle size scales inversely with flagellar length: revisiting the balance-point length control model. *J Cell Biol* **187**:81–89.
Erzberger JP, Berger JM. 2006. Evolutionary relationships and structural mechanisms of AAA+ proteins. *Annu Rev Biophys Biomol Struct* **35**:93–114.
Firestone AJ, Weinger JS, Maldonado M, Barlan K, Langston LD, O'Donnell M, Gelfand VI, Kapoor TM, Chen JK. 2012. Small-molecule inhibitors of the AAA+ ATPase motor cytoplasmic dynein. *Nature* **484**:125–129.
Gibbons BH, Gibbons IR. 1987. Vanadate-sensitized cleavage of dynein heavy chains by 365-nm irradiation of demembranated sperm flagella and its effect on the flagellar motility. *J Biol Chem* **262**:8354–8359.
Granger E, McNee G, Allan V, Woodman P. 2014. The role of the cytoskeleton and molecular motors in endosomal dynamics. *Semin Cell Dev Biol* **31**:20–29.
He M, Subramanian R, Bangs F, Omelchenko T, Liem KF Jr, Kapoor TM, Anderson KV. 2014. The kinesin-4 protein Kif7 regulates mammalian Hedgehog signalling by organizing the cilium tip compartment. *Nat Cell Biol* **16**:663–672.
Hirokawa N, Noda Y, Tanaka Y, Niwa S. 2009. Kinesin superfamily motor proteins and intracellular transport. *Nat Rev Mol Cell Biol* **10**:682–696.
Höing S, Yeh T-Y, Baumann M, Martinez NE, Habenberger P, Kremer L, Drexler HCA, Küchler P, Reinhardt P, Choidas A, Zischinsky M-L, Zischinsky G, Nandini S, Ledray AP, Ketcham SA, Reinhardt L, Abo-Rady M, Glatza M, King SJ, Nussbaumer P, Ziegler S, Klebl B, Schroer TA, Schöler HR, Waldmann H, Sterneckert J. 2018. Dynarrestin, a Novel Inhibitor of Cytoplasmic Dynein. *Cell Chemical Biology*. doi:10.1016/j.chembiol.2017.12.014
Huang J, Roberts AJ, Leschziner AE, Reck-Peterson SL. 2012. Lis1 Acts as a "Clutch" between the ATPase and Microtubule-Binding Domains of the Dynein Motor. *Cell* **150**:975–986.
Ishikawa H, Marshall WF. 2017. Intraflagellar Transport and Ciliary Dynamics. *Cold Spring Harb Perspect Biol* **9**. doi:10.1101/cshperspect.a021998
Jerabek-Willemsen M, André T, Wanner R, Roth HM, Duhr S, Baaske P, Breitsprecher D. 2014. MicroScale Thermophoresis: Interaction analysis and beyond. *J Mol Struct* **1077**:101–113.
Kabsch W. 2010. XDS. *Acta Crystallogr D Biol Crystallogr* **66**:125–132.
Kawashima SA, Chen Z, Aoi Y, Patgiri A, Kobayashi Y, Nurse P, Kapoor TM. 2016. Potent, Reversible, and Specific Chemical Inhibitors of Eukaryotic Ribosome Biogenesis. *Cell* **167**:512–524.e14.
Kim J, Kato M, Beachy PA. 2009. Gli2 trafficking links Hedgehog-dependent activation of Smoothened in the primary cilium to transcriptional activation in the nucleus. *Proc Natl Acad Sci U S A* **106**:21666–21671.
Kon T, Nishiura M, Ohkura R, Toyoshima YY, Sutoh K. 2004. Distinct functions of nucleotide-binding/hydrolysis sites in the four AAA modules of cytoplasmic dynein. *Biochemistry* **43**:11266–11274.
Kon T, Oyama T, Shimo-Kon R, Imamula K, Shima T, Sutoh K, Kurisu G. 2012. The 2.8 Å crystal structure of the dynein motor domain. *Nature* **484**:345–350.

Lechtreck KF. 2015. IFT–Cargo Interactions and Protein Transport in Cilia. *Trends Biochem Sci* **40**:765–778.
Liao X, Siu MKY, Au CWH, Chan QKY, Chan HY, Wong ESY, Ip PPC, Ngan HYS, Cheung ANY. 2009. Aberrant activation of hedgehog signaling pathway contributes to endometrial carcinogenesis through β-catenin. *Mod Pathol* **22**:839–847.
Lin R, Connolly PJ, Huang S, Wetter SK, Lu Y, Murray WV, Emanuel SL, Gruninger RH, Fuentes-Pesquera AR, Rugg CA, Middleton SA, Jolliffe LK. 2005. 1-Acyl-1H-[1,2,4]triazole-3,5-diamine Analogues as Novel and Potent Anticancer Cyclin-Dependent Kinase Inhibitors: Synthesis and Evaluation of Biological Activities. *Journal of Medicinal Chemistry*. doi:10.1021/jm050267e
Magnaghi P, D'Alessio R, Valsasina B, Avanzi N, Rizzi S, Asa D, Gasparri F, Cozzi L, Cucchi U, Orrenius C, Polucci P, Ballinari D, Perrera C, Leone A, Cervi G, Casale E, Xiao Y, Wong C, Anderson DJ, Galvani A, Donati D, O'Brien T, Jackson PK, Isacchi A. 2013. Covalent and allosteric inhibitors of the ATPase VCP/p97 induce cancer cell death. *Nat Chem Biol* **9**:548–556.
Mangeol P, Prevo B, Peterman EJG. 2016. KymographClear and KymographDirect: two tools for the automated quantitative analysis of molecular and cellular dynamics using kymographs. *Mol Biol Cell* **27**:1948–1957.
McCoy AJ, Grosse-Kunstleve RW, Adams PD, Winn MD, Storoni LC, Read RJ. 2007. Phaser crystallographic software. *J Appl Crystallogr* **40**:658–674.
Mijalkovic J, Peterman E. 2019. Inhibiting IFT dynein with ciliobrevin in C. elegans chemosensory cilia. *bioRxiv*. doi:10.1101/531848
Mijalkovic J, Prevo B, Oswald F, Mangeol P, Peterman EJG. 2017. Ensemble and single-molecule dynamics of IFT dynein in Caenorhabditis elegans cilia. *Nat Commun* **8**:14591.
Moore JK, Stuchell-Brereton MD, Cooper JA. 2009. Function of dynein in budding yeast: mitotic spindle positioning in a polarized cell. *Cell Motil Cytoskeleton* **66**:546–555.
Niekamp S, Coudray N, Zhang N, Vale RD, Bhabha G. 2019. Coupling of ATPase activity, microtubule binding, and mechanics in the dynein motor domain. *EMBO J* **38**:e101414.
Pisa R, Cupido T, Kapoor TM. 2019a. Designing Allele-Specific Inhibitors of Spastin, a Microtubule-Severing AAA Protein. *J Am Chem Soc* **141**:5602–5606.
Pisa R, Cupido T, Steinman JB, Jones NH, Kapoor TM. 2019b. Analyzing Resistance to Design Selective Chemical Inhibitors for AAA Proteins. *Cell Chem Biol*. doi:10.1016/j.chembiol.2019.06.001
Prevo B, Scholey JM, Peterman EJG. 2017. Intraflagellar transport: mechanisms of motor action, cooperation, and cargo delivery. *FEBS J* **284**:2905–2931.
Reck-Peterson SL, Yildiz A, Carter AP, Gennerich A, Zhang N, Vale RD. 2006. Single-molecule analysis of dynein processivity and stepping behavior. *Cell* **126**:335–348.
Ridky TW, Cotsarelis G. 2015. Vismodegib resistance in basal cell carcinoma: not a smooth fit. *Cancer Cell*.
Roberts AJ. 2018. Emerging mechanisms of dynein transport in the cytoplasm versus the cilium. *Biochem Soc Trans* **46**:967–982.
Robertson MJ, Van Zundert GCP, Borrelli K, Skiniotis G. 2019. GemSpot: A Pipeline for Robust Modeling of Ligands into CryoEM Maps. *BioRxiv*.
Rohatgi R, Milenkovic L, Scott MP. 2007. Patched1 regulates hedgehog signaling at the primary cilium. *Science* **317**:372–376.
Rohou A, Grigorieff N. 2015. CTFFIND4: Fast and accurate defocus estimation from electron

micrographs. *J Struct Biol* **192**:216–221.
Roossien DH, Miller KE, Gallo G. 2015. Ciliobrevins as tools for studying dynein motor function. *Front Cell Neurosci* **9**:252.
Schmidt H, Carter AP. 2016. Review: Structure and mechanism of the dynein motor ATPase. *Biopolymers* **105**:557–567.
Schmidt H, Gleave ES, Carter AP. 2012. Insights into dynein motor domain function from a 3.3-Å crystal structure. *Nat Struct Mol Biol* **19**:492–7, S1.
Schmidt H, Zalyte R, Urnavicius L, Carter AP. 2015. Structure of human cytoplasmic dynein-2 primed for its power stroke. *Nature* **518**:435–438.
See SK, Hoogendoorn S, Chung AH, Ye F, Steinman JB, Sakata-Kato T, Miller RM, Cupido T, Zalyte R, Carter AP, Nachury MV, Kapoor TM, Chen JK. 2016. Cytoplasmic Dynein Antagonists with Improved Potency and Isoform Selectivity. *ACS Chem Biol* **11**:53–60.
Shalaeva DN, Cherepanov DA, Galperin MY, Golovin AV, Mulkidjanian AY. 2018. Evolution of cation binding in the active sites of P-loop nucleoside triphosphatases in relation to the basic catalytic mechanism. *eLife*. doi:10.7554/elife.37373
Steinman JB, Kapoor TM. 2019. Using chemical inhibitors to probe AAA protein conformational dynamics and cellular functions. *Curr Opin Chem Biol* **50**:45–54.
Steinman JB, Santarossa CC, Miller RM, Yu LS, Serpinskaya AS, Furukawa H, Morimoto S, Tanaka Y, Nishitani M, Asano M, Zalyte R, Ondrus AE, Johnson AG, Ye F, Nachury MV, Fukase Y, Aso K, Foley MA, Gelfand VI, Chen JK, Carter AP, Kapoor TM. 2017. Chemical structure-guided design of dynapyrazoles, cell-permeable dynein inhibitors with a unique mode of action. *Elife* **6**. doi:10.7554/eLife.25174
Taipale J, Chen JK, Cooper MK, Wang B, Mann RK, Milenkovic L, Scott MP, Beachy PA. 2000. Effects of oncogenic mutations in Smoothened and Patched can be reversed by cyclopamine. *Nature* **406**:1005–1009.
Tang WK, Odzorig T, Jin W, Xia D. 2019. Structural Basis of p97 Inhibition by the Site-Selective Anticancer Compound CB-5083. *Mol Pharmacol* **95**:286–293.
Toropova K, Zou S, Roberts AJ, Redwine WB, Goodman BS, Reck-Peterson SL, Leschziner AE. 2014. Lis1 regulates dynein by sterically blocking its mechanochemical cycle. *eLife*. doi:10.7554/elife.03372
Ulbrich C, Diepholz M, Bassler J, Kressler D, Pertschy B, Galani K, Böttcher B, Hurt E. 2009. Mechanochemical removal of ribosome biogenesis factors from nascent 60S ribosomal subunits. *Cell* **138**:911–922.
Vale RD. 2000. AAA proteins. Lords of the ring. *J Cell Biol* **150**:F13–9.
van den Boom J, Meyer H. 2018. VCP/p97-Mediated Unfolding as a Principle in Protein Homeostasis and Signaling. *Mol Cell* **69**:182–194.
Walker JE, Saraste M, Runswick MJ, Gay NJ. 1982. Distantly related sequences in the alpha- and beta-subunits of ATP synthase, myosin, kinases and other ATP-requiring enzymes and a common nucleotide binding fold. *The EMBO Journal*. doi:10.1002/j.1460-2075.1982.tb01276.x
White SR, Lauring B. 2007. AAA+ ATPases: achieving diversity of function with conserved machinery. *Traffic* **8**:1657–1667.
Yang TT, Tony Yang T, Su J, Wang W-J, Craige B, Witman GB, Tsou M-FB, Liao J-C. 2015. Superresolution Pattern Recognition Reveals the Architectural Map of the Ciliary Transition Zone. *Scientific Reports*. doi:10.1038/srep14096
Ye F, Breslow DK, Koslover EF, Spakowitz AJ, Nelson WJ, Nachury MV. 2013. Single

molecule imaging reveals a major role for diffusion in the exploration of ciliary space by signaling receptors. *Elife* **2**:e00654.
Yeh T-Y, Quintyne NJ, Scipioni BR, Eckley DM, Schroer TA. 2012. Dynactin's pointed-end complex is a cargo-targeting module. *Mol Biol Cell* **23**:3827–3837.
Zhang K, Foster HE, Rondelet A, Lacey SE, Bahi-Buisson N, Bird AW, Carter AP. 2017. Cryo-EM Reveals How Human Cytoplasmic Dynein Is Auto-inhibited and Activated. *Cell* **169**:1303–1314.e18.